P-ISSN 0126-3188
E-ISSN 2443-3926

METALURGI

VOLUME 37 ISSUE 2, AGUSTUS 2022
SCIENTIFIC JOURNAL ACCREDITATION NUMBER NO.3/E/KPT/2019

National Research and Innovation Agency

Publisher :
National Research and Innovation Agency (BRIN)
Kawasan Puspiptek Serpong, Tangerang Selatan, Banten, Indonesia, 15314

E-mail: jurnalmetalurgi@mail.lipi.go.id

Science and technology magazine, regularly published every year; one volume consists of 3 editions

METALURGI

VOLUME 37 NUMBER 2, AGUSTUS 2022

P-ISSN 0126-3188
E-ISSN 2443-3926

ACCREDITATION : SK No. 3/E/KPT/2019

PREFACE

Thanks to Allah SWT, five articles could be published in Metalurgi Magazine Volume 37 Number 2 in August 2022.

The first article conducted by Made Subekti Dwijaya et al. on Preliminary Study of Material Properties on PU-Mg and PU-Zn for Aneurysm Clip Application. The second article, Hardness and Corrosion Behavior of Ti-20Cu-20Ni-20Mn-20Zn as High Entropy Alloy and Ti-13Cu-9Ni-5Mn-5Zn for Marine Structure Application, was presented by Muhammad Azhar Ariefkha Dani et al. In the following article, Nofrijon Sofyan et al. discussed Effect of Heating Temperature and Die Insert Draft Angle on the Flowability of Hot Forged SCM 435 Steel. Muhammad Faisal Akbar et al. discussed the fourth article, Effect of Nd_2O_3 and Fe_2O_3 Addition on Gadolinia Doped Ceria (GDC) Solid Electrolyte System for Intermediate Temperature-Solid Oxide Fuel Cell (IT-SOFC) Applications. Aufa Rai Adiatama et al. wrote the fifth article, Synthesis and Characteristic of Nano Silica from Geothermal Sludge: Effect of Surfactant.

Hopefully, the publication of this volume of Metalurgi Magazine will benefit the advancement of research in Indonesia.

EDITORIAL

METALURGI

ISSN 0126 – 3188 Vol. 37 No. 2 Agustus 2022

Keywords sourced from articles. This abstract is reproduced without permission or fee.

UDC (OXDCF) 620.1

Made Subekti Dwijaya, Talitha Asmaria (Research Center for Metallurgy, National Research and Innovation Agency)

Metalurgi, Vol. 37 No. 2 Agustus 2022

Preliminary Study of Material Properties on PU-Mg and PU-Zn for Aneurysm Clip Application

An aneurysm clip is an implant tool for assisting the neurosurgeon in treating acute hemorrhagic stroke and cerebral aneurysm. This equipment stops the blood flow of a ruptured or enlarged blood vessel or aneurysm. In the development of aneurysm clip production, titanium alloy is the most used material selection. Several researchers reported that this metal leads to artifacts during MR (magnetic resonance) or CT (computed tomography) imaging. Since several pieces of evidence polyurethane could be a good material selection for aneurysm clips, this paper aims to investigate the material properties of the polyurethane foam with an additional combination of magnesium and zinc. This study conducts magnesium and zinc composition variations of 1 wt.%, 2 wt.%, and 3 wt.%, respectively. The materials were tested using a compression test, a FTIR (fourier-transform-infrared), SEM (scanning-electron-microscope), DSC (differential-scanning-calorimetry), and TGA (thermogravimetric-analyzer) to determine the material properties. From all examinations, adding magnesium and zinc to polyurethane foam affected the compressive strength and porosity of the polyurethane foam. Therefore, all test results concluded that adding magnesium with a composition of 3wt.%, which has a compressive strength of 0.84 MPa, is the best mixture. The idea of finding other compositions that are compatible with the polyurethane will significantly increase the possibility of new materials for aneurysm clip construction.

Keywords: Aneurysm clip, compressive strength, magnesium, polyurethane foam, zinc

METALURGI

ISSN 0126 – 3188 Vol. 37 No. 2 Agustus 2022

Keywords sourced from articles. This abstract is reproduced without permission or fee.

UDC (OXDCF) 620.110

Muhammad Azhar Ariefkha Dani[a], Bonita Dilasari[a], Yudi Nugraha Thaha[b], Ika Kartika[b], Fendy Rokhmanto[b] ([a]Department of Metallurgical Engineering, Bandung Institute of Technology, [b] Research Center for Metallurgy, National Research and Innovation Agency)

Metalurgi, Vol. 37 No. 2 Agustus 2022

Hardness and Corrosion Behavior of Ti-20Cu-20Ni-20Mn-20Zn as High Entropy Alloy and Ti-13Cu-9Ni-5Mn-5Zn for Marine Structure Application

Beta titanium alloys and titanium high entropy alloys are promising candidates for marine structural applications. This study aims to compare Ti-20Cu-20Ni-20Mn-20Zn high entropy alloy and Ti-13Cu-9Ni-5Mn-5Zn beta titanium alloy on microstructure, mechanical properties, and corrosion behavior in a 3.5% NaCl solution. Ti-20Cu-20Ni-20Mn-20Zn and Ti-13Cu-9Ni-5Mn-5Zn were produced by powder metallurgy. In the experimental results, it was observed that Ti-20Cu-20Ni-20Mn-20Zn alloy, as a high entropy alloy, has a low hardness value of 190.658 HV and a high corrosion rate of 1.7992 mm/year. The Ti-13Cu-9Ni-5Mn-5Zn alloy as the beta-titanium alloy has a high hardness value of 430.736 HV and a low corrosion rate of 0.12121 mm/year. The results indicate that Ti-13Cu-9Ni-5Mn-5Zn has better corrosion resistance in 3.5% NaCl solution and hardness than Ti-20Cu-20Ni-20Mn-20Zn high entropy alloy.

Keywords: Beta-titanium, high entropy alloys, powder metallurgy, corrosion, marine structure application

METALURGI

ISSN 0126 – 3188 Vol. 37 No. 2 Agustus 2022

Keywords sourced from articles. This abstract is reproduced without permission or fee.

UDC (OXDCF) 620.16

Nofrijon Sofyan[a], Maulana Heruwiyono[a], Akhmad Herman Yuwono[a], Donanta Dhaneswara[a] ([a]Departments of Metallurgical and Materials Engineering, Universitas Indonesia)

Metalurgi, Vol. 37 No. 2 Agustus 2022

Effect of Heating Temperature and Die Insert Draft Angle on the Flowability of Hot Forged SCM 435 Steel

The flowability problem of a closed forging process in the heavy equipment industry is still widely found. This problem may affect the quality of the product. To solve this problem, the effect of heating temperature and die insert draft angle on the characteristic of hot forged SCM435 steel used for undercarriage track roller has been examined. In the experiment, the workpieces were hot forged at a heating temperatures of 1150 °C, 1200 °C, 1250 °C, and die to insert draft angles of 3°, 5°, and 7° to form undercarriage track roller products. The mechanical properties of the specimens taken from the workpieces were characterized through hardness and dimensional changes, whereas the microstructure was characterized using an optical microscope. The results showed that increasing the heating temperature and die insert draft angle resulted in good flowability. The best product with the specified diameter of 191.2 mm and height of 53.6 mm was obtained from the heating temperature of 1250 °C at the die insert draft angle of 7°. This characteristic agreed with the specified forging design for the undercarriage track roller.

Keywords: Flowability, hot forging, track roller, undercarriage, underfilling

METALURGI

ISSN 0126 – 3188 Vol. 37 No. 2 Agustus 2022

Keywords sourced from articles. This abstract is reproduced without permission or fee.

UDC (OXDCF) 546.3

Muhammad Faisal Akbar[a], Bonita Dilasari[a], Syoni Soepriyanto[a], Dadan Suhendar[a] ([a]Bandung Institute of Technology)

Metalurgi, Vol. 37 No. 2 Agustus 2022

Effect of Nd_2O_3 and Fe_2O_3 Addition on Gadolinia Doped Ceria (GDC) Solid Electrolyte System for Intermediate Temperature-Solid Oxide Fuel Cell (IT-SOFC) Applications

GDC (gadolinia doped ceria) is a solid electrolyte contender for intermediate-temperature SOFCs (solid oxide fuel cell). However, more development of this solid electrolyte is required to improve its ionic conductivity. We will investigate the effect of Nd_2O_3 and Fe_2O_3 addition on GDC solid electrolytes to boost ionic conductivity. Solid electrolytes of the composition $Ce_{0.9}Gd_{0.2}M_xO_{1.9}$ (M = Nd, Fe) (x = 0% ; 2.5% ; 5%, and 7.5%) were synthesized using mixed oxide method and formed into pellets with a diameter of 1 cm. The pellets were sintered at 1200℃ and 1400℃ for 4 hours in an Argon environment then the EIS (electrochemical impedance spectroscopy) test was performed at 450-650°C. The results showed that the Nd_2O_3 and Fe_2O_3 added were totally dissolved in the ceria structure and produced single-phase cubic fluorite CeO_2. GDC solid electrolyte with Fe_2O_3 addition produces higher densification than Nd_2O_3 addition, where the value reaches 75% in the GDC sintered at 1400℃. However, the addition of Nd_2O_3 further increased the value of ionic conductivity and decreased the activation energy of the GDC solid electrolyte compared to the addition of Fe_2O_3. The highest ionic conductivity and the lowest activation energy were obtained in the GDC with 2.5% Nd_2O_3 in 650℃ operating temperature, with the values achieved were 1.2 mS/cm and 0.41 eV, respectively. Therefore, it can be concluded that Nd_2O_3 addition is more effective to improve the performance of solid electrolyte GDC.

Keywords: SOFC (solid-oxide fuel cell), solid electrolyte, GDC (gadolinia doped ceria), ionic conductivity

METALURGI

ISSN 0126 – 3188 Vol. 37 No. 2 Agustus 2022

Keywords sourced from articles. This abstract is reproduced without permission or fee.

UDC (OXDCF) 553.4

Aufa Rai Adiatama[a], Ratna Frida Susanti[a], Widi Astuti[b], Himawan Tri Bayu Murti Petrus[c], Kevin Cleary Wanta[a] ([a]Department of Chemical Engineering, Parahyangan Catholic University, [b]Reseach Unit for Mineral Technology, National Research and Innovation Agency, [c]Department of Chemical Engineering, Universitas Gadjah Mada)

Metalurgi, Vol. 37 No. 2 Agustus 2022

Synthesis and Characteristic of Nano Siilica from Geothermal Sludge: Effect of Surfactant

In the synthesis of nanoparticles, the phenomenon of agglomeration is an undesirable condition because the particles formed can be larger. The use of surfactants can prevent the occurrence of this phenomenon. In this study, the use of surfactants was studied in the synthesis of nano silica from geothermal sludge. The method applied in the synthesis of nano silica is the sol-gel method. A 1 M NaOH (sodium hydroxide) solution was used to prepare of the precursor solution, while the SiO_2 gel formation was carried out at a pH of 5 using a 1.5 M HCl (hydrochloric acid) solution. The surfactants used were ABS (alkyl benzene sulfonate), CTAB (cetyltrimethylammonium bromide), SDS (sodium dodecyl sulfate), and PVP (polyvinylpyrrolidone). The surfactant added to the precursor solution was at the CMC (critical micelle concentration), where the CMC value for each surfactant was 0.15; 0.05; 0.50; and 1.00 wt% for ABS, CTAB, SDS, and PVP, respectively. As a comparison, nano silica synthesis was also carried out without adding of surfactants. The experimental results showed that the synthesis of nano silica without surfactant produced a product with a purity of 98.03%. Based on PSA (particle size analyzer) testing, the average particle size was 4.82 μm. Although the purity was already high, the resulting product experiences agglomeration and surfactants were needed to minimize the occurrence of agglomeration in the product. The surfactant that gives the best product quality is PVP, whose average particle size is 66% smaller than the product without surfactant. However, the effect produced with PVP has a low purity, which is 56.67%. This condition occurs because NaCl was trapped in the surfactant template. The presence of this surfactant template causes the washing process more difficult because the templates become an obstacle for water to diffuse into the particles and dissolve the impurities.

Keywords: Agglomeration, nano silica, geothermal sludge, surfactant

METALURGI
Majalah Ilmu dan Teknologi
p-ISSN 0126-3188 | e-ISSN 2443-3926
ejurnalmaterialmetalurgi.lipi.go.id

PRELIMINARY STUDY OF MATERIAL PROPERTIES ON PU-Mg AND PU-Zn FOR ANEURYSM CLIP APPLICATION

Made Subekti Dwijaya*, Talitha Asmaria
Research Center for Metallurgy, National Research and Innovation Agency
Management Building 720, B.J. Habibie Sains and Technology Area, Banten, Indonesia 15343
*E-mail: made004@brin.go.id

Received: 13-05-2022, Revised: 19-07-2022, Accepted: 04-10-2022

Abstract

An aneurysm clip is an implant tool for assisting the neurosurgeon in treating acute hemorrhagic stroke and cerebral aneurysm. This equipment stops the blood flow of a ruptured or enlarged blood vessel or aneurysm. In the development of aneurysm clip production, titanium alloy is the most used material selection. Several researchers reported that this metal leads to artifacts during MR (magnetic resonance) or CT (computed tomography) imaging. Since several pieces of evidence polyurethane could be a good material selection for aneurysm clips, this paper aims to investigate the material properties of the polyurethane foam with an additional combination of magnesium and zinc. This study conducts magnesium and zinc composition variations of 1 wt.%, 2 wt.%, and 3 wt.%, respectively. The materials were tested using a compression test, a FTIR (fourier-transform-infrared), SEM (scanning-electron-microscope), DSC (differential-scanning-calorimetry), and TGA (thermogravimetric-analyzer) to determine the material properties. From all examinations, adding magnesium and zinc to polyurethane foam affected the compressive strength and porosity of the polyurethane foam. Therefore, all test results concluded that adding magnesium with a composition of 3wt.%, which has a compressive strength of 0.84 MPa, is the best mixture. The idea of finding other compositions that are compatible with the polyurethane will significantly increase the possibility of new materials for aneurysm clip construction.

Keywords: *Aneurysm clip, compressive strength, magnesium, polyurethane foam, zinc*

1. INTRODUCTION

Aneurysm clip is one of the neurosurgery management tools to treat by clamping the blood vessels [1]-[2]. Several health conditions, such as acute hemorrhagic stroke and cerebral aneurysm, require a specific operation to close the aneurysm or the area of the blood vessel that is ruptured or enlarged by using a clip with metal material in the blood vessel. A hemorrhagic stroke happens because of a blood vessel rupture that acts as a blood supply to the brain. In cases of acute hemorrhagic stroke, surgery is one of the recommended actions because it is an effort to stop bleeding, reduce pressure in the skull, increase the possibility of recovery and reduce the death rate from stroke [1]. Furthermore, cerebral aneurysms are a kind of cerebrovascular illness in which a weakening of a cerebral artery results in an abnormal focal dilation. The therapies of microsurgical and endovascular have two aims; to remove brain aneurysms from the cerebral circulation and to prevent them from rupturing [3]. Another treatment for cerebral aneurysms is surgical clipping, ensuring the cerebral aneurysm from blood flowing with a clip.

An ideal aneurysm clip model requires these features: small size, biocompatibility, low cost, good mechanical properties (such as tensile strength, corrosion resistance, and fatigue resistance), and common image artifacts [4]. The innovation of aneurysm clip was started by Helbert Olivercona (1891-1980), followed by many contributors; those were Frank Mayfield (1908-1991), Charles Drake (1920-1998), Joseph McFadden (1920-present), Thoralf Sundt Jr. (1930-1992), William M. Lougheed (1923-2004), William B. Scoville (1906-1984), Milton D. Heifetz (1921-2015), Gazi Yasargil (1925-present), Kenichiro Sugita (1932-1994), and Robert Spetzler (1944-present)[5]. Based on this

DOI : 10.14203/metalurgi.v37i2.645

Metalurgi is Sinta 2 Journal (https://sinta.ristekbrin.go.id/journals/detail?id=3708) accredited by Ministry of Research & Technology, Republic Indonesia

last review paper about the origins of eponymous aneurysm clips, the innovation in medicine, including aneurysm clips, is significant in supporting aneurysm surgery. Designs and material selection are the most consideration in the manufacturing technology of aneurysm clips. In developing aneurysm clip materials, Ti6Al4V is the most used material. Like most metal implant materials, Ti6Al4V has good mechanical properties and biocompatibility, low density, good corrosion resistance, and low young's modulus of 55-110 GPa. Although Ti6Al4V has a higher Young's modulus than the bone, around 10-30 GPa, it has a significantly lower Young's modulus compared to other biocompatible metals, which are CoCr around 240 GPa and SS316L around 240 GPa[6]-[8].

Besides that, the titanium alloy could cause artifacts in MRI (magnetic resonance imaging), which could aggravate the aneurysm and the surrounding tissue diagnosis [9]. Kocasarac et al.'s research show that the titanium and titanium alloy implants produced high susceptibility artifacts on MRI that caused decreasing quality images due to large signal voids[10]. Ito et al. examined the artifacts caused by titanium clips on MR (magnetic resonance) images and detected the artifact sizes 200% larger than the size of the actual clips [11]. Another study by Khursheed et al. revealed that the largest artifact produced by titanium alloy aneurysm clip takes up 3.94% of brain volume, and the artifact/clip length ratio is 4.75 to 6.55 mm [12]. Based on the evidence presented, another material is considered for an aneurysm clip, and one of them is a polymer.

Magnesium as an implant material is widely used in many surgical applications. Its lightweight, biocompatible and has sufficiently good mechanical properties. Moreover, the MRI artifact generated by magnesium is less severe than the titanium implant, demonstrating a superior 3D image reconstruction quality compared to titanium [13]. In medical imaging, a magnesium implant has beneficial properties compared to other metal implants. Conventional radiography showed only small attenuation using the magnesium and was lower than the Titanium imaging. Moreover, in MRI, magnesium produced fewer artifacts than titanium, which could ease the imaging evaluation in postoperative [14].

A solid fiducial marker is usually made of high atomic materials such as gold. However, such materials generate streak artifacts which affect the radiation dose calculation and post-treatment assessment. A suitable fiducial marker should minimize artifacts. Zinc has a 7.14 g/cm^3 density, which is 37% of gold. The atomic number of zinc is 30, much lower than gold but five times of carbon. Zinc is also known for its biocompatibility and low toxicity degradation release (0.15mg/day, the toxicity threshold is 100-150mg/day) [15].

Polymer is one of the biomedical implant materials thanks to its biocompatibility, biostability, and noncytotoxic. Gas and water permeability are also calculated to protect the electronic circuit device from moisture and ions within the body [16]. Due to its wide range of options and achieved requirements, polymer-based for aneurysm clips are developed these days. W. S. Cho et al., showed that polyurethane and PDMS (polydimethylsiloxane) was the perfect candidates for aneurysms clip material [17]. Polyurethane has a higher value than PDMS, considering the elastic modulus and strain to failure. Polyurethanes are synthetic polymers that feature hard and soft microstructures. Diisocyanates with low molecular weight and high glass transitions form the hard phase. Thus, this study chose polyurethane for the aneurysm clip materials.

On the other hand, the soft phase comprises polyols with low glass transitions. This polymeric material has 90.1± 0.3°Sh A hardness with 7.2 ± 0.2 MPa. The polyurethane chains can be incorporated into active substances to improve the mechanical properties and meet the requirements of an aneurysm clip [18]. In 2018, Won-Sang Cho et al. researched an aneurysm clip made of zirconia-polyurethane with MR compatibility and mechanical properties to minimize the imaging artifacts [17]. They used commercial 3 mol% Y_2O_3-stabilized ZrO_2 and TiO_2 for the clip body and polyurethane and PDMS for the head spring. The MR susceptibility test showed minor artifacts; the artifact volume is 2.6 times larger than the real one. Polyurethane showed a higher elastic modulus than PDMS, so polyurethane was chosen to be the head spring. There are not many polymer-based aneurysm clips developed.

This paper aims to fabricate polymer-based aneurysm clips to minimize the CT (computed tomography) imaging artifacts by adding 1, 2, and 3 wt.% magnesium powder and 1, 2, and 3 wt.% zinc powder. The material will be tested with FTIR (fourier-transform-infrared), SEM (scanning-electron-microscope), DSC (differential-scanning-calorimetry), TGA (thermogravimetric-analyzer) and a compression test. This paper will significantly contribute to

developing material selection for the aneurysm clips.

2. MATERIALS AND METHODS

Polyurethane parts A (isocyanate part) and B (polyols part) with a volume ratio of 2:1 were prepared. First, the isocyanate part, the polyols part of PU (polyurethane), and the 1, 2, & 3 wt.% of magnesium and zinc powder were added into the mold. The blend stirred for 3 minutes at a constant rate; after the free rise foam process was completed, the foam synthesis continued by a curing process at ambient temperature for 24 hours. After 24 hours, the PU foam was cut into three cubes with dimensions 5 x 5 x 5 cm according to ASTM D1621-16. PU pure was used as the reference foam. Table 1 shows the foam grouping .

All foams were characterized using FTIR (fourier transform infrared) to confirm the urethane compound, indicating successful polymerization. SEM (scanning electron microscope) was used to examine the morphology of the foam surface. The glass transition temperature (Tg) was analyzed using DSC (digital scanning calorimetry). TGA (thermogravimetric analyzer) to determine the thermal stability of the foam and compression test to determine the compressive strength of the foam.

Table 1. PU, PU-Mg, & PU-Zn foam grouping

Materials	1 wt. % Mg	2 wt. % Mg	3 wt. % Mg	1 wt. % Zn	2 wt. % Zn	3 wt. % Zn
PU Pure	-	-	-	-	-	-
PU-Mg1	√	-	-	-	-	-
PU-Mg2	-	√	-	-	-	-
PU-Mg3	-	-	√	-	-	-
PU-Zn1	-	-	-	√	-	-
PU-Zn2	-	-	-	-	√	-
PU-Zn3	-	-	-	-	-	√

3. RESULT AND DISCUSSION

3.1 FTIR (Fourier Transform Infrared) Analysis Result

The FTIR (fourier transform infrared) characterization aims to determine chemical compounds based on atomic bonds. Through this characterization, the functional groups formed in the composite material can also be seen.

Polyurethane is a polymer formed from the reaction between a polyol's OH (hydroxyl) group and with NCO (isocyanate functional group). In pure polyurethane (without adding other elements), the results of the FTIR test can be seen in Figure 1. There are two general methods to fabricate polyurethane foam, and both involve excessive diisocyanate on termination. The first method is pre-polymer termination using diisocyanate, and the second is polyol termination using diisocyanate, followed by adding a crosslinker [19]. The peak list is presented in Table .

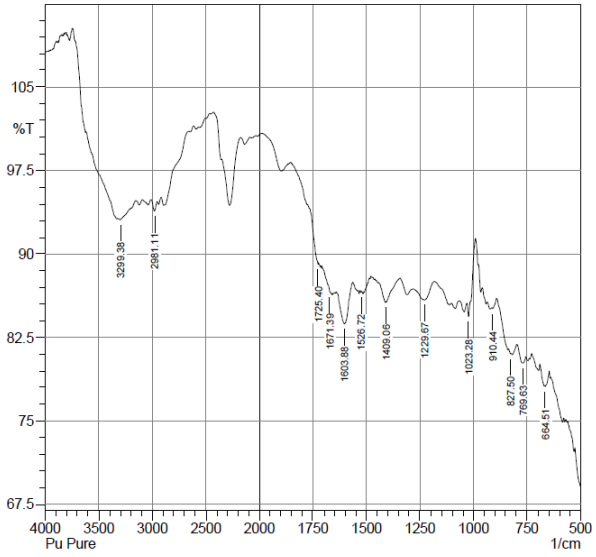

Figure 1. FTIR graph for pure polyurethane

There are three types of H-bonds in polyurethane, namely: an NH group that binds an H to one of three possible groups of proton acceptors; (a) carbonyl groups, (b) C-O-C polyethers, and (c) oxygen alkoxy urethanes [20]. In pure polyurethane foam, a stretching NH bond at 3299.38 cm^{-1} indicates the urethane compound.

Table 2. Peaks for pure polyurethane

Peak (cm^{-1})	Compound
910.44	C-O-C stretching
1023.28	Cyanate (-OCN dan C-OCN stretch)
1526.72	C-N stretching
1603.88	
1671.39	C=O stretching
1725.40	
2981.11	CH stretching
3299.38	NH stretching

3.1.1 FTIR of Polyurethane with Addition of Mg

The FTIR characterization was performed to determine the chemical compounds in the polyurethane mixture by adding magnesium (Mg) with a ratio of 1, 2, and 3 wt.% of Mg. The results of the FTIR characterization are shown in Figure 2.

Polyurethane itself is a polymer formed from the reaction between OH (hydroxyl) groups of polyols, which were shown at peaks of 3320.2038 cm^{-1} to 3323.0635 cm^{-1} (PU-Mg1-3), with NCO (groups of PU-Mg1-3). Isocyanate

function, shown at the peak of ~2269.2349 cm^{-1} in all PU-Mg foam. In all PU-Mg foam, NH stretching bonds showed at about 3017.0672 cm-1 to 3031.3661 cm^{-1}. C-O-C stretching bonds are shown at the peak of 1292.6202 cm^{-1} and 1294.0501 cm^{-1} for the three PU-Mg foam. In contrast, 1611.4856 cm^{-1} for PU-Mg1 and 1612.9155 cm^{-1} peaks for PU-Mg2 and PU-Mg3 showed the C=O stretching bond.

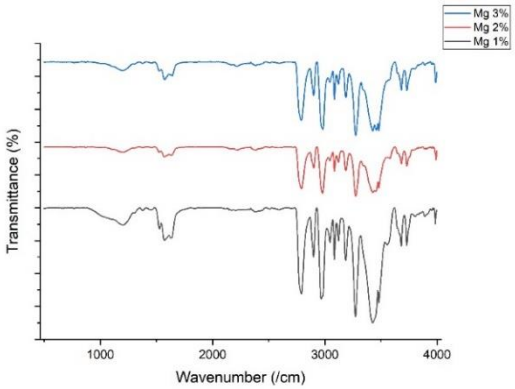

Figure 2. FTIR graph of polyurethane with addition of Mg

The FTIR spectral variations on C-O-C stretching, NH stretching, and C=O stretching can be used well as an indicator of the presence of H-bonds between oxygen alkoxy urethane and NH groups. Based on the results of the FTIR test in Table 3, the PU-Mg foam reveals several peaks with each type of bond.

Table 3. Peaks for polyurethane with Mg

Specimen	Peak (cm^{-1})	Compound
PU-Mg 1 wt.%	1112.4541	Cyanate (-OCN and C-OCN stretch)
	1294.0501	C-O-C stretching
	1611.4856	C=O stretching
	2269.2349	Isocyanate (-N=C=O stretch)
	3017.0672	NH stretching
	3320.2038	OH stretching
PU-Mg 2 wt.%	1111.0242	Cyanate (-OCN and C-OCN stretch)
	1292.6202	C-O-C stretching
	1612.9155	C=O stretching
	2296.4028	Isocyanate (-N=C=O stretch)
	3031.3661	NH strectching
	3323.0635	OH stretching
PU-Mg 3 wt.%	1292.6202	C-O-C stretching
	1612.9155	C=O stretching
	2269.4028	Isocyanate (-N=C=O stretch)
	3025.6465	NH strectching
	3323.0635	OH stretching

3.1.2 FTIR of Polyurethane with Addition of Zn

The FTIR test was carried out to determine the chemical compounds in the polyurethane mixture by adding zinc (Zn) with a ratio of 1, 2, and 3 wt.% Zn. The comparison of the FTIR test results to the specimens is shown in Figure 3.

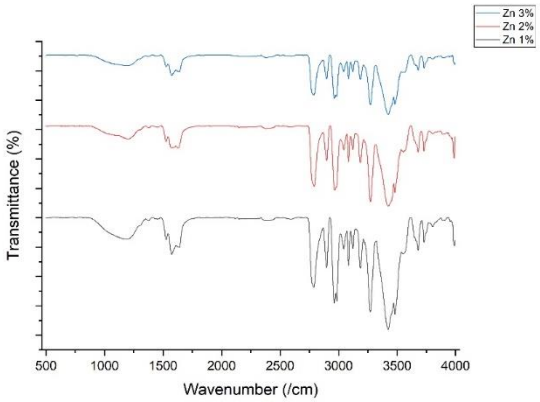

Figure 3. FTIR graph of polyurethane with addition of Zn

Table 4 shows the peak lists of polyurethane with the addition of Zn. PU-Zn foam shows several peaks with each type of bond. Polyurethane formed from the reaction between OH (hydroxyl) groups of polyols, shown at peaks of 3318.7739 cm^{-1} to 3321.6336 cm^{-1} (PU-Zn1-3), with NCO (groups PU-Zn1-3). The isocyanate function group was confirmed at 2269.2349 cm^{-1} in all three foams. The FTIR result also confirmed the presence of Zn in PU at peaks of 1542.8509 cm^{-1} for PU-Zn1, 1541,4210 cm-1 for PU-Zn2, and 1542.8509 cm^{-1} for PU-Zn3. It overlaps with the amide zone II.

In the three foams, NH stretching bonds at about 3015.6373 cm^{-1} and 3017.0672 cm^{-1}. C-O-C stretching bonds were shown at 1193.9578 cm^{-1} and 1295.48 cm^{-1} for PU-Zn2 and PU-Zn3. In comparison, ~1612.9155 cm^{-1} peak showed the C=O stretching bond for the three foams.

Table 4. Peaks for polyurethane with Zn

Specimen	Peak (cm^{-1})	Compound
PU-Zn 1 wt.%	1181.0885	Cyanate (-OCN dan C-OCN stretch)
	1612.9155	C=O stretching
	2269.2349	Isocyanate (-N=C=O stretch)
	3017.0672	NH stretching
	3321.6336	OH stretching
PU-Zn 2 wt.%	1112.4541	Cyanate (-OCN dan C-OCN stretch)
	1295.48	C-O-C stretching
	1611.4856	C=O stretching
	2269.2349	Isocyanate (-N=C=O stretch)
	3015.6373	NH strectching
	3318.7739	OH stretching
PU-Zn 3 wt.%	1112.4541	Cyanate (-OCN dan C-OCN stretch)
	1193.9578	C-O-C stretching
	1612.9155	C=O stretching
	2269.2349	Isocyanate (-N=C=O stretch)
	3015.6373	NH strectching
	3320.2038	OH stretching

3.2 Compression Test Analysis

The compression test used for rigid polymeric foam was in accordance with ASTM D1621-16. The test specimen is prepared in a cube shape or tube with a minimum area of 25,8 cm2 (4 in^2) and a maximum area of 232 cm^2 (36 in^2). The maximum height can't be more than the width or diameter of the specimen. The compression test determined the compressive strength of polyurethane with 1, 2, and 3 wt.% magnesium powder. The compression test result of the PU-Mg & PU-Zn group is shown in Figs 4 and 5.

For the PU-Mg group, the PU-Mg3 gave the highest compression strength at 0.84 MPa, while the PU-Zn3 gave the highest compression strength at 0.392 MPa, as shown in Fig. 5. The compression test results of PU-Mg and PU-Zn show a similar trend. The compressive strength increased along with the increasing amount of magnesium or zinc powder.

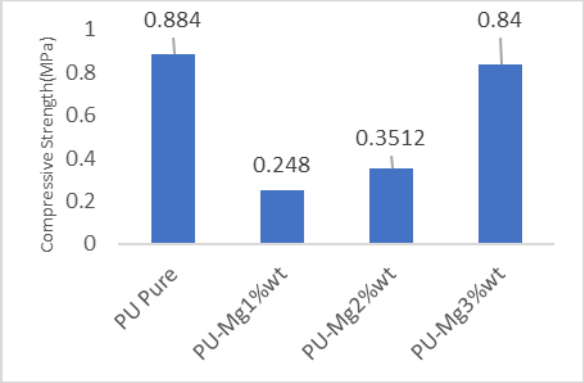

Figure 4. Compressive strength of PU-Mg

However, the PU Pure achieved the highest compression strength of all foams at 0.884 MPa. The lower compression strength of PU-Mg and PU-Zn compared to the PU pure was attributed to the weak interface between the additive and the matrix. The higher amount of incorporation of Mg and Zn powder into the PU matrix causes the additive to agglomerate due to the poor dispersion of the additive particle [21].

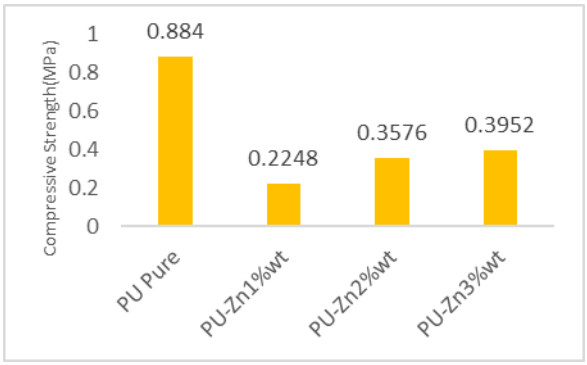

Figure 5. Compressive strength of PU-Zn

In general, inorganic fillers cause the foam cell to be more open, which lowers the mechanical properties. Moreover, the low compatibility between the inorganic fillers and the PU tends to cause cracking at the interfaces [22]

3.3 SEM (Scanning Electron Microscope) Analysis

SEM (scanning electron microscope) is used to observe the morphology of the foam surface.

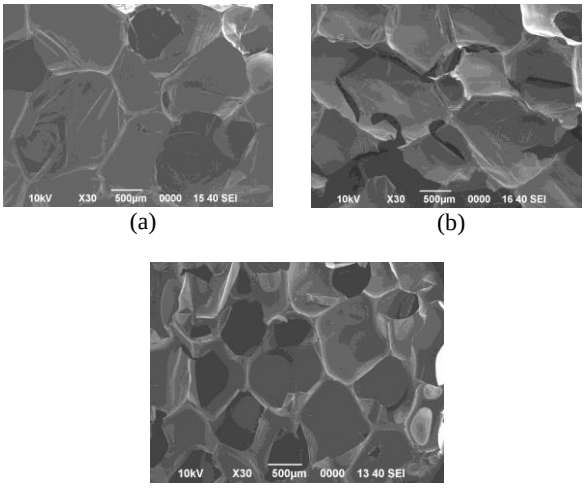

(a) (b)

(c)

Figure 6. SEM Results for polyurethane with Mg addition (wt.%); (a) 1, (b) 2, and (c) 3

The SEM results for polyurethane with the addition of magnesium (Mg) with a ratio of 1, 2, and 3wt.% Mg are shown in Fig. 6. SEM results of PU-Mg show a porous structure. Table 5 shows the more amount of magnesium added, the smaller the cell size of the foam.

Table 5. Polyurethane/Mg porosity

Mg Composition (wt.%)	Porosity (%)	Porosity length (µm)
1	88.816	1078.793
2	81.550	1050.352
3	81.209	1012.350

Changes in cell morphology characterized by changes in the size of small and large cells may be related to the presence of Mg, which affects the foaming process of PU/Mg [21].

Adding Mg of 3 wt.% will show a more distorted cell shape, damaged cell walls, and less homogeneous cell structures. The polyurethane morphology with the addition of 1, 2, and 3 wt.% zinc was shown in Fig. 7. Table 6 shows that the results of the SEM test of PU-Zn foam have a porous structure.

Polyurethane foam has a cellular structure and consists of partially open cells with circular holes. This result also shows that the greater the zinc

composition added, the smaller the porosity of the specimen. Zn particles act as the initial site of nucleation (cell formation).

Table 6. Polyurethane/Zn porosity

Zn composition (wt.%)	Porosity (%)	Porosity length (µm)
1	77.749	941.3328
2	77.571	881.9152
3	77.256	768.6748

However, at the same time, the addition of Zn will inhibit cell growth and produce smaller cell sizes [23].

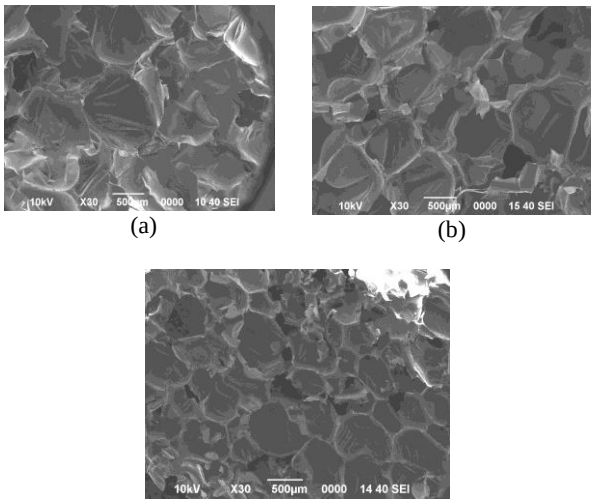

(a) (b) (c)

Figure 7. SEM results for polyurethane with Zn addition (wt.%); (a) 1, (b) 2, and (c) 3

3.4 DSC (Differential Scanning calorimetry) Analysis

The DSC (differential scanning calorimetry) characterization was performed from 40 °C to 350 °C with a heating rate of 5 °C/min. The results of the DSC test are in the form of a thermogram that can provide information about the thermal properties of a polymer, which is Tg in each foam. The foam used for testing has a minimum weight of 3 mg.

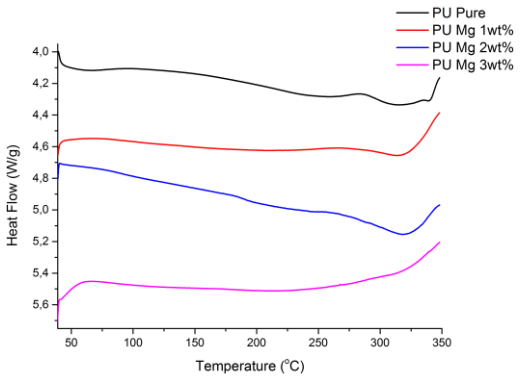

Figure 8. DSC result of PU Pure and PU-Mg series

Variations in the addition of the amount of magnesium and the amount of zinc were used to identify the trend of each of these variations. The results of the DSC are shown in Figs. 8 and 9.

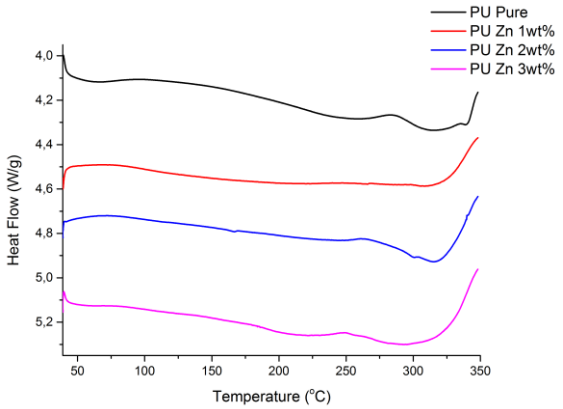

Figure 9. DSC result of PU Pure and PU-Zn series

Table 7 shows that the more Mg or Zn is added, the higher the glass transition temperature (Tg). The increases in the concentration of the additives reduce the molecular mobility of the matrix, which results in the shift of the foams Tg to a higher temperature [24]. The DSC result also supports the SEM test results shown in Fig. 6 and Fig. 7 because the pore size gets smaller with the addition of Mg or Zn, so the mobility of the molecule is limited.

Table 7. Glass transition temperature (Tg) for each foams

Materials	Tg (°C)
PU Pure	112.8
Mg 1 wt.%	124.16
Mg 2 wt.%	189.66
Mg 3 wt.%	185.92
Zn 1 wt.%	120.13
Zn 2 wt.%	122.60
Zn 3 wt.%	159.40

3.5 TGA (Thermogravimetric Analysis) Result

The TGA (thermogravimetric analysis) was performed by heating the foam from 40 to 450 °C at a heating rate of 5 °C/min.

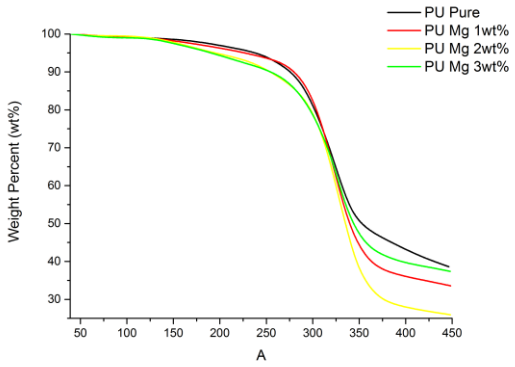

Figure 10. TGA result of polyurethane with Mg

The TGA results show how much the material decomposes as it's heated [25].

Figure 10 and Figure 11 show the result of TGA. The decomposition temperature for all foams is shown in Table 8. The initial decomposition temperature shows a 5 wt.% decrease in the foam weight due to the evaporation of water vapor contained in the foam.

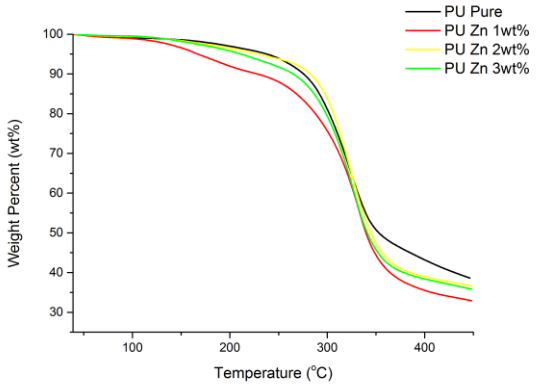

Figure 11. TGA result of polyurethane with Zn

PU Pure foam shows the highest temperature at 237.97 °C, while PU-Mg1 shows the lowest temperature at 166.96 °C. The decomposition peak temperature shows the degradation temperature of polyurethane's soft segment, which consists of the polyol part. The PU-Mg & PU-Zn series foam has a higher temperature than the PU pure, indicating that the incorporation of additives could increase the PU foam's thermal stability [19].

Table 8. Decomposition temperature for each foam

Composition	Initial Decomposition Temperature (°C)	Decomposition peak temperature (°C)	Weight Loss (%)
PU Pure	237.97	350.30	61.384
Mg 1 wt.%	227.05	363.79	54.940
Mg 2 wt.%	195.15	373.94	57.073
Mg 3 wt.%	190.37	380.19	47.856
Zn 1 wt.%	166.96	356.38	50.946
Zn 2 wt.%	228.86	369.41	52.168
Zn 3 wt.%	211.46	374.36	50.488

4. CONCLUSION

The effect of adding of magnesium or zinc to the polyurethane foam, which would serve as a potential aneurism clip material, was detailed. Several tests were conducted to know the mechanical and thermal properties. All foams show the bond between hydroxyl and isocyanate function on FTIR (fourier transform infrared) testing resulting from polyurethane foam formation. Adding 1, 2, and 3 wt.% of magnesium will increase the compressive strength, glass transition temperature (Tg), initial decomposition temperature, decomposition peak temperature, and weight loss, also decreasing the porosity area and length. As well as the addition of 1, 2, and 3 wt.% zinc will also increase the compressive strength and glass transition temperature (Tg), decreasing the porosity area and length, initial decomposition temperature, decomposition peak temperature, and weight loss. The polyurethane foam, with the addition of 3 wt.% magnesium (PU-Mg3), achieves the best result with a compressive strength of 0.84 MPa.

ACKNOWLEDGMENT

The author thanks to Erika Satriana and Farah Zafira Rennu for the helps in several experiments on this study.

REFERENCES

[1] D. F. Louw, W. T. Asfora, and G. R. Sutherland, "A brief history of aneurysm clips.," *Neurosurg. Focus*, vol. 11, no. 2, 2001. Doi: 10.3171/foc.2001.11.2.5.

[2] J. P. Mohr, P. A. Wolf, J. A. Grotta, M. A. Moskowitz, M. Mayberg, and R. von Kummer, *Stroke: Pathophysiology, Diagnosis, and Management*. Elsevier, pp. 589-613, 2011.

[3] S. Marbacher, F. Strange, J. Frösén, and J. Fandino, "Preclinical extracranial aneurysm models for the study and treatment of brain aneurysms: A systematic review," *J. Cereb. Blood Flow Metab.*, vol. 40, no. 5, pp. 922-938, 2020. Doi: 10.1177/0271678X20908363.

[4] H. Y. Um, B. H. Park, D. H. Ahn, M. I. Abd El Aal, J. Park, and H. S. Kim, "Mechanical and biological behavior of ultrafine-grained Ti alloy aneurysm clip processed using high-pressure torsion," *J. Mech. Behav. Biomed. Mater.*, vol. 68, no. September 2016, pp. 203-209, 2017. Doi: 10.1016/j.jmbbm.2017.02.002.

[5] F. Jumah, T. Quinoa, O. Akel, V. Narayan, N. Adeeb, G. Gupta, and A. Nanda, "The origins of eponymous aneurysm clips: A review," *World Neurosurg.*, vol. 134, pp. 518-531, 2020. Doi: 10.1016/j.wneu.2019.09.061.

[6] S. Liu and Y. C. Shin, "Additive manufacturing of Ti6Al4V alloy: A review," *Mater. Des.*, vol. 164, p. 107552, 2019. Doi: 10.1016/j.matdes.2018.107552.

[7] L.-C. Zhang and H. Attar, "Selective laser melting of titanium alloys and titanium matrix composites for biomedical applications: A review," *Adv. Eng. Mater.*, vol. 18, no. 4, pp. 463-475, 2016. Doi:

10.1002/adem.201500419.
[8] M. Geetha, A. K. Singh, R. Asokamani, and A. K. Gogia, "Ti based biomaterials, the ultimate choice for orthopaedic implants – A review," *Prog. Mater. Sci.*, vol. 54, no. 3, pp. 397-425, 2009. Doi: 10.1016/j.pmatsci.2008.06.004.
[9] A. Brack, S. Senger, G. Fischer, H. Janssen, J. Oertel, and C. Brecher, "Development of an artifact-free aneurysm clip," *Curr. Dir. Biomed. Eng.*, vol. 2, no. 1, 2016. Doi: 10.1515/cdbme-2016-0120.
[10] H. Demirturk Kocasarac, G. Ustaoglu, S. Bayrak, R. Katkar, H. Geha, S. Thomas Feahl, B. L Mealy, M. Danaci, and M. Noujeim, "Evaluation of artifacts generated by titanium, zirconium, and titanium–zirconium alloy dental implants on MRI, CT, and CBCT images: A phantom study," *Oral Surg. Oral Med. Oral Pathol. Oral Radiol.*, vol. 127, no. 6, pp. 535-544, 2019. Doi: 10.1016/j.oooo.2019.01.074.
[11] K. Ito, T. Seguchi, T. Nakamura, A. Chiba, T. Hasegawa, A. Nagm, T. Horiuchi, K. Hongo, "Evaluation of metallic artifacts caused by nonpenetrating titanium clips in postoperative neuroimaging," *World Neurosurg.*, vol. 96, pp. 16-22, 2016. Doi: 10.1016/j.wneu.2016.08.086.
[12] F. Khursheed, F. Rohlffs, S. Suzuki, D. H. Kim, and T. M. Ellmore, "Artifact quantification and tractography from 3T MRI after placement of aneurysm clips in subarachnoid hemorrhage patients," *BMC Med. Imaging*, vol. 11, no. 1, p. 19, 2011. Doi: 10.1186/1471-2342-11-19.
[13] L. Sonnow, S. Könneker, P. M. Vogt, F. Wacker, and C. Valcs, "Biodegradable magnesium Herbert screw – image quality and artifacts with radiography, CT and MRI," *BMC Medical Imaging*., pp. 17:16, 2017. Doi: 10.1186/s12880-017-0187-7.
[14] L. Sonnow, A. Ziegler, G. H. Pöhler, M. H. Kirschner, M. Richter, M. Cetin, M. Unal, and O. Kose, "Alterations in magnetic resonance imaging characteristics of bioabsorbable magnesium screws over time in humans: a retrospective single center study," *Innov Surg Sci*., pp. 105-113, 2017. Doi: 10.1515/iss-2021-0032.
[15] T. Wang, S. Inubushi, N. Ikeo, T. Mukai, K. Okumura, H. Akasaka, R. Yada, K. Yoshida, D. Miyawaki, T. Ishihara, A. Nakaoka, and R. Sasaki, "Novel artifact-robust and highly visible zinc solid fiducial marker for kilovoltage x-ray image-guided radiation therapy," *Med Phys*., vol 47, no 10, pp 4703-4710, 2020. Doi:10.1002/mp.14412.
[16] A. K. Mishra, P. Chalise, R. P. Singh, and R. K. Shah, "The proximal femur--a second look at rational of implant design," *Nepal Med. Coll. J.*, vol. 11, no. 4, pp. 278-280, 2009.
[17] W. S. Cho, K. I. Cho, J. E. Kim, T. S. Jang, E. J. Ha, H. S. Kang, Y. J. Son, S. H. Choi, S. Lee, C. C. Kim, J. Y. Sun, and H. E. Kim, "Zirconia-Polyurethane Aneurysm Clip," *World Neurosurg.*, vol. 115, pp. 14-23, 2018. Doi: 10.1016/j.wneu.2018.03.130.
[18] J. Kucinska-Lipka, I. Gubanska, and M. Sienkiewicz, "Thermal and mechanical properties of polyurethanes modified with L-ascorbic acid," *J. Therm. Anal. Calorim.*, vol. 127, no. 2, pp. 1631-1638, 2017. Doi: 10.1007/s10973-016-5743-9.
[19] A. N. Roziafanto, M. S. Dwijaya, R. Yunita, M. Amrullah, and M. Chalid, "Synthesis hybrid bio-polyurethane foam from biomass material," *Proceedings of the 5th International Symposium on Applied Chemistry 2019, AIP Conference Proceedings 2175*, p. 020068, 2019. Doi: 10.1063/1.5134632.
[20] J. Bandekar and S. Klima, "FT-IR spectroscopic studies of polyurethanes Part I. Bonding between urethane C-O-C groups and the NH Groups," *J. Mol. Struct.*, vol. 263, pp. 45–57, 1991, Doi: 10.1016/0022-2860(91)80054-8.
[21] S. A. Adnan, N. H. A. Zaidi, Y. M. Daud, and F. Zainuddin, "The effect of magnesium content on the properties of palm oil based polyurethane foam," *AIP Conference Proceedings 2030*, p. 020050, 2018. Doi: 10.1063/1.5066691.
[22] S. Yi, Y-J. Cho, and J-S. Roh, "Improved dimensional stability of water-blownpolyurethane foam with aluminum hydroxide and magnesium hydroxide," *J Appl Polym Sci.*, vol 137, no 46, p. 49510, 2020. Doi: 10.1002/app.49510.
[23] S. El Mogy, "Processing of polyurethane nanocomposite reinforced with nanosized zinc oxide: Effect on mechanical and acoustic properties," *Egypt. J. Chem.*, vol 62, no. 2, pp 333-341, 2018. Doi: 10.21608/ejchem.2018.4655.1410.
[24] J. Tomaszewska, T. Sterzyński, A. Woźniak-Braszak, and M. Banaszak,

"Review of recent developments of glass transition in PVC nanocomposites," *Polymers (Basel).*, vol. 13, no. 24, p. 4336, 2021. Doi: 10.3390/polym13244336.

[25] D. Filip, D. Macocinschi, and S. Vlad, "Thermogravimetric study for polyurethane materials for biomedical applications," *Compos. Part B Eng.*, vol. 42, no. 6, pp. 1474-1479, 2011. Doi: 10.1016/j.compositesb.2011.04.050.

Metalurgi (2022) 2: 49 - 56

METALURGI
Majalah Ilmu dan Teknologi
p-ISSN 0126-3188 | e-ISSN 2443-3926
ejurnalmaterialmetalurgi.lipi.go.id

HARDNESS AND CORROSION BEHAVIOR OF Ti-20Cu-20Ni-20Mn-20Zn AS HIGH ENTROPY ALLOY AND TI-13Cu-9Ni-5Mn-5Zn FOR MARINE STRUCTURE APPLICATION

Muhammad Azhar Ariefkha Dani[a,*], Bonita Dilasari[a], Yudi Nugraha Thaha[b], Ika Kartika[b], Fendy Rokhmanto[b]

[a] Department of Metallurgical Engineering, Bandung Institute of Technology
Jl. Ganesha 10, Bandung, Indonesia 40132
[b] Research Center for Metallurgy, National Research and Innovation Agency
Management Building 720, B.J. Habibie Sains and Technology Area, Banten, Indonesia 15343
*E-mail: m.azhar.ariefkha.dani@gmail.com

Received: 23-03-2022, Revised: 19-07-2022, Accepted: 04-10-2022

Abstract

Beta titanium alloys and titanium high entropy alloys are promising candidates for marine structural applications. This study aims to compare Ti-20Cu-20Ni-20Mn-20Zn high entropy alloy and Ti-13Cu-9Ni-5Mn-5Zn beta titanium alloy on microstructure, mechanical properties, and corrosion behavior in a 3.5% NaCl solution. Ti-20Cu-20Ni-20Mn-20Zn and Ti-13Cu-9Ni-5Mn-5Zn were produced by powder metallurgy. In the experimental results, it was observed that Ti-20Cu-20Ni-20Mn-20Zn alloy, as a high entropy alloy, has a low hardness value of 190.658 HV and a high corrosion rate of 1.7992 mm/year. The Ti-13Cu-9Ni-5Mn-5Zn alloy as the beta-titanium alloy has a high hardness value of 430.736 HV and a low corrosion rate of 0.12121 mm/year. The results indicate that Ti-13Cu-9Ni-5Mn-5Zn has better corrosion resistance in 3.5% NaCl solution and hardness than Ti-20Cu-20Ni-20Mn-20Zn high entropy alloy.

Keywords: *Beta-titanium, high entropy alloys, powder metallurgy, corrosion, marine structure application*

1. INTRODUCTION

Since the 1950s, titanium alloys have been developed as structure materials for marine facilities, especially for ship hulls, marine power systems, and pipes. Marine titanium alloys mostly contain aluminum and molybdenum upon optimum doping with an adaptive strengthening of the hexagonal crystalline lattice (α-Ti). α-Ti is chosen because it has good weldability, which enables the production of large-size welded structures without additional thermal processing to remove residual welding stress [1]. However, α-Ti has low strength properties, is brittle, unable to heat treatment, and has a low forming ability [2].

Besides that, beta titanium (β-Ti) is one phase of titanium alloys that usually contains vanadium (V), molybdenum (Mo), niobium (Nb), and tantalum (Ta) [2]. It has been used in applications that demand high strength, good corrosion resistance, excellent biocompatibility, good ductility, good weldability, good stability at a temperature above 315 ºC, and ease of fabrication [2], [3]. Moreover, the β-Ti alloy has better formability and is easier to fabricate than the alpha phase titanium [2]. β-Ti alloys such as Ti-8Mn, Ti-45Nb, Ti-15Mo-5Zr, Ti-11.5Mo-6Zr-4.5Sn, and Ti-35V-15Cr have good corrosion resistance to Cl^- ions and show good corrosion resistance for marine applications [4]. β-Ti alloy properties provide significant advantages over other high-performance alloys. However, the main drawback of β-Ti alloys is their high cost due to increase raw materials cost [5].

On the other hand, high entropy alloys are currently of great research interest in materials science and engineering [6]. High entropy alloys are alloys designed to combine at least five essential elements in relatively high concentrations (5–35 at.%) compared to

DOI : 10.14203/metalurgi.v37i2.636

conventional alloys that have only one or two basic elements [6]–[11]. High entropy alloys have recently been developed due to their high strength properties, good corrosion resistance, and ease of fabrication [7], [12]. High entropy alloys recently being developed are Ti-Zr-Cu-Ni-Be alloy, 0.5Al-Co-Cr-Cu-Fe-Ni-0.2Ti alloy, Ta-Nb-Hf-Zr-Ti alloy, and Ta-Nb-V-Ti alloy [8]. To the best of our knowledge, there are still few studies on high entropy alloys using titanium in 2022, and no research on Ti-Cu-Ni-Mn-Zn high entropy alloy has been discovered.

The powder metallurgy method was used to create Ti-20Cu-20Ni-20Mn-20Zn high entropy alloy and Ti-13Cu-9Ni-5Mn-5Zn β-Ti alloy in the current work. Because of the uniform composition, metal savings, and lower processing costs, the powder metallurgy method was used for alloy production [13]. Copper (Cu), nickel (Ni), manganese (Mn), and zinc (Zn) are inexpensive alloying elements for the synthesis of beta titanium and high entropy alloy. Cu, Ni, and Mn are eutectoid elements forming beta-phase titanium [3]. Zinc (Zn) was selected to decrease the sintering temperature of the powder metallurgy process [14]. NaCl 3.5% is commonly used standard solution for marine corrosion simulation [1].

This study aims to compare the microstructure, mechanical properties, and corrosion behavior Ti-20Cu-20Ni-20Mn-20Zn high entropy alloy and Ti-13Cu-9Ni-5Mn-5Zn β-Ti alloy on their in a 3.5% NaCl solution for marine structure application.

2. MATERIALS AND METHODS

2.1 Materials

Powder metallurgy method was used to create Ti-20Cu-20Ni-20Mn-20Zn and Ti-13Cu-9Ni-5Mn-5Zn alloy compositions. Titanium, copper, nickel, manganese, and zinc (Merck, p.a grade) was precisely weighed and mixed for 5 minutes in mortar. It was then compacted for 30 seconds using Enerpac GP-105 at 500 MPa pressure to form a compact cylinder with a 1 cm diameter and 5 mm height. The compacted sample was sintered using GSL-1100X at 880 °C for 3 hours before being cooled to room temperature in an argon atmosphere in a quartz tube. The samples were polished on the Grinder Polisher-1B with water flowing through it using emery papers up to 2000 grit. This study used a Kroll solution consisting of 6 mL HNO3, 3 mL HF, and 100 mL H2O as the etching solution.

2.2 Characterization

The microstructure of Ti-20Cu-20Ni-20Mn-20Zn and Ti-13Cu-9Ni-5Mn-5Zn samples were characterized by JEOL JSM-6390A SEM-EDS (scanning electron microscope-energy dispersive spectroscopy).

Ti-20Cu-20Ni-20Mn-20Zn and Ti-13Cu-9Ni-5Mn5Zn alloys were investigated by Rigaku Smartlab XRD (x-ray diffraction) with Cu-Kα to identify the phase that was formed after the sintering process.

The Vickers Micro Hardness test was performed The Vickers Micro Hardness test was carried out at Mitutoyo AR Hardness with a loading of 0.3 KN and a loading speed of 12 seconds. The hardness test was carried out eight times on the surface of the specimen with a horizontally parallel pattern at Mitutoyo AR Hardness with a loading of 0.3 KN and a loading speed of 12 seconds. The hardness test was carried out eight times on the surface of the specimen with a horizontally parallel pattern.

Potentiodynamic polarization and EIS (electrochemical impedance spectroscopy) were used to investigate corrosion behavior in a 3.5% NaCl solution using a three-electrode system, with the samples serving as working electrodes, Ag/AgCl (KCl 1 M) serving as the reference electrode, and a platinum plate serving as the counter electrode. For marine environment simulation, a 3.5% NaCl solution at room temperature (25 °C) was used. Autolab 302 Multi BA was used to perform the electrochemical measurements. The potentiodynamic polarization was performed at a scan rate of 0.001 V/s, with an initial potential of -0.42 V vs OCP (open circuit potential) and a final potential of 0.95 V vs OCP. The EIS was taken 120 seconds after immersion to determine the OCP. The OCP determination time was chosen because the average OCP had a stable value with a deviation of less than 5% from t = 0 s to t = 120 s. The stability of the average OCP value indicates that the TiO_2 film on the titanium surface is growing slowly and that the titanium surface is stable. The OCP stability as a function of time in titanium alloys in 3.5% NaCl solution has also been reported [16]. The EIS was performed with a frequency range of 100 kHz - 0.05 Hz and an amplitude of 10 mV about OCP. Nova 1.1 examined the electrochemical parameter.

3. RESULT AND DISCUSSION

3.1 Microstructure and Phase Analysis

Figure 1 shows SEM-EDS (scanning electron microscope-energy dispersive spectroscopy) observation Ti-Cu-Ni-Mn-Zn alloy after sintering

at 880 °C for 3 hours. Ti-20Cu-20Ni-20Mn-20Zn alloy exhibits eutectoid structure clearly seen in Fig. 1(a). The eutectoid structure is most likely due to the high Zn concentration. Figure 1(b) depicts a Ti-13Cu-9Ni-5Mn-5Zn alloy with a -Ti microstructure β-Ti [17].

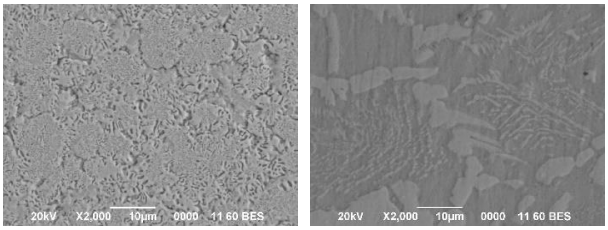

(a) (b)

Figure 1. SEM-EDS image of (a) Ti-20Cu-20Ni-20Mn-20Zn, and (b) Ti-13Cu-9Ni-5Mn-5Zn, after sintering at T = 880 °C for 3 hours

Figure 2 depicts SEM mapping of a high entropy Ti-20Cu-20Ni-20Mn-20Zn alloy. Titanium was found to be uniformly distributed. The Ti-rich matrix contained a uniform distribution of Ni, Mn, and Zn. Meanwhile, in the Ti-rich matrix, Cu was unequally distributed. According to the SEM-EDS mapping profile, Ti forms intermetallic with Ni, Mn, and Zn.

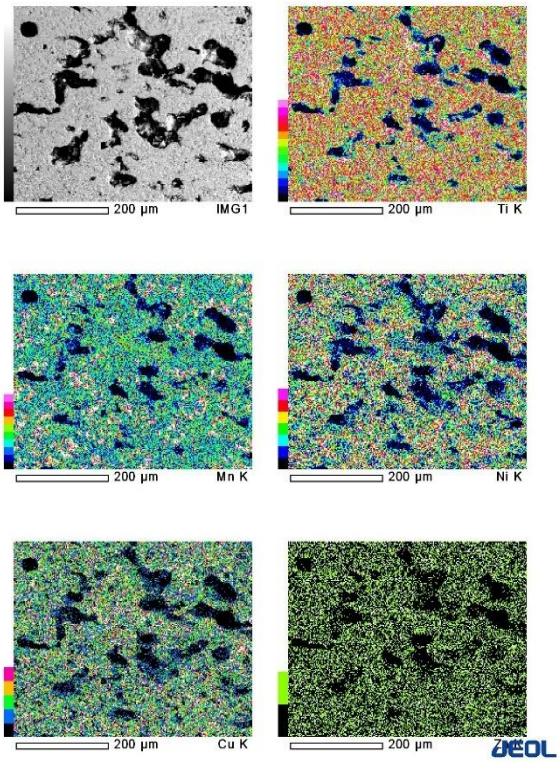

Figure 2. SEM-EDS mapping of Ti-20Cu-20Ni-20Mn-20Zn alloy after sintering at T = 880 °C for 3 hours

Figure 3 depicts SEM mapping of a Ti-13Cu-9Ni-5Mn-5Zn-Ti alloy after 3 hours of sintering at T = 880 °C. The Ti matrix was found to be segregated. Mn and Zn were found in the Ti-rich matrix, but less of Cu and Ni. Cu was observed along grain boundaries. A trace of Ti was discovered in the Cu matrix. Ti tends to form intermetallic with Mn and Zn in the Ti-13Cu-9Ni-5Mn-5Zn alloy, according to the SEM-EDS mapping profile (Fig. 3). Ti-20Cu-20Ni-20Mn-20Zn and Ti-13Cu-9Ni-5Mn-5Zn have distinct microstructures, particularly in terms of Cu phase distribution.

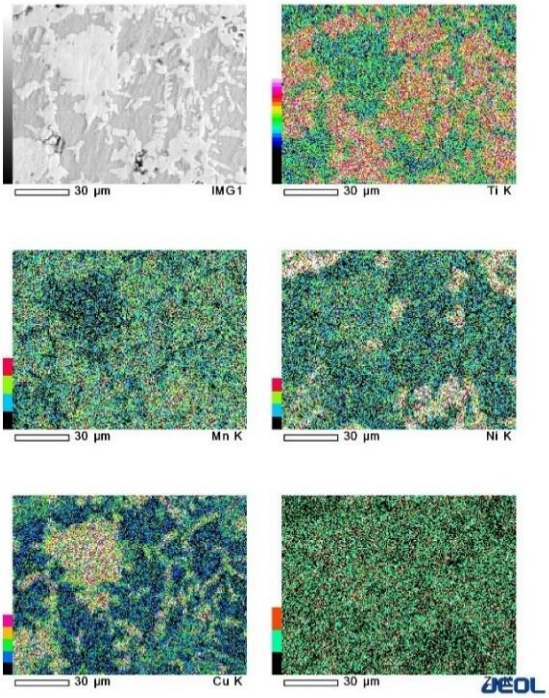

Figure 3. SEM-EDS mapping of Ti-13Cu-9Ni-5Mn-5Zn alloy after sintering at T = 880 °C for 3 hours

Phase analysis of the XRD (x-ray diffraction) results on Ti-20Cu-20Ni-20Mn-20Zn and Ti-13Cu-9Ni-5Mn-5Zn after sintering at a temperature of 880 °C for 3 hours can be seen in Fig. 4. X-ray diffractogram of Ti-20Cu-20Ni-20Mn-20Zn alloy shows the presence of α-Ti, TiNi, Ti_2Ni, $TiZn_2$, $TiMn_2$, and Cu, following the result of phase diagram analysis [14], [18]-[20]. The Cu phase (cubic structure and cell parameters a=b=c=2.561), intermetallic TiNi (hexagonal structure and cell parameters a=4.6460; b=4.1080; c=2.8980), and intermetallic $TiZn_2$ (hexagonal structure and cell parameters a=5.0640; c=8.2100) have the highest intensity in the Ti-20Cu-20Ni-20Mn-20Zn. The second highest intensity (2=44.88°) is found in the intermetallic TiNi phase (hexagonal structure and cell parameters a=4.6460; b=4.1080; c=2.8980) and the intermetallic $TiMn_2$ phase (hexagonal structure and cell parameters a=4.8200; c=7.9150). The third highest intensity is the intermetallic Ti_2Ni phase (2θ=41.57º) with a cubic structure and cell parameters a=b=c= 11.3193. The fourth intensity is the intermetallic

TiNi phase (2θ=41.06º) with a hexagonal structure and cell parameter a=4.6460; b=4.1080; c=2.8980. The fifth intensity (2θ=39.11º) is the α-Ti phase (hexagonal structure and cell parameter a=2.934; b=2.934; c=4.657), intermetallic TiNi (hexagonal structure and cell parameter a=4.6460; b=4.1080; c=2.8980) and intermetallic Ti_2Ni (cubic structure and cell parameters a=b=c=11.3193).

On the other hand, the x-ray diffractogram of Ti-13Cu-9Ni-5Mn-5Zn alloy shows the presence of β-Ti, $TiZn_2$, Ti_3Cu, TiNi, $TiMn_2$, and Cu, by the result of phase diagram analysis as shown at Fig. 3 [14], [18]-[19], [21]. The one dominant peak, namely the intermetallic Ti_3Cu phase, is located at 2θ=39,57º (hexagonal structure and cell parameter a=4.1580; c=3.5940). The second peak is the intermetallic TiNi phase, which is located at 2θ=41.06º (hexagonal structure, and cell parameter a=4.6460; b=4.1080; c=2.8980). The third peak (2θ=38.47º) is the β-Ti phase (cubic structure and cell parameters a=b=c=2.941) and the intermetallic $TiZn_2$ (hexagonal structure and cell parameters a=5.0640; c=8.2100).

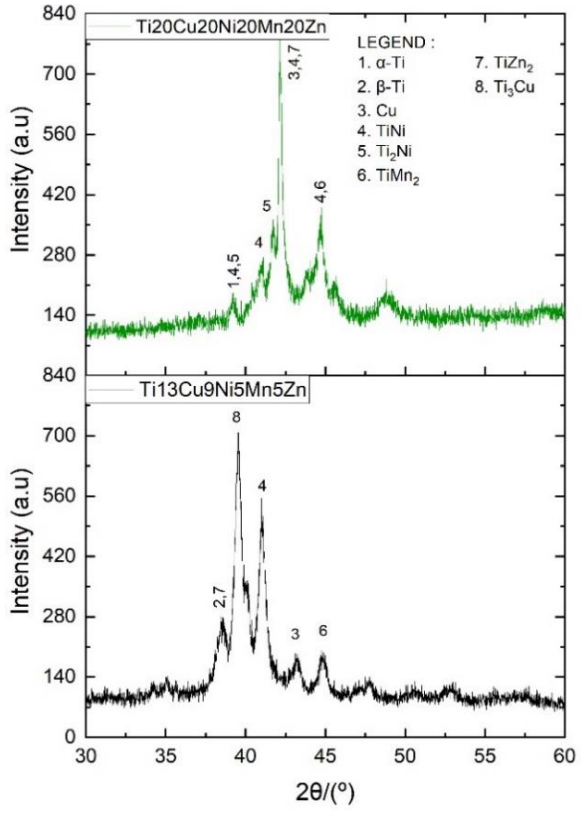

Figure 4. X-ray diffraction pattern of Ti-20Cu-20Ni-20Mn-20Zn and Ti-13Cu-9Ni-5Mn-5Zn alloys after sintered at T= 880 °C for 3 hours

The $TiMn_2$ intermetallic phase is located at 2=44.88° (hexagonal structure, and cell parameters a=4.8200; c=7.9150). The fifth peak, at 2=43.29° (cubic structure and cell parameters a=b=c=2.561), is the Cu elemental phase.

Based on XRD analysis, it is confirmed that α-Ti was formed in Ti-20Cu-20Ni-20Mn-20Zn, while β-Ti was formed in Ti-13Cu-9Ni-5Mn-5Zn. It is well known that α-Ti alloys have low strength properties and are less ductile compared to β-Ti alloys due to the hexagonal closed package structure. β-Ti alloys, which have a BCC (body-centered cubic) structure, tend to have high specific properties, high fatigue, high-temperature, corrosion, and high ductility [2]. Cu elemental phase in the Ti-20Cu-20Ni-20Mn-20Zn high entropy alloy was observed at a higher concentration and intensity than the Ti-13Cu-9Ni-5Mn-5Zn alloy. Based on SEM-EDS mapping and XRD results, it can be seen that the Ti-20Cu-20Ni-20Mn-20Zn and Ti-13Cu-9Ni-5Mn-5Zn alloys have a significant difference in phase concentration and phase distribution of intermetallic titanium and titanium elemental.

3.2 Hardness Result

The hardness value of Ti-20Cu-20Ni-20Mn-20Zn high entropy alloy and Ti-13Cu-9Ni-5Mn-5Zn beta titanium alloy after sintering at a temperature of 880 °C for 3 hours can be seen in Fig. 5. The hardness value of Ti-20Cu-20Ni-20Mn-20Zn was 190.658 HV and Ti-13Cu-9Ni-5Mn-5Zn was 430.736 HV. This could be due to the high intensity of the Cu elemental phase and the low intensity of the α-Ti phase in the Ti-20Cu-20Ni-20Mn-20Zn alloy. The low concentration of the α-Ti phase is likely because titanium tends to form an intermetallic phase with Ni, Mn, and Zn. It's well known that α-Ti has less strength and is brittle [2], and intermetallic Zn exhibit lower hardness than titanium [22]. Contrary to Ti-13Cu-9Ni-5Mn-5Zn alloy, a less intermetallic phase of titanium with Cu, Ni, Mn, and Zn was formed so that a higher β-Ti phase was observed. β-Ti has more strength and ductility [2], [3]. Besides that, Ti-20Cu-20Ni-20Mn-20Zn has more porosity on the surface than Ti-13Cu-9Ni-5Mn-5Zn. The hardness test result confirmed that lower single phase concentration and higher intermetallic phase concentration results in a softer alloy.

A. S. Oryshchenko et al., reported commercial titanium marine with hardness value [1]. The Ti40Al10V alloy reported have hardness value of 250 HV, the Ti6Al4V6Mo alloy reported have hardness value of 60.87 HV, and the Ti3Al8V4Mo4Zr alloy reported have hardness value of 118 HV [23]–[25]. From this comparison, Ti-13Cu-9Ni-5Mn-5Zn is a

promising candidate for marine structure because it has a higher hardness.

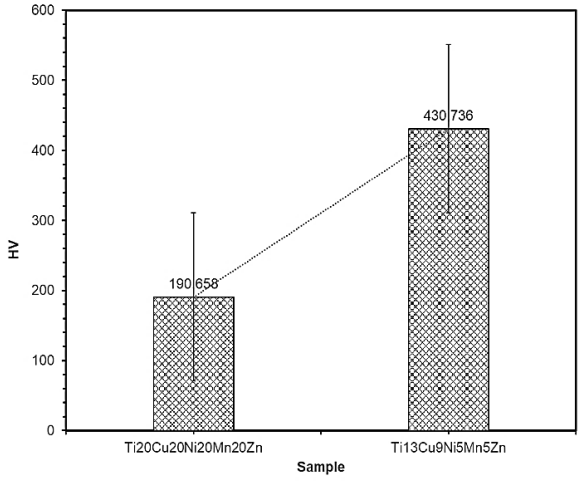

Figure 5. The hardness value comparison between Ti-20Cu-20Ni-20Mn-20Zn and Ti-13Cu-9Ni-5Mn-5Zn after sintered at T= 880 °C for 3 hours

Hence, it is expected to be more resistant to friction and plastic deformation.

3.3 Electrochemical Measurements Analysis

Potentiodynamic polarization was used to determine the corrosion potential and corrosion current density of Ti-Cu-Ni-Mn-Zn alloys in a 3.5% NaCl solution. Figure 6 shows the potentiodynamic polarization results of the two samples in a 3.5% NaCl solution. Both samples showed an active-passive corrosion behavior. Corrosion potential and current density obtained from Tafel extrapolation are presented in Table 1. Ti-13Cu-9Ni-5Mn-5Zn alloy showed a more positive corrosion potential and a lower corrosion current density than that of Ti-20Cu-20Ni-20Mn-20Zn alloy, which indicates that Ti-13Cu-9Ni-5Mn-5Zn alloy is nobler and has better corrosion resistance in a 3.5% NaCl solution compared to Ti-20Cu-20Ni-20Mn-20Zn.

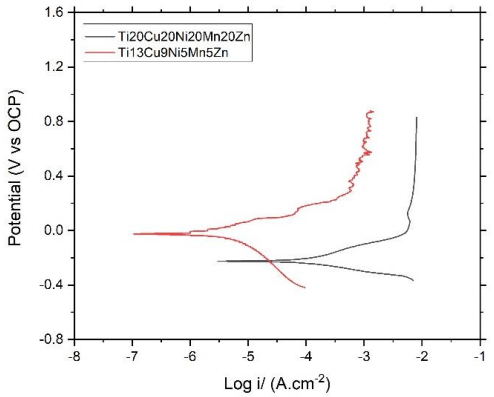

Figure 6. Potentiodynamic polarization of each composition of Ti-Cu-Ni-Mn-Zn alloy after sintered at T= 880 °C for 3 hours

Corrosion rate values of the Ti-20Cu-20Ni-20Mn-20Zn high entropy alloy and the Ti-13Cu-9Ni-5Mn-5Zn alloy calculated from the corrosion current density were 1.799 mm/year and 0.121 mm/year, respectively. That was reported that beta titanium has a stable oxide form [26]. Due to the presence of multiple elements in Ti-20Cu-20Ni-20Mn-20Zn alloy, titanium oxide film tends to be inhomogeneous (non-uniform). The inhomogeneous oxide film in Ti-20Cu-20Ni-20Mn-20Zn alloy is more reactive to Cl^- ion than the titanium oxide film that of Ti-13Cu-9Ni-5Mn-5Zn.

Table 1. Corrosion rate of the Ti-Cu-Ni-Mn-Zn alloy after sintered at T= 880 °C for 3 hours

Samples	E_{corr} (V vs. OCP)	I_{corr} ($\mu A/cm^2$)	Corrosion Rate (mm/y)
Ti-20Cu-20Ni-20Mn-20Zn	-0.225	117.130	1.7992
Ti-13Cu-9Ni-5Mn-5Zn	-0.018	7.891	0.1212

Ti-13Cu-9Ni-5Mn-5Zn alloy thermodynamically. However, it must not be that the Ti-13Cu-9Ni-5Mn-5Zn alloy possesses a lower current density compared to the Ti-20Cu-20Ni-20Mn-20Zn alloy. Due to the small current density, kinetically, the tendency of mass loss for pitting formation in Ti-13Cu-9Ni-5Mn-5Zn alloy was very slow. From the above results, it can be concluded that the Ti-13Cu-9Ni-5Mn-5Zn alloy is suitable to be applied as material in a seawater environment [27].

Ti-13Cu-9Ni-5Mn-5Zn and Ti-20Cu-20Ni-20Mn-20Zn alloys exhibit different potentiodynamic polarization curves. The difference in the potentiodynamic polarization curve indicates a difference in corrosion mechanisms in two other alloy surfaces. Based on the potentiodynamic polarization curve, the tendency for pitting formation was observed in Ti13Cu9Ni5Mn5Zn alloy thermodynamically. However, it must be not the Ti13Cu9Ni5Mn5Zn alloy possesses lower current density compared to Ti20Cu20Ni20Mn20Zn alloy. Due to small current density, kinetically, the tendency of mass loss for pitting formation in Ti13Cu9Ni5Mn5Zn alloy was very slow. From the above results, it can be concluded that the Ti13Cu9Ni5Mn5Zn alloy is suitable to be applied as material in a seawater environment.

The EIS (electrochemical impedance spectroscopy) characterization was used to determine phenomena that occuring on the Ti-Cu-Ni-Mn-Zn alloy's surface [28]. The results of the EIS measurements of Ti-20Cu-20Ni-20Mn-

20Zn and Ti-13Cu-9Ni-5Mn-5Zn are presented in Nyquist plots, Bode Modulus plots, and Bode Phase plots in 3.5% NaCl solution, which can be seen in Fig. 7.

The Nyquist plot of both samples immersed in 3.5% NaCl solution showed a similar shape but different in diameter, indicating a difference in the corrosion rate. Nyquist plot of both Ti-20Cu-20Ni-20Mn-20Zn high entropy alloy and Ti-13Cu-9Ni-5Mn-5Zn beta titanium has one semi-circle. The loop is at high to low frequency. The equivalent circuit obtained from the curve fitting consists of the R_s (electrolyte resistance) in series with the CPE (constant phase element) and R_{ct} (charge transfer resistance), as shown in Fig. 8.

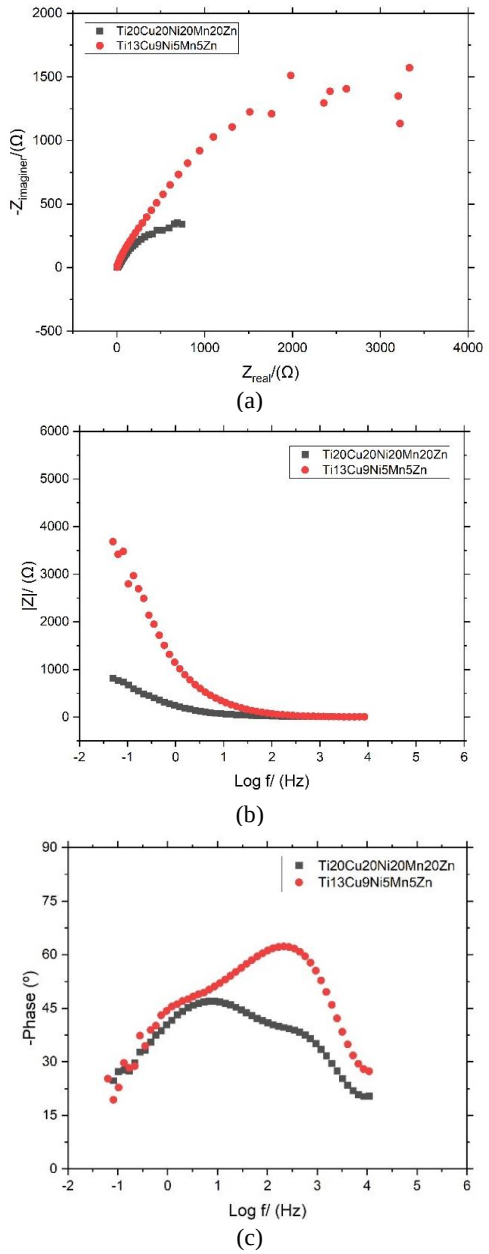

Figure 7. (a) Nyquist plot, (b) Bode modulus, and (c) Bode phase of each composition of Ti-Cu-Ni-Mn-Zn alloy after sintered at T= 880 °C for 3 hours

Figure 8 shows an equivalent circuit model representing the interface characteristics between the porous electrode and the electrolyte [29]. The circuits representing the pore's environment were added in parallel to the equivalent circuit model expressing the geometric electrode surfaces. This equivalent circuit consists of R_s representing the resistance in the electrolyte, R_{ct} representing the charge transfer resistance at the electrode interface, and CPE representing the electrical double layer capacitance at the electrode surface [29]. The interface layer of the Ti-20Cu-20Ni-20Mn-20Zn alloy has more pores than that of Ti-13Cu-9Ni-5Mn-5Zn alloy. This can be seen by a three parallel circuit added in Fig. 8(a), while Fig. 8(b) was only simulated with a two parallel circuit [29].

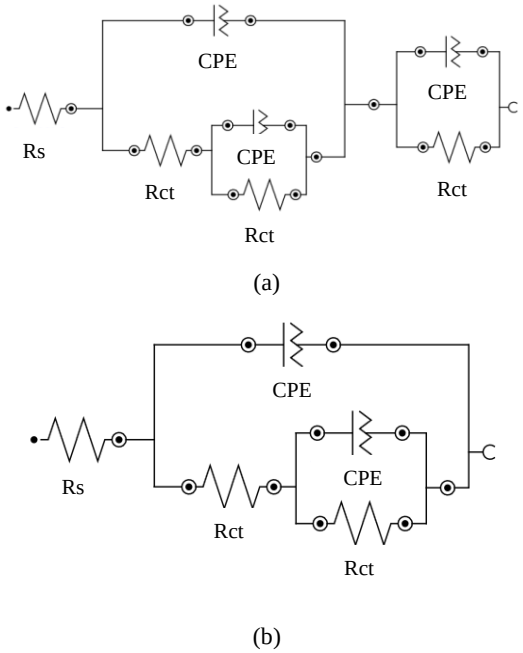

Figure 8. Equivalent circuit (a) Ti-20Cu-20Ni-20Mn-20Zn alloy and (b) Ti-13Cu-9Ni-5Mn-5Zn alloy, after sintered at T= 880 °C for 3 hours

The value of each electrical element is presented in Table 2. The R_p value represents the total resistance of R_s and R_{ct}. The higher R_p value of Ti-13Cu-9Ni-5Mn-5Zn β-Ti alloy indicates that the alloy is more resistant to corrosion in a 3.5% NaCl solution than Ti-20Cu-20Ni-20Mn-20Zn high entropy alloy.

Table 2. The results of fitting Ti-Cu-Ni-Mn-Zn alloy after sintered at T= 880 °C for 3 hours using EIS

Samples	R_p (Ω)	Q_n ($s_n\Omega^{-1}cm^{-2}$)	n
Ti-20Cu-20Ni-20Mn-20Zn	2,672.65	$1.390x10^{6}$	0.704
Ti-13Cu-9Ni-5Mn-5Zn	4,884.04	$0.278x10^{-3}$	1.429

Bode Modulus and Bode Phase plots exhibit a similar trend as the Nyquist plot, as seen in Figs.

7(c) and (d). A higher |Z| value was observed for Ti-13Cu-9Ni-5Mn-5Zn compared to Ti-20Cu-20Ni-20Mn-20Zn, indicating the material's higher corrosion resistance. The shift of the |Z| value in the medium frequency in titanium alloy might be related to the possible appearance of double capacitance at the interface of the material layers.

In the Bode Phase plots, the Ti-20Cu-20Ni-20Mn-20Zn high entropy alloy exhibit a lower phase angle compared than the Ti-13Cu-9Ni-5Mn-5Zn β-Ti alloy. The observed difference in phase angle indicates the difference in the corrosion rate of Ti-20Cu-20Ni-20Mn-20Zn and Ti-13Cu-9Ni-5Mn-5Zn alloy. The higher phase means that the alloy is more resistant to corrosion than the lower phase in the 3.5% NaCl solution.

4. CONCLUSION

The Ti-20Cu-20Ni-20Mn-20Zn and Ti-13Cu-9Ni-5Mn-5Zn alloys were successfully fabricated by the powder metallurgy method. Based on SEM-EDS mapping and XRD results, Ti-20Cu-20Ni-20Mn-20Zn and Ti-13Cu-9Ni-5Mn-5Zn alloys have a significant difference in phase concentration and phase distribution of intermetallic titanium and titanium elemental. The Ti-20Cu-20Ni-20Mn-20Zn alloy as a high entropy alloy has a lower hardness value of 190.658 HV and a higher corrosion rate of 1.7992 mm/year. The Ti-13Cu-9Ni-5Mn-5Zn alloy as a beta titanium alloy has a higher hardness value of 430.736 HV and a lower corrosion rate of 0.1212 mm/year. The results obtained indicate that Ti-13Cu-9Ni-5Mn-5Zn has better corrosion resistance in 3.5% NaCl solution and higher hardness than Ti-20Cu-20Ni-20Mn-20Zn for marine structure application.

ACKNOWLEDGMENT

This work supported Research Center for Metallurgy, The National Research and Innovation Agency (BRIN), Serpong.

REFERENCES

[1] A. S. Oryshchenko, I. V. Gorynin, V. P. Leonov, A. S. Kudryavtsev, V. I. Mikhailov, and E. V. Chudakov, "Marine titanium alloys: Present and future," *Inorg. Mater. Appl. Res.*, vol. 6, no. 6, pp. 571-579, 2015. Doi: 10.1134/S2075113315060106.

[2] F. Rokhmanto, "Pengaruh kandungan Mo dan Nb di dalam paduan logam implan (Ti-Al-Mo dan Ti-Al-Nb) terhadap pembentukan fasa beta," *Universitas Indonesia*, pp. 5-10, 2009.

[3] R. P. Kolli and A. Devaraj, "A review of metastable beta titanium alloys," *Metals (Basel).*, vol. 8, no. 7, pp. 1-41, 2018. Doi: 10.3390/met8070506.

[4] R. W. Schutz, "Environmental behavior of beta titanium alloys," *Jom*, vol. 46, no. 7, pp. 24-29, 1994. Doi: 10.1007/BF03220744.

[5] J. D. Cotton Robert, D. Briggs, Rodney R. Boyer, S. Tamirisakandala, P. Russo, N. Shchetnikov and John C. Fanning, "State of the art in beta titanium alloys for airframe applications," *Jom*, vol. 67, no. 6, pp. 1281–1303, 2015. Doi: 10.1007/s11837-015-1442-4.

[6] M. H. Tsai and J. W. Yeh, "High-entropy alloys: A critical review," *Mater. Res. Lett.*, vol. 2, no. 3, pp. 107–123, 2014. Doi: 10.1080/21663831.2014.912690.

[7] Y. F. Ye, Q. Wang, J. Lu, C. T. Liu, and Y. Yang, "High-entropy alloy: challenges and prospects," *Mater. Today*, vol. 19, no. 6, pp. 349–362, 2016. Doi: 10.1016/j.mattod.2015.11.026.

[8] E. P. George, D. Raabe, and R. O. Ritchie, "High-entropy alloys," *Nat. Rev. Mater.*, vol. 4, no. 8, pp. 515–534, 2019. Doi: 10.1038/s41578-019-0121-4.

[9] A. Sasongko, J. Setiawan, H. Hardiyanti, R. Suryadi, T. Yulianto and R. Langenati, "Perhitungan komposisi paduan high-entropy alloy AlCrMoNbZr untuk karakterisasi bahan struktur elemen bakar reaktor daya," *Hasil-Hasil Penelitian EBN Tahun 2020, BRIN Nuclear Energy Research Organization*, October, 2021. Doi: 10.13140/RG.2.2.21176.26885.

[10] J. Yeh, Y. Chen, S. Lin, and S. Chen, "High-entropy alloys – A new era of exploitation," *Materials Science Forum.*, vol. 560, pp. 1-9, 2007. Doi: 10.4028/www.scientific.net/MSF.560.1.

[11] D. B. Miracle and O. N. Senkov, "A critical review of high entropy alloys and related concepts," *Acta Mater.*, vol. 122, pp. 448–511, 2017. Doi: 10.1016/j.actamat.2016.08.081.

[12] Y. F. Ye, Q. Wang, J. Lu, C. T. Liu, and Y. Yang, "High-entropy alloy : challenges and prospects," *Materials Science*, vol. 00, no. 00, 2015. Doi: 10.1016/j.mattod.2015.11.026.

[13] N. Ma, S. Liu, W. Liu, L. Xie, D. Wei, L. Wang, L. Li, B. Zhao, Y. Wang , "Research progress of titanium-based high entropy alloy: Methods, properties,

and applications," *Front. Bioeng. Biotechnol*., vol. 8, no. November, pp. 1-18, 2020. Doi: 10.3389/fbioe.2020.603522.

[14] G. P. Vassilev, X. J. Liu, and K. Ishida, "Reaction kinetics and phase diagram studies in the Ti-Zn system," *J. Alloys Compd.*, vol. 375, no. 1-2, pp. 162-170, 2004. Doi: 10.1016/j.jallcom.2003.11.026.

[15] M. J. Mindel and S.R. Pollack, "The room temperature oxidation," *Acta Metall.*, vol. 17, p. 1441, 1969.

[16] S. Pan and W. Tsai, "Polarity reversal of titanium-coupled brass in 3.5 wt % NaCl solution Polarity reversal of titanium-coupled brass in 3.5 wt % NaCl solution Kadek Trisna Surya Hariyantha Szu-Jung Pan," *Conference: The International Corrosion Prevention Symposium for Research Scholars (CORSYM-2014) at Bombay, India*, 2014. Doi: 10.13140/2.1.2324.1609.

[17] M. J. Donachie, *Titanium - A Techincal Guide*, vol. 99, no. 5. 2000. [Online]. Available: http://www.intechopen.com/books/corrosion-resistance. Date of access: 20 February 2022.

[18] M. Kikuchi, Y. Takada, S. Kiyosue, M. Yoda, M. Woldu, Z. Cai, O. Okuno, T. Okabe, "Mechanical properties and microstructures of cast Ti-Cu alloys," *Dent. Mater.*, vol. 19, no. 3, pp. 174-181, 2003. Doi: 10.1016/S0109-5641(02)00027-1.

[19] T. Nakahata, "Industrial processing of titanium–nickel (Ti–Ni) shape memory alloys (SMAs) to achieve key properties", *Woodhead Publishing Limited*, pp. 53-62, 2011. Doi: 10.1533/9780857092625.1.53.

[20] J. L. Murray, "The Mn-Ti (Manganese-Titanium) system," *Bulletin of Alloy Phase Diagrams*, vol. 2, no. 3, pp. 334-343, 1981.

[21] Y. Alshammari, F. Yang, and L. Bolzoni, "Mechanical properties and microstructure of Ti-Mn alloys produced via powder metallurgy for biomedical applications," *J. Mech. Behav. Biomed. Mater.*, vol. 91, pp. 391-397, 2019. Doi: 10.1016/j.jmbbm.2018.12.005.

[22] H. Okamoto, "Ti-Zn (Titanium-Zinc)," *J. Phase Equilibria Diffus.*, vol. 29, no. 2, pp. 211-212, 2008. Doi: 10.1007/s11669-008-9271-6.

[23] Y. Yuan, Y. Wu, Z. Yang, X. Liang, Z. Lei, H. Huang, H. Wang, X. Liu, K. An, W. Wu and Z. Lu, "Formation, structure and properties of biocompatible TiZrHfNbTa high-entropy alloys," *Mater. Res. Lett.*, vol. 7, no. 6, pp. 225-231, 2019. Doi: 10.1080/21663831.2019.1584592.

[24] D. Wu, W. lin Wang, L. gang Zhang, Z. yu Wang, K. chao Zhou, and L. bin Liu, "New high-strength Ti–Al–V–Mo alloy: from high-throughput composition design to mechanical properties," *Int. J. Miner. Metall. Mater.*, vol. 26, no. 9, pp. 1151-1165, 2019. Doi: 10.1007/s12613-019-1854-1.

[25] A. Abada, S. Bergheul, and A. Younes, "Mechanical and structural behaviour of TiAlV nanocrystalline elaborated by mechanical milling technique," *Micro Nano Lett.*, vol. 15, no. 14, pp. 1023-1027, 2020. Doi: 10.1049/mnl.2020.0336.

[26] D. Prando, A. Brenna, M. V. Diamanti, S. Beretta, F. Bolzoni, M. Ormellese and M. Pedeferri, "Corrosion of titanium: Part 2: Effects of surface treatments," *J. Appl. Biomater. Funct. Mater.*, vol. 16, no. 1, pp. 3-13, 2018. Doi: 10.5301/jabfm.5000396.

[27] Z. Yan, X. Yuan, Z. Tan, M. Tang, and Z. Feng, "Effect of in situ ion nitride treatment on the corrosion behavior of titanium," *Corrosion Science*, vol. 13, pp. 353-361, 2018. Doi: 10.20964/2018.01.23.

[28] S. Feliu, "Electrochemical impedance spectroscopy for the measurement of the corrosion rate of magnesium alloys: Brief review and challenges," *Metals (Basel).*, vol. 10, no. 6, pp. 1-23, 2020. Doi: 10.3390/met10060775.

[29] S. Nomura, H. Tashiro, Y. Terasawa, Y. Nakano, M. Haruta, K. Sasagawa, H. Takehara and J. Ohta, "Randles circuit model for characterizing a porous stimulating electrode of the retinal prosthesis," *Electron. Commun. Japan*, vol. 104, no. 3, pp. 1-9, 2021. Doi: 10.1002/ecj.12324.

Metalurgi (2022) 2: 57 - 64

METALURGI
Majalah Ilmu dan Teknologi
p-ISSN 0126-3188 | e-ISSN 2443-3926
ejurnalmaterialmetalurgi.lipi.go.id

EFFECT OF HEATING TEMPERATURE AND DIE INSERT DRAFT ANGLE ON THE FLOWABILITY OF HOT FORGED SCM435 STEEL

Nofrijon Sofyan[a,*], Maulana Heruwiyono[a], Akhmad Herman Yuwono[a], Donanta Dhaneswara[a]
[a]Departments of Metallurgical and Materials Engineering, Universitas Indonesia
Kampus UI Depok, Jawa Barat, Indonesia, 16425
*E-mail: nofrijon.sofyan@ui.ac.id

Received: 16-03-2022, Revised: 18-07-2022, Accepted: 04-10-2022

Abstract

The flowability problem of a closed forging process in the heavy equipment industry is still widely found. This problem may affect the quality of the product. To solve this problem, the effect of heating temperature and die insert draft angle on the characteristic of hot forged SCM435 steel used for undercarriage track roller has been examined. In the experiment, the workpieces were hot forged at a heating temperatures of 1150 °C, 1200 °C, 1250 °C, and die to insert draft angles of 3°, 5°, and 7° to form undercarriage track roller products. The mechanical properties of the specimens taken from the workpieces were characterized through hardness and dimensional changes, whereas the microstructure was characterized using an optical microscope. The results showed that increasing the heating temperature and die insert draft angle resulted in good flowability. The best product with the specified diameter of 191.2 mm and height of 53.6 mm was obtained from the heating temperature of 1250 °C at the die insert draft angle of 7°. This characteristic agreed with the specified forging design for the undercarriage track roller.

Keywords: *Flowability, hot forging, track roller, undercarriage, underfilling*

1. INTRODUCTION

The growth of heavy equipment industries continues to experience ups and downs in line with its use [1]. To keep this heavy equipment industry running, innovation is needed in the production line by continuously improving in the manufacturing process, both in assembly and component processes [2]. Heavy equipment components are generally made through metal forming technology [3]. One of the metal forming processes for this purpose is the hot forging process. Compare to other processes, the advantage of this hot forging is the strength and toughness of the product that can be controlled closely [4]. In this instance, hot forging can be applied to heavy equipment parts that require high strength and toughness.

One of the parts in the heavy equipment is a track roller contained in the undercarriage that serves as a unit weight divider to the track and a track link driver [5]. Track roller is one of the undercarriage components made with the hot forging process, especially through a closed die hot forging [6]. In the process, however, there is still a problem with an underfilling that results in the defective product. The effort is necessary to solve this problem, primarily in avoiding any losses arising from the defective product.

Underfilling is a condition in which the material can not to fill the desired die during the hot forging process. This condition is affected by many factors, such as improper die forging design, incorrect forging methods, less material, and insufficient material heating temperature [4]. In this instance, design is one factor that affects the material's flowability during hot forging. Improving the design, it will also enhance the flow of the material to reduce defective products. In their research, Mane and Patil [7] have made corrections to the die design in the axle beam. This improved design, it has been proven to improve product productivity [8]. Furthermore, the insufficient heating temperature during the hot forging may cause less flow of the material, and thus, the material cannot fill the die properly [9]-[10]. The worst condition could occur because hot forging at this insufficient

DOI: 10.14203/metalurgi.v37i2.635

Metalurgi is Sinta 2 Journal (https://sinta.ristekbrin.go.id/journals/detail?id=3708) accredited by Ministry of Research & Technology, Republic Indonesia

temperature may result in crack initiation and thus, the defective product.

According to the JIS (japanese industrial standards) [11], this steel is considered high-strength steel with wide range of applications such as automobile clutches, shafts, gears, undercarriage, and flywheels parts [12]-[13]. However, this steel has a drawback in which during the hot forging process, it cannot fill the desired die and thus results in the defect after the process due to an underfilling condition [13].

One of the ways expected to overcome the underfilling problem found in SCM435 steel is by optimizing the heating temperature and die insert draft angle design. In this work, the material was hot forged at heating temperature variations of 1150, 1200, 1250 °C and die to insert draft angles of 3°, 5°, and 7° to form undercarriage track roller products. The results are presented and discussed in detail.

2. MATERIALS AND METHODS

The material was cylindrical bar steel with a dimension of 170 mm in diameter and 400 mm in length provided by PT. Komatsu Undercarriage Indonesia.

Tabel 1. Composition (wt.%) of the as-received material

C	Si	Mn	P	S	Ni
0.364	0.318	1.346	0.008	0.012	0.0
Cr	Mo	Cu	Al	B	Fe
0.517	0.116	0.009	0.033	0.002	Rem

The composition of the as-received material was tested using optical spectrometry, with the result given in Table 1.

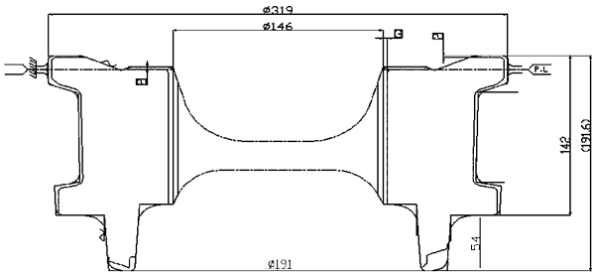

Figure 1. Track roller design. The unit is in millimeter (mm)

The product was designed in the form of a double flange track roller used as an undercarriage component, as shown in Fig. 1. To realize the product, the die was also designed accordingly, which consists of several parts arranged into a single die forging. The part that forms the inside and the end of the track roller is called inner die parts, which are adjustable and made of SKD61 tool steel.

,

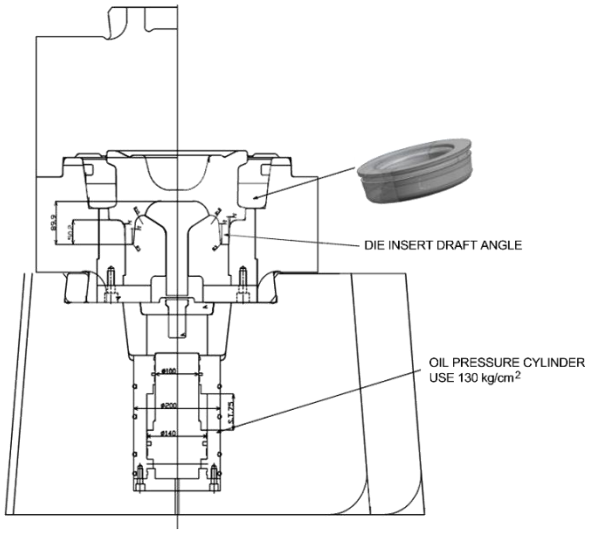

Figure 2. Die structure of the double flange track roller component

In this work, the inner die parts were adjusted to have a variation die insert draft angles of 3, 5 and 7 degrees. The structure and the inner die parts of the double flange track roller components used in this work are given in Figure 2 and Figure 3, respectively.

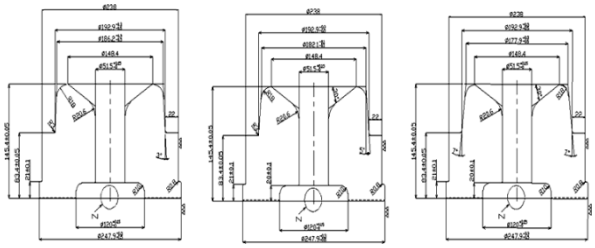

(a) (b) (c)

Figure 3. Die insert draft angle variations (a) 3, (b) 5, and (c) 7 degrees

The work was carried out at PT. Komatsu Undercarriage Indonesia. The experiment began by first installing the die forging on a forging machine and a trimmer jig on a trimming machine. This machine was used to cut the existing flash of the forging products after the process.

After the installation process was completed, the die was preheated to a temperature of 150 °C and left until homogeneous heat was obtained and the piecework materials were ready. The workpieces were then heated at temperature variations of 1150, 1200, and 1250 °C using an induction furnace (Neturen, 1000 kW and 6.6 kHz), which has a very high uniform heating distribution with the help of a conveyor passing through the coil in the induction furnace with a speed of 2.7 mm/s toward the forging machine. Temperature control for each step was carried out using a temperature measuring apparatus before and after the hot forging process. After the hot

forging, each workpiece was trimmed, air cooled, and ready for the next treatment. The sequence of this experimental procedure is given in Fig. 4.

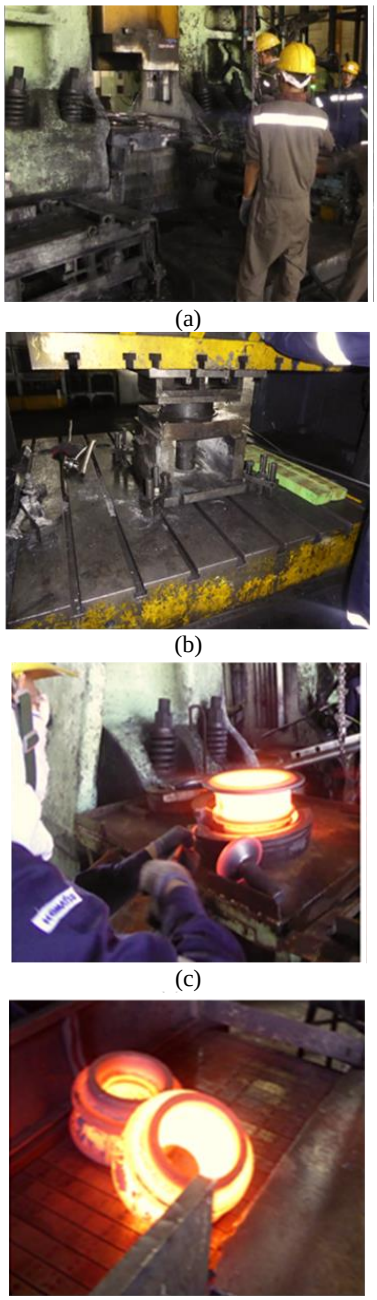

Figure 4. Experimental procedure: (a) die installation of the forging equipment, (b) trimmer jig installation on the trimming machine, (c) the undercarriage product, (d) and the undercarriage after trimming

After the hot forging process, the workpieces were tested for their dimension, hardness, and microstructure. The specimens for the characterization were taken from the bottom part of the workpiece after cross-sectioning it as schematically given in Fig. 5.

The dimension was measured within the original design's closest range, which was 191 mm and 54 mm for diameter and height, respectively. For the mechanical properties, Rockwell hardness testing was performed in according to ASTM-E18-16.

For the microstructural analysis, the specimen was first sand papered up to 1200 grits, then polishing it using diamond paste. After cleaning it with alcohol, the specimen was etched by immersing it in 8 % Nital solution (8 % nitric acid in alcohol) for 10 seconds.

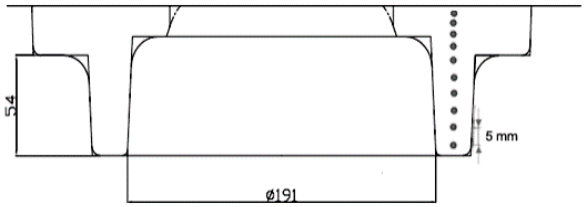

Figure 5. Cross section of the workpiece where the specimens were taken for the characterization purposes

Using an optical microscope (Keyence VHX-5000), the specimen was ready for microstructural characterization. All characterizations was performed at an ambient condition.

3. RESULT AND DISCUSSION

During hot forging, a material undergoes plastic deformation following the shape of the die. To obtain the characteristic of the material's flowability during the hot forging, the dimension of the product was measured in terms of the diameter and height of the track roller product given in the design. In this instance, the flowability of the material is limited to the capability of the material to fill the die during the hot forging process. The results of the dimensional change measurement are given in Fig. 6.

Dimensional change measurement showed that the closest approximated dimensions according to the original product design were the one with a die insert draft angle of 7° and heating temperature of 1250 °C, i.e., 191.2 mm and 53.6 mm for diameter and height, respectively. Other workpieces heated at other heating temperatures using different die insert draft angles experienced off-dimensions in which the diameter and or height of the workpiece could not meet the design specification. At a heating temperature of 1150 °C and a draft angle of 3°, for example, the resulting product has 193.0 mm and 52.1 mm for diameter and height, respectively. It is suspected that the situation could occur because the forging temperature was still relatively low for the material to deform. Moreover, the forging temperature could also somehow decrease during the forging process, which might cause material's

flowability to decrease as the temperature decreases.

The die inserts draft angles obviously affected the flowability of the material and, thus, the material's ability to fill the die. As can be seen from the graph, at the same temperature, the 7° draft angle results in more height as compared to that of 5° and 3° draft angles. The draft angle of 7° and heating temperature of 1250 °C results in the highest height at 53.6 mm. This is probably because a large draft angle makes the material easy to flow through the die.

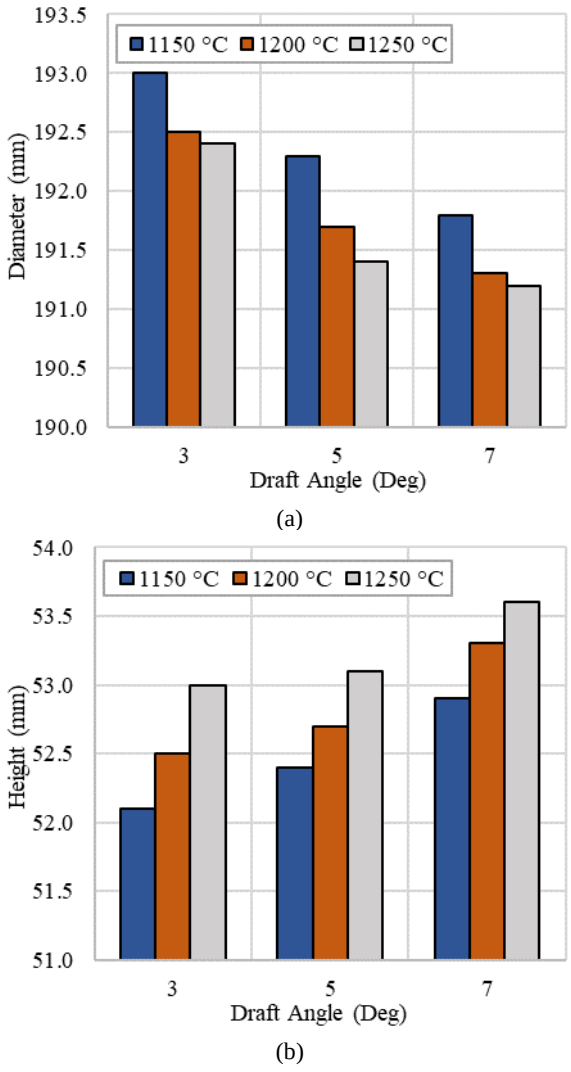

Figure 6. The effect of temperature variations at different die insert draft angles on the dimensional change of the undercarriage track roller products after hot forging (a) height and (b) diameter

During the forging process, plastic deformation may occur in longitudinal and cross sectional directions; however, the degree of change might be differ depending on the flowability and the die design. As seen in Fig. 6, the average value of the diameter is greater than the average height value. In this instance, the deformation is more dominant in the cross-sectional direction, and thus, the change in diameter is larger than that of the longitudinal direction. This corresponds to the state of the forging process, i.e., compression, in which the deformation tends to move freely towards the frictionless (free) direction [14]. From the picture in Fig. 6, it can also be seen that with the increase in temperature and the die insert draft angle, the deformation increases, which means that the material can fill the die well. This is because with the increase of temperature, the more the flow and thus the easier the material to fill the die will be, even at a relatively small load [15].

The hardness testing would be helpful to examine the hardness distribution of the forging products in line with the changes in the forging temperature and die insert draft angle. Hardness distribution from the edge inward at temperature variations of 1150, 1200, and 1250 °C and various die insert draft angles is given in Figs. 7(a), 7(b), and 7(c), respectively. In contrast, the average hardness is given in Fig. 8.

The average hardness of the material after hot forging seems to be affected by the temperature [16] and the draft angle, in, which the higher the temperature and the draft angle, there is a tendency that the hardness also increases. The range of the hardness is about 28-29 HRC, which is statistically insignificant. However, since the hardness of the material before hot forging is about 18.7 HRC, this process profoundly proves that there is an increase of about 54% in hardness after the hot forging. It is expected that the higher the heating temperature, the higher the initial temperature for the air-quenched process. With the carbon content of 0.364 wt.%, as seen in Table 1, it would be understandable that the hardness will also increase with the increase of heating temperature.

At the same temperature, the hardness distribution of the workpiece tends to increase from the edge inward to 1200 °C. This corresponds to the deformation of the material at high temperatures. After experiencing high deformation during the forging, because of high temperature, the recrystallization and, thus, the grain growth at the edge take place faster in comparison to the area inside farther from the edge and therefore make the hardness increase inward. At 1250 °C, even though the difference is insignificant, as mentioned previously, the distribution is almost constant, and the average hardness tends to be relatively lower than that of two other temperatures. This constant hardness distribution is expected due to a more homogeneous temperature distribution.

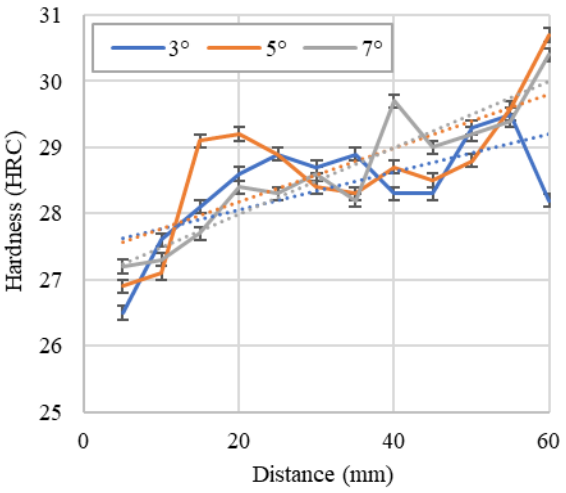

(a)

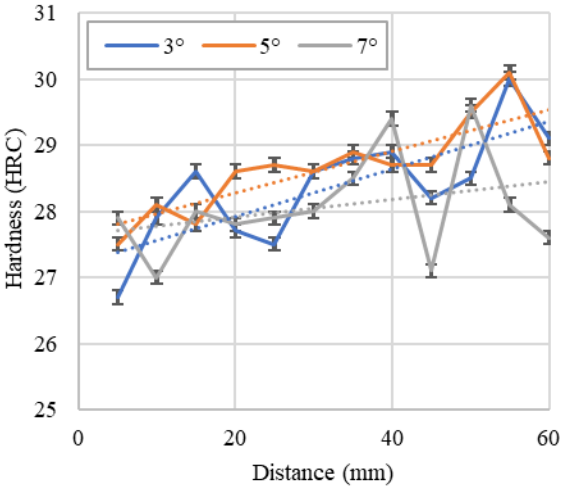

(b)

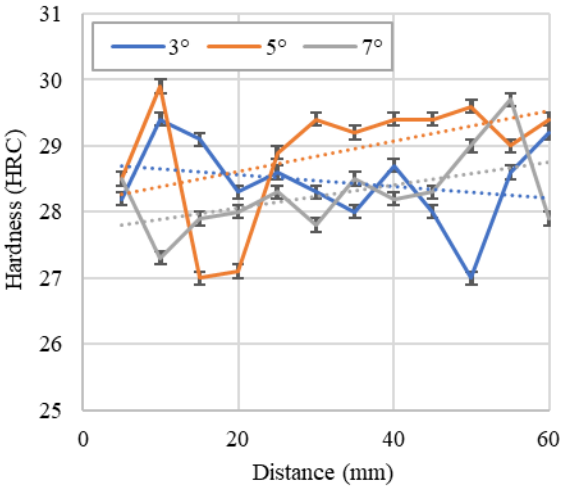

(c)

Figure 7. Hardness distribution from the edge inward at temperature variations (°C); (a) 1150, (b) 1200, (c) 1250 and various die insert draft angles. Error bars are given on each line graph

At this high temperature, it would be much easier for recrystallization and grain growth to take place, and thus, compared to two other temperatures, decrease the average hardness [17].

A microstructural investigation was performed using an optical microscope on the specimen taken from the bottom of the product. The observation was performed at a magnification of 500 x, and the results are given in Fig. 9.

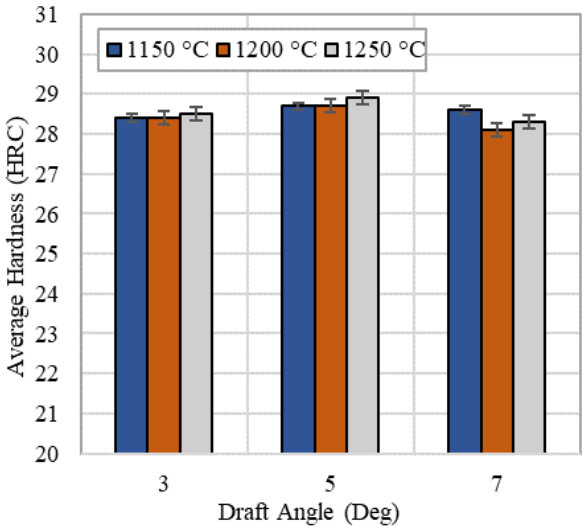

Figure 8. Average hardness from the edge inward at various die insert draft angles and temperature variations. Error bar is given on each bar graph

As can be seen in Fig. 9, the microstructure shows that the edge of the product has a non-homogeneous grain size in which large and small grain sizes are mixed due to a mixture of ferrite and pearlite grains from austenite transformation [18]-[19]. Examination of the microstructures revealed that different heating temperatures result in different phase structures, as can seen in Fig. 9. This microstructure examination supports hardness distribution in which due to more as has been explained previously.

After the hot forging process, some forged products experienced oxidation and decarburization at the tip of surfaces resulting in coarse microstructure [20]. With the increasing temperature, the workpiece becomes susceptible to scale formation and decarburization.

Steel materials with heating temperatures higher than 1150 °C have high sensitivity to decarburization. In this instance, good control is required for the forging process [21]. The depth of the decarburization may affect the material's properties leading to fatigue failure during service if it is not properly handled.

The formation of this scale needs to be considered to determine the appropriate tolerance so as not to reduce the dimensions of ready-made products. This would be primarily true because the uneven surface may lead to an undesired heavy machining process.

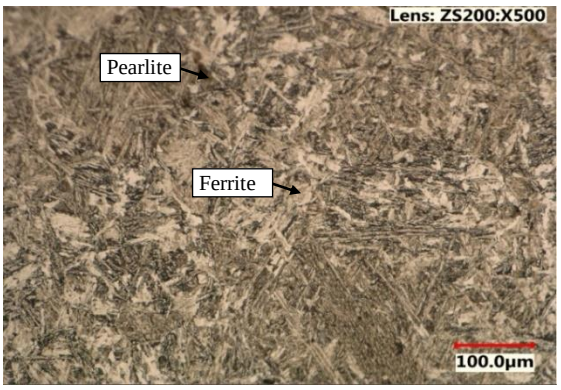

(a)

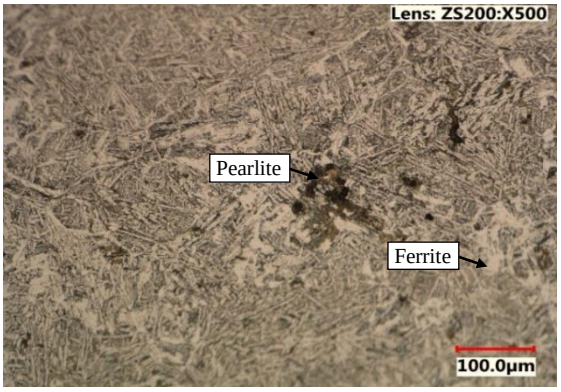

(b)

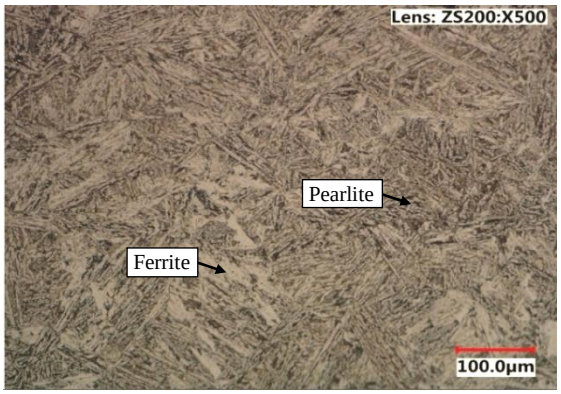

(c)

Figure 9. Microstructure of the workpieces heated (°C) at (a) 1150 with die insert angle of 3°, (b) 1200 with die insert angle of 5°, and (c) 1250 with die insert angle of 7°. Bar scale is 100 μm

4. CONCLUSION

Plastic deformation of the largest after-wrought product occurs at a temperature of 1250 °C and a die draft angle of 7° with a diameter of 191.2 mm and height of 53.6 mm, very close to the desired dimensions for diameter and for height. The distribution of hardness is affected by the temperature and the draft angle in which the higher the temperature and the draft angle, there is tendency for the hardness also increases after the hot forging. The heating temperatures of 1150, 1200, and 1250 °C do not significantly affect the hardness statistically. However, the hot forging process does increase the hardness by about 54% as compared to the original material. The characteristics of the obtained hot-forged material agreed with the specified forging design for the undercarriage track roller. Thus could be further tested for large-scale production.

ACKNOWLEDGMENT

The authors would like to thank PT. Komatsu Undercarriage Indonesia for providing the sample and equipment during the research.

REFERENCES

[1] M. Gobetto, *Operations Management in Automotive Industries*. Dordrecht: Springer Netherlands, pp. 1-43, 2014. Doi: 10.1007/978-94-007-7593-0.

[2] Siemens, "Heavy equipment & off highway vehicles," 2022. https://www.plm.automation.siemens.com/global/en/industries/heavy-equipment/ (accessed Jun. 05, 2022).

[3] M. Kleiner, M. Geiger, and A. Klaus, "Manufacturing of lightweight components by metal forming," *CIRP Annals*, vol. 52, no. 2, pp. 521–542, 2003. Doi: https://doi.org/10.1016/S0007-8506(07)60202-9.

[4] S. Kalpakjian, S. R. Schmid, and H. Musa, *Manufacturing Engineering and Technology*. 6 Ed. Singapore: Prentice Hall, pp. 335-357, 2009.

[5] H. L. Nichols Jr. and D. A. Day, *Moving the Earth: The Workbook of Excavation*, 6th ed. New York: McGraw-Hill Education, pp. 15.1-15.9, 2010.

[6] O. C. Duffy, S. A. Heard, and G. Wright, *Fundamentals of Mobile Heavy Equipment*. Burlington, MA: Jones & Bartlett Learning, LLC, pp. 991-1025, 2019.

[7] A. H. Mane, "Design and analysis of secondary up setter die to correct under filling problem for forged front axle beam," *International Engineering Research Journal*, vol. special issue, no. 2, pp. 4590-4593, 2015.

[8] M. G. Rathi and N. A. Jakhade, "An overview of forging process with their defects," *International Journal of Scientific and Research Publications*, vol. 4, no. 6, pp. 1-6, 2014.

[9] S.-W. Lee, J.-W. Jo, M.-S. Joun, and J.-M. Lee, "Effect of friction conditions on material flow in FE analysis of Al piston forging process," *International Journal of Precision Engineering and Manufacturing*, vol. 20, no. 10, pp. 1643-1652, 2019. Doi:

10.1007/s12541-019-00189-8.

[10] M. Hawryluk, D. Dobras, M. Kaszuba, P. Widomski, and J. Ziemba, "Influence of the different variants of the surface treatment on the durability of forging dies made of Unimax steel," *The International Journal of Advanced Manufacturing Technology*, vol. 107, no. 11, pp. 4725-4739, 2020. Doi: 10.1007/s00170-020-05357-z.

[11] C.-Y. Chen, F.-Y. Hung, T.-S. Lui, and L.-H. Chen, "Microstructures and mechanical properties of austempering Cr-Mo (SCM 435) alloy steel," *Materials Transactions*, vol. 54, no. 1, pp. 56-60, 2013. Doi: 10.2320/matertrans.M2012317.

[12] C. Ji, L. Wang, and M. Zhu, "Effect of subcritical annealing temperature on microstructure and mechanical properties of SCM435 steel," *Journal of Iron and Steel Research, International*, vol. 22, no. 11, pp. 1031-1036, 2015. Doi: 10.1016/S1006706X(15)30108-4.

[13] K. Tanaka, D. Shimonishi, D. Nakagawa, M. Ijiri, and T. Yoshimura, "Stress relaxation behavior of cavitation-processed Cr–Mo steel and Ni–Cr–Mo steel," *Applied Sciences*, vol. 9, no. 2, p. 299, 2019. Doi: 10.3390/app9020299.

[14] N. C. Cho, S. H. Lee, S. S. Hong, and J. S. Lee, "Experimental verification of preform design for axisymmetric heavy forging on a model hammer," *Journal of Materials Processing Technology*, vol. 47, no. 1-2, pp. 103-110, 1994. Doi: 10.1016/09240136(94)90088-4

[15] G.E. Dieter, Introduction to Workability, in J. R. Davis and S. L. Semiatin, *ASM Metals Handbook, Vol 14: Forming and Forging*, 9th ed., vol. 14. Ohio: ASM International, pp. 363-372, 1989.

[16] I. P. Nanda, Z. Ali, N. F. B. W. Anuar, M. H. Idris, and A. Arafat, "Effect of forging temperature on biodegradable Mg-0.7%Ca alloy properties for Implant application," *IOP Conference Series: Materials Science and Engineering*, vol. 1062, no. 1, p. 012047, 2021. Doi: 10.1088/1757-899X/1062/1/012047.

[17] D. Li, L. Chai, Z. Chen, T. Jin, G. Shi, Y. Jin, and Z. Feng, "Effects of forging temperature on microstructure and mechanical properties of 650 °C high temperature titanium alloy," in *High Performance Structural Materials*, Singapore: Springer Singapore, pp. 477-483, 2018. Doi: 10.1007/978-981-13-0104-9_51.

[18] M. Müller, D. Britz, L. Ulrich, T. Staudt, and F. Mücklich, "Classification of bainitic structures using textural parameters and machine learning techniques," *Metals (Basel)*, vol. 10, no. 5, p. 630, 2020. Doi: 10.3390/met10050630.

[19] H. Kim, J. Inoue, and T. Kasuya, "Unsupervised microstructure segmentation by mimicking metallurgists' approach to pattern recognition," *Scientific Reports*, vol. 10, no. 1, p. 17835, 2020. Doi: 10.1038/s41598-020-74935-8.

[20] M. Irani and A. K. Taheri, "Effect of forging temperature on homogeneity of microstructure and hardness of precision forged steel spur gear," *Materials Chemistry and Physics*, vol. 112, no. 3, pp. 1099-1105, 2008. Doi: 10.1016/j.matchemphys.2008.07.044.

[21] C. Zhang, li-yao Xie, G. Liu, lie Chen, Y. Liu, and J. Li, "Surface decarburization behavior and its adverse effects of air-cooled forging steel C70S6 for fracture splitting connecting rod," *Metals and Materials International*, vol. 22, no. 5, pp. 836-841, 2016. Doi: 10.1007/s12540-016-5657-x.

Metalurgi (2022) 2: 65 - 72

METALURGI
Majalah Ilmu dan Teknologi
p-ISSN 0126-3188 | e-ISSN 2443-3926
ejurnalmaterialmetalurgi.lipi.go.id

EFFECT OF Nd_2O_3 AND Fe_2O_3 ADDITION ON GADOLINIA DOPED CERIA (GDC) SOLID ELECTROLYTE SYSTEM FOR INTERMEDIATE TEMPERATURE-SOLID OXIDE FUEL CELL (IT-SOFC) APPLICATIONS

Muhammad Faisal Akbar[a,*], Bonita Dilasari[a], Syoni Soepriyanto[a], Dadan Suhendar[a]
[a]Bandung Institute of Technology
Ganesha No. 10, Bandung, Jawa barat, Indonesia 40132
*E-mail: mfaisalakbar4529@gmail.com

Received: 21-04-2022, Revised: 05-09-2022, Accepted: 04-10-2022

Abstract

GDC (gadolinia doped ceria) is a solid electrolyte contender for intermediate-temperature SOFCs (solid oxide fuel cell). However, more development of this solid electrolyte is required to improve its ionic conductivity. We will investigate the effect of Nd_2O_3 and Fe_2O_3 addition on GDC solid electrolytes to boost ionic conductivity. Solid electrolytes of the composition $Ce_{0.9}Gd_{0.2}M_xO_{1.9}$ (M = Nd, Fe) (x = 0% ; 2.5% ; 5%, and 7.5%) were synthesized using mixed oxide method and formed into pellets with a diameter of 1 cm. The pellets were sintered at 1200 ℃ and 1400 ℃ for 4 hours in an Argon environment then the EIS (electrochemical impedance spectroscopy) test was performed at 450-650°C. The results showed that the Nd_2O_3 and Fe_2O_3 added were totally dissolved in the ceria structure and produced single-phase cubic fluorite CeO_2. GDC solid electrolyte with Fe_2O_3 addition produces higher densification than Nd_2O_3 addition, where the value reaches 75% in the GDC sintered at 1400 ℃. However, the addition of Nd_2O_3 further increased the value of ionic conductivity and decreased the activation energy of the GDC solid electrolyte compared to the addition of Fe_2O_3. The highest ionic conductivity and the lowest activation energy were obtained in the GDC with 2.5% Nd_2O_3 in 650 ℃ operating temperature, with the values achieved were 1.2 mS/cm and 0.41 eV, respectively. Therefore, it can be concluded that Nd_2O_3 addition is more effective to improve the performance of solid electrolyte GDC.

Keywords: *SOFC (solid-oxide fuel cell), solid electrolyte, GDC (gadolinia doped ceria), ionic conductivity*

1. INTRODUCTION

SOFC (solid oxide fuel cell) is a type of fuel cell or electrochemical device that can transform chemical energy from a fuel into electrical energy and heat without using a combustion stage [1]. SOFCs have several advantages over other fuel cells, including higher electrode corrosion resistance, higher fuel flexibility, and high power efficiency (40-60%) [2]. However, SOFC still has several operational issues, particularly the high operating temperature (1000 °C). The high operating temperature causes many problems in its operation, such as rapid material degradation, making it less economical [3]. Therefore, the current research focuses on lowering the operating temperature of SOFCs while maintaining good performance quality.

One effort that may be made is choosing the appropriate solid electrolyte material. The solid electrolyte must have a high ionic conductivity to be used at an intermediate temperature (400-700 °C) SOFC or IT-SOFC [4]. YSZ (Yttria stabilized zirconia) is a solid electrolyte commonly utilized in commercial SOFCs that operate at 1000 °C [5]. Nevertheless, the ionic conductivity value of YSZ diminishes in the medium operating temperature range, preventing it from being employed on IT-SOFC [6]. GDC (gadolinia doped ceria) has the potential to be employed as a solid electrolyte in IT-SOFC because it has sufficient ionic conductivity, low activation energy, and higher catalytic activity at medium temperatures [7]. However, further

DOI : 10.14203/metalurgi.v37i2.614

Metalurgi is Sinta 2 Journal (https://sinta.ristekbrin.go.id/journals/detail?id=3708) accredited by Ministry of Research & Technology, Republic Indonesia

development of this solid electrolyte is required to improve its ionic conductivity.

According to Herle et. al., [8], the addition of double doping (co-doping) with two cations can enhance the ionic conductivity of a ceria-based solid electrolyte compared to single doping. Co-doping to the GDC solid electrolyte can enhance ionic conductivity and stability by preventing partial reduction of the GDC solid electrolyte [9]. According to Andersson et. al., [10], the optimal dopant for a ceria-based solid electrolyte is Promethium (Pm) (atomic number 61). Based on modeling with vienna ab initio, the addition of Pm to the ceria matrix will result in the lowest vacancy formation energy and binding energy between defects compared to other elements. Consequently, the activation energy value of the ceria-based solid electrolyte system will be lower. On the other hand, Pm is a synthetic element that does not exist in nature. As a result, the most likely approach is to use elements with atomic numbers near to 61, or more commonly, rare earth metal oxides. This is because the binding energy is a function of the atomic number. Hence the atomic number of the dopant element should be as close to Pm as possible. Neodymium (atomic number 60) is an element that can be used for co-doping of ceria-based solid electrolytes because it has an atomic number close to Pm. This co-doping aims to enhance the vacancy concentration in cubic fluorite ceria, hence increasing the ionic conductivity[11]. Apart from doping, various research has investigated the addition of a sintering aid to the GDC solid electrolyte to improve the densification [12]. With increasing densification, it is expected that the ionic conductivity will also increase. One type of sintering aid that is widely used is transition metal oxides such as Fe_2O_3 [13].

In this study, the effect of the addition of rare earth metal oxides (Nd_2O_3) and transition metal oxides (Fe_2O_3) on the physical and electrical characteristics of GDC solid electrolyte will be compared to determine the more effective material to improve the performance of solid electrolytes.

2. MATERIALS AND METHODS

Solid electrolytes with compositions $Ce_{0.9}Gd_{0.2}Nd_xO_{1.9}$ and $Ce_{0.9}Gd_{0.2}Fe_xO_{1.9}$ (x = 0, 2.5%, 5% and 7.5%) were synthesized using CeO_2, Gd_2O_3, Nd_2O_3, and Fe_2O_3 precursor with high purity (99,9%). All powders were mixed in 96% ethanol media. The ethanol-powder mixture was heated to 70 °C on a hotplate and stirred using a magnetic stirrer until all of the ethanol had evaporated and there was a powder deposit at the bottom of the beaker. Then the powder was dried in an oven at 150 °C for 1 hour. The powder was then ground using a mortar with a PVA binder of 3 wt.% and 70% alcohol. After grinding, the powder was pressed into a 1 cm thick green pellet using a hydraulic compacting machine with a pressure of 40 kN. The pellets were then sintered in a tube furnace (Thermolyne) at two temperature variations of 1200 °C and 1400 °C for 4 hours in an Argon environment. Then several tests were carried out on the sintered pellets, including EIS (electrochemical impedance spectroscopy), XRD (x-ray diffraction), and SEM (scanning electron microscope) tests.

EIS test was carried out using a potentiostat (Corrtest) with silver paste as the standard electrode and current collector at a temperature of 450-650 °C with a frequency range of 100 kHz-0.1 Hz using an AC signal of 20 mV. The Nyquist and Bode curves obtained from the EIS test are then fitted with an equivalent circuit model using ZView software to bring the grain (R_g) and grain boundaries (R_{gb}) resistance of solid electrolytes. The total resistance (R_{total}) value can be calculated by Equation (1), and then can be used to determine the ionic conductivity and activation energy value.

$$R_{total} = R_g + R_{gb} \qquad (1)$$

3. RESULT AND DISCUSSION

3.1 Phase Analysis

Figure 1 shows the diffraction pattern of the solid electrolyte of GDC (gadolinia doped ceria) with the addition of Nd_2O_3 (Nd-GDC) and Fe_2O_3 (Fe-GDC). The diffraction pattern of the three GDCs has the same pattern where the peaks are identified as planes (111), (200), (220), etc.

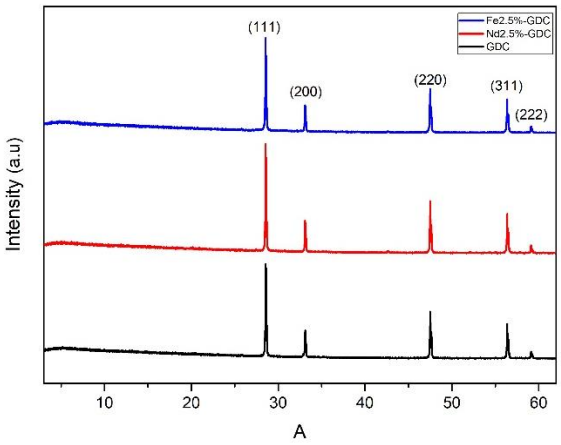

Figure 1. X-ray diffraction pattern of GDC, Nd2.5%-GDC, and Fe2.5%-GDC sintered at 1200 °C

These peaks indicate that the structure generated in the three GDCs is single-phase cubic

fluorite CeO_2 [14] (JCPDS no. 34-394), and Gd_2O_3, Nd_2O_3, and Fe_2O_3 doping have been entirely dissolved into the ceria structure (CeO_2). Adding Gd^{3+}, Nd^{3+}, and Fe^{3+} to the ceria matrix results in subtituting of Ce^{4+} ions, forming a solid solution [15]. This ion substitution changes the lattice parameter of cubic fluorite ceria due to the difference in ionic radii between Ce^{4+} (0.097 nm) as the host atom with Gd^{3+} (0.105 nm), Nd^{3+} (0.110 nm), and Fe^{3+}(0.069 nm) as doping atom [16].

3.2 Densification and Microstructure Analysis

Densification is a powder shrinkage process that occurs during the sintering process. Densification is observed with % relative density or by comparing the density of the sintered product with its theoretical density.

Figure 2 shows the relative density of solid electrolyte GDCs sintered at 1200 °C and 1400 °C. Based on the graph, the densification increased up to concentration of 2.5%, and then decreased with further increases in the co-doping concentration. Densification increases owing to mass transfer during the sintering process, which can remove pores in the solid electrolyte system. Furthermore, the rise in densification was driven by changes in the ceria lattice properties due to dopant addition. However, densification decreases as the concentration exceed 2.5%. The decrease in densification was caused by an excessive co-doping concentration, which causes more Nd^{3+} or Fe^{3+} atoms to substitute Ce^{4+} atoms, resulting in excessive lattice distortion [17].

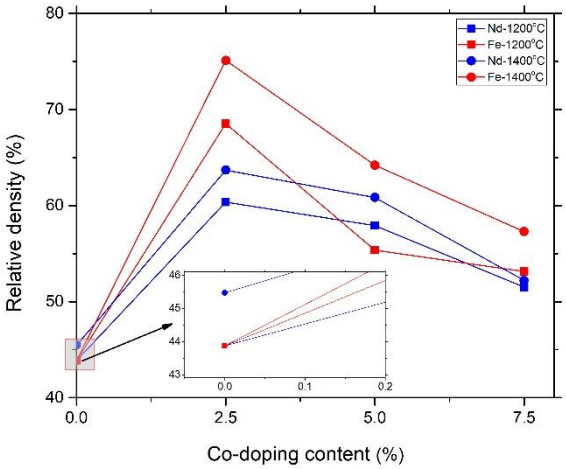

Figure 2. Relationship of co-doping concentration with relative density at sintering temperatures of 1200 °C and 1400 °C

Lattice distortion occurs along with changes in lattice parameters due to differences in radii and static forces between atoms. In GDC solid electrolyte, adding Fe_2O_3 at both 1200 °C and 1400 °C sintering temperatures results in higher densification than adding Nd_2O_3. This is because Fe_2O_3 acts as a sintering aid that can accelerate densification kinetics during the sintering process [18]. The highest densification (75%) was found in the GDC with the addition of Fe_2O_3 2.5%, which was sintered at 1400 °C.

The increases in the densification of the GDC with the addition of Fe_2O_3 were caused by viscous flow sintering occurred that can accelerate the densification kinetics [19]. Also, Figure 2 indicates that the densification will increase as the sintering temperature rises. At a higher sintering temperature, the atoms in the GDC get more energy to diffuse and form denser granules. However, if the sintering temperature is too high, the grain size will increase, which causes poor mechanical properties of the solid electrolyte.

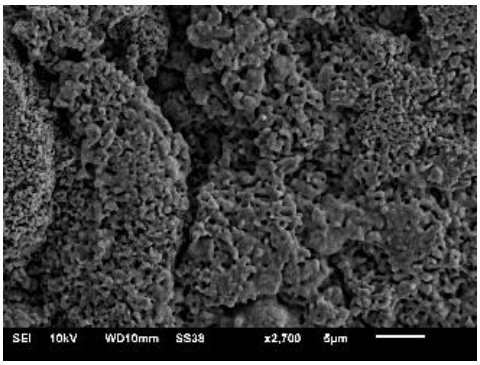

(a)

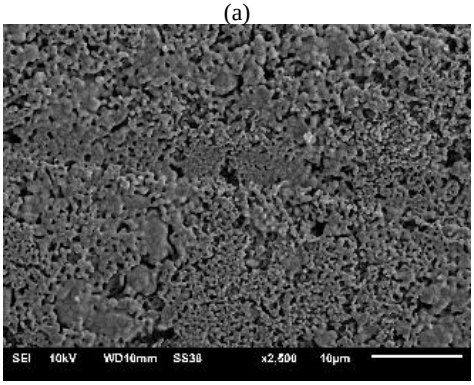

(b)

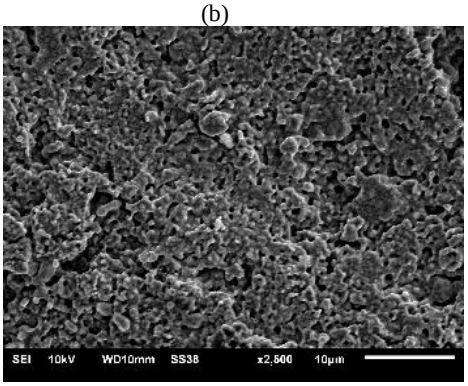

(c)

Figure 3. Microstructure of (a) GDC, (b) Nd-GDC, and (c) Fe-GDC sintered at 1400 °C and at 2.5%co-doping concentration

Figure 3 shows the microstructure of the GDC solid electrolyte GDC with Nd_2O_3 and Fe_2O_3 addition. In the microstructure of the GDC, large agglomerates were formed, which still have many pores and large grain sizes (1.227μm). The agglomerates disappeared when Nd_2O_3 was introduced to the GDC, producing finer granules with smaller grain sizes (0.642μm). This is consistent with Fig. 2, demonstrating that the GDC densification with Nd_2O_3 has a more excellent value than the GDC. According to studies by Priyadharsini et. al., [20], the presence of Nd in the ceria lattice could inhibit the agglomeration process, resulting in less aggregation of elements in specific places and smaller grain size. The microstructure generated in the GDC with the addition of Fe_2O_3 has fewer pores and a comparatively smaller grain size (0.906μm). In the Fe-GDC, it was also observed that the wet grain boundary cluster or the wetted grain boundary indicated the occurrence of viscous flow sintering [21]. This process occurs because of the liquid phase formed by the melting of the sintering aid. The liquid phase will fill the pores with capillary forces, which will then be reprecipitated at the final stage of sintering so that densification will increase.

3.3 Ionic Conductivity Analysis

Ionic conductivity is a quantity that expresses the ease of a material to transport ions. Ionic conductivity is determined by Equation (2), where σ is total ionic conductivity (S/cm), R_{total} is total resistance of solid electrolyte (Ω), L is thickness of solid electrolyte (cm) and A is area of solid electrolyte (cm^2).

$$\sigma = \frac{1}{R_{total}} \times \frac{L}{A} \qquad (2)$$

The total resistance of a solid electrolyte is the sum of the grain and grain boundary resistance. The grain and grain boundary conductivity can be determined to identify the contribution of grain and grain boundaries to the total conductivity. Grain and grain boundary conductivity can be calculated using the same equation shown in Equation (2), but the resistance value used is the resistance of each grain and grain boundary. Figure 4 shows the contribution of grain and grain boundaries to the total ionic conductivity of solid electrolytes GDC at an operating temperature of 450 °C. From Figure 4, it can be seen that the conductivity of the grain was larger than those of the grain boundary. Variances caused this variation in conductivity the concentration of vacancy within the grains and grain boundaries. The vacancy concentration inside the grains was more significant than the grain boundaries, resulting in a higher conductivity [22]. However, the grain boundary conductivity has a value and trend nearly identical to the total conductivity, implying that the grain boundary contribution was more prominent than the grain contribution to the total conductivity. It can also be explained by the microstructure shown in Fig. 3, where the GDC solid electrolyte with Nd_2O_3 and Fe_2O_3 addition has a tiny grain size, resulting in more grain boundaries than grains. Therefore, the contribution of grain boundaries is more dominant than grains.

At 5% co-doping concentration, there was a data anomaly. The grain boundary conductivity and total ionic conductivity of the GDC with Fe_2O_3 addition were higher than the GDC with Nd_2O_3 addition. This occurs because the grain boundary resistance in the GDC with Fe_2O_3 addition is lower than in the GDC with Nd_2O_3 addition, resulting in increased grain boundary conductivity.

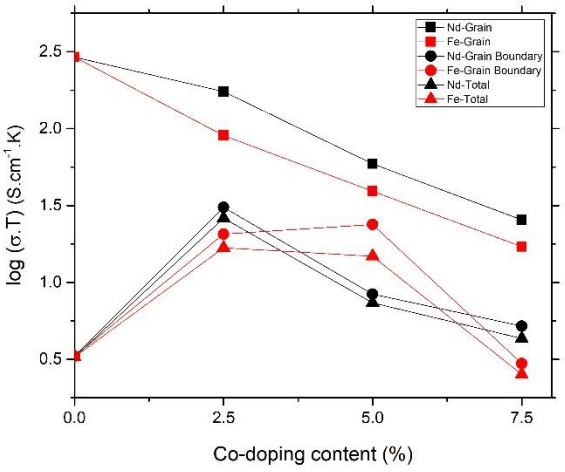

Figure 4. Grain and grain boundary contribution to total conductivity of GDCs sintered at 1200 °C and at 450 °C operating temperature

Figure 5 shows the relationship of co-doping a concentration with the total ionic conductivity. Ionic conductivity increases with the addition of Nd_2O_3 and Fe_2O_3 up to concentration of 2.5% and then decreases with further concentration increases. The decrease in ionic conductivity occurs because the density of the solid electrolyte drops at concentrations above 2.5%, as discussed in sub-section 3.2. It causes the mobility of oxygen ions to be slower, so the ionic conductivity decreases. Furthermore, high co-doping concentrations, it causes defects to interact with one another. Oxygen vacancy ($V\ddot{o}^{2+}$) would interact with other charged species and

produce a cluster defect, which causes the oxygen vacancy to be immobile [23]. Figure 6 compares the effect of adding Nd_2O_3 and Fe_2O_3 at 2.5% concentration and various operating temperatures on the total ionic conductivity. The highest ionic conductivity value obtained in this study was 1.2 mS/cm with the addition of 2.5% Nd_2O_3 at an operating temperature of 650 °C. This value is lower than the research conducted by Dikmen et.al., [24] and Kim et.al., [25], obtained ionic conductivity of 4.9 mS/cm and 4.3 mS/cm. This value is lower than the two previous studies because the two previous studies used a higher sintering temperature and a longer sintering time so that fewer pores were produced. The fewer pores cause the ionic conductivity to be higher than in this study.

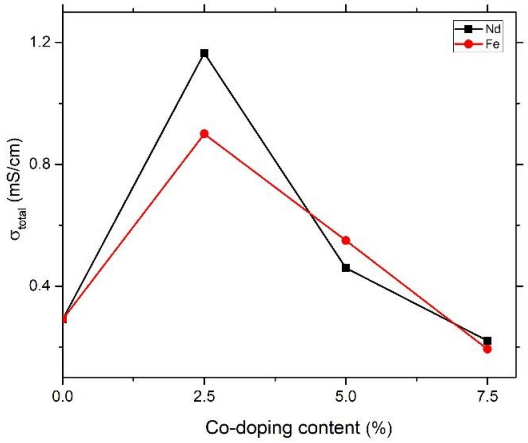

Figure 5. Relationship of co-doping concentration with total ionic conductivity

The ionic conductivity of the GDC with the addition of Nd_2O_3 has a higher value than the GDC with the addition of Fe_2O_3. The increase in ionic conductivity in the Nd-GDC was due to the rise in the vacancy concentration. When Nd_2O_3 is introduced, Nd^{3+} will replace Ce^{4+}, forming an oxygen vacancy defect [22]. The formation of this oxygen vacancy is written with the Kröger-Vink notation shown in Equation (3). The more oxygen vacancies formed, the easier the mobility of oxygen ions in the solid electrolyte so that the ionic conductivity increases.

$$Nd_2O_3 \rightarrow 2Nd_{Ce} + \text{Vö} + 3O_o^x \qquad (3)$$

The maximum ionic conductivity of the GDC with the addition of Fe_2O_3 was achieved at a concentration of 2.5%, which reached 0.89 mS/cm at an operating temperature of 650 °C. This value is greater than the previous study by Dong et.al., [26], which found 6×10^{-2} mS/cm of ionic conductivity. Furthermore, the Fe-GDC exhibits a higher ionic conductivity value than the Nd-GDC because Fe-GDC solid electrolytes have higher densification than GDC. Nevertheless, the addition of Fe_2O_3 is not directly related to the formation of oxygen vacancies, so the ionic conductivity value is lower than the Nd_2O_3 addition. Therefore, it can be concluded that Nd_2O_3 is the more effective material for increasing the ionic conductivity of solid electrolyte GDC compared to Fe_2O_3.

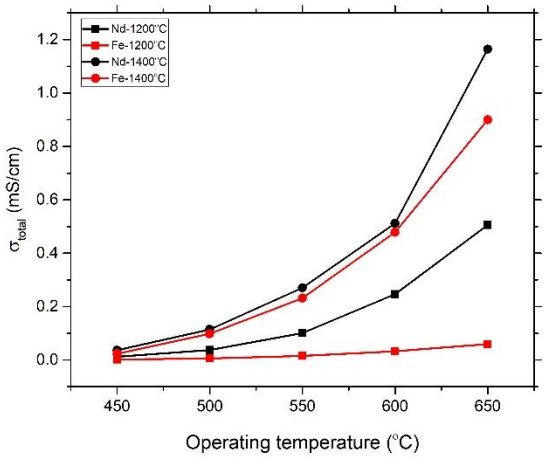

Figure 6. Comparison of the addition of 2.5% Nd_2O_3 and 2.5% Fe_2O_3 to the total ionic conductivity at various operating temperature

This also validates the research by Anderrson et.al., [10] described in the introduction, where the atomic number of Nd is closer to the atomic number of Pm.

3.4 Activation Energy Analysis

The ionic conductivity of the solid electrolyte is a function of the operating temperature. The dependence of ionic conductivity with operating temperature is usually shown by the Arrhenius plot, which can be seen in Fig. 7. As shown in Figure 7, generally, the ionic conductivity increases with increasing operating temperature because of the decrease in the total resistance of the solid electrolyte [27]. This is also consistent with the data shown in Fig. 6. As the operating temperature rises, the mobility of oxygen ions will increase, causing the ionic conductivity value to increase [18].

The activation energy of a solid electrolyte system can be calculated from the Arrhenius plot using Equation (3), where σ is total ionic conductivity (S/cm), σ_0 is a pre-exponential factor (S.K/cm), T is operating temperature (K), k is Boltzman constant, and Ea is activation energy (eV).

$$\sigma T = \sigma_0 \exp(-\frac{E_a}{k.T}) \qquad (3)$$

Figure 8 shows the relationship of co-doping concentration to the activation energy of the

GDC solid electrolyte system. In general, adding of Nd_2O_3 and Fe_2O_3 can reduce the activation energy of the solid electrolyte system. The lowest activation energy was achieved at a co-doping concentration of 2.5%.

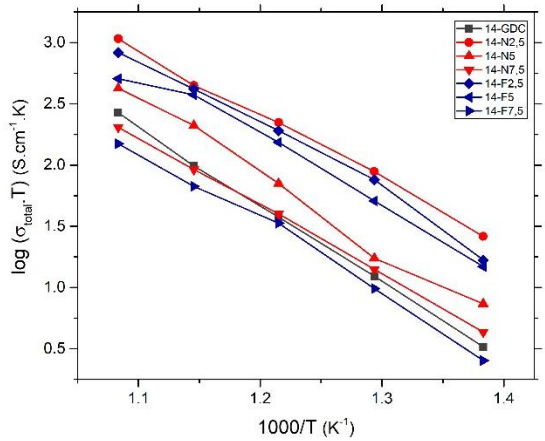

Figure 7. Arrhenius plot of the GDC sintered at 1400 °C

The GDC adding of Nd_2O_3 had a lower activation energy value than the GDC with the addition of Fe_2O_3. The activation energy of the GDC with the addition of 2.5% Nd_2O_3 reached 0.41 eV, while the addition of Fe_2O_3 reached 0.45 eV. These values have met the requirements for SOFC applications, which are below 1 eV [7]. The decrease in activation energy indicates that the energy required to release oxygen ions from the crystal lattice and ion migration becomes smaller so that the ionic conductivity increases [27].

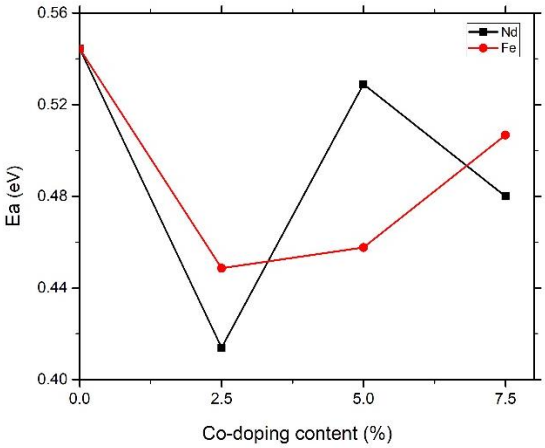

Figure 8. Activation energy of the GDC solid electrolyte

4. CONCLUSION

GDC (gadolinia doped ceria) solid electrolytes with Nd_2O_3 and Fe_2O_3 addition was successfully synthesized by mixed-oxide method. Based on the findings in this study, Nd_2O_3 and Fe_2O_3 added were dissolved in the ceria structure and produced single-phase cubic fluorite CeO_2. The highest densification, up to 75%, was obtained in the GDC solid electrolyte with Fe_2O_3 addition. The highest ionic conductivity and the lowest activation energy were obtained in the GDC with 2.5% Nd_2O_3 in 650°C operating temperature, with the values achieved were 1.2 mS/cm and 0.41 eV, respectively. It can be concluded that the addition of Nd_2O_3 is more effective than the addition of Fe_2O_3 in enhancing the ionic conductivity of GDC solid electrolyte and can lower the activation energy. The improvement in ionic conductivity is likely to improve SOFC cell performance at intermediate operating temperatures.

ACKNOWLEDGMENT

The author would like to thank the Solid Oxide System Laboratory ITB technicians who have helped during the research. The author would also like to thank the Head of the Metallurgical Engineering Masters Program ITB for granting permission to use research facilities.

REFERENCES

[1] R. O. Fuentes and R. T. Baker, "Synthesis and properties of Gadolinium-doped ceria solid solutions for IT-SOFC electrolytes," *Int. J. Hydrogen Energy*, vol. 33, no. 13, pp. 3480–3484, 2008. Doi: 10.1016/j.ijhydene.2007.10.026.

[2] P. Widiatmoko, H. Devianto, I. Nurdin, F. Yusupandi, Kevino, and E. N. Ovani, "Fabrication and characterization of intermediate-temperature solid oxide fuel cell (IT-SOFC) single cell using Indonesia's resources," *IOP Conf. Ser. Mater. Sci. Eng.*, vol. 550, no. 1, 2019. Doi: 10.1088/1757-899X/550/1/012001.

[3] Z. Gao, H. Wang, E. Miller, Q. Liu, D. Senn, and S. Barnett, "Tape casting of high-performance low-temperature solid oxide cells with thin La0.8Sr0.2Ga0.8Mg0.2O3-δ electrolytes and impregnated nano anodes," *ACS Appl. Mater. Interfaces*, vol. 9, no. 8, pp. 7115-7124, 2017. Doi: 10.1021/acsami.6b15224.

[4] Y. Fu, "Theoretical and experimental study of solid oxide fuel cell (SOFC) using impedance spectra signature redacted," M.A thesis, Massachusetts Institute of Technology, Cambrige, no 1. pp. 22-30, 2015.

[5] S. A. Kumar and P. Kuppusami, "*Enhancing the ionic conductivity in the ceria-based electrolytes for intermediate temperature solid oxide fuel cells*" in book Intemediate Temperature Solid Oxide

Fuel Cells. 1st edition. Gurbinder Kaur. Elsevier. pp 113-163, 2020.
[6] Y. Liu, "Application of rare-earth doped ceria and natural minerals for solid oxide fuel cells". Doctoral Thesis, KTH Royal Institute of Technology, Sweden, pp. 24-50, 2019.
[7] J. A. Kilner and M. Burriel, "Materials for intermediate temperature solid-oxide fuel cells", *Annual Review of Materials Research*, vol. 44, pp. 365-393, 2014. Doi: 10.1146/annurev-matsci-070813-113426.
[8] J. Van Herle, D. Seneviratne, and A. J. McEvoy, "Lanthanide co-doping of solid electrolytes: AC conductivity behaviour," *J. Eur. Ceram. Soc.*, vol. 19, no. 6-7, pp. 837-841, 1999. Doi: 10.1016/s0955-2219(98)00327-6.
[9] N. Jaiswal, K. Tanwar, R. Suman, D. Kumar, S. Uppadhya, and O. Parkash, "A brief review on ceria based solid electrolytes for solid oxide fuel cells," *J. Alloys Compd.*, vol. 781, pp. 984-1005, 2019. Doi: 10.1016/j.jallcom.2018.12.015.
[10] C. J. Luo, R. Q. Liu, Z. Q. Deng, M. Li, and J. J. Shen, "Experimental investigations of an energy absorber based on thin-walled metal tube's plastic deformation," *Zhendong yu Chongji/Journal Vib. Shock*, vol. 29, no. 4, pp. 101-106, 2010.
[11] R. M. Ormerod, "Solid oxide fuel cells," *Chem. Soc. Rev.*, vol. 32, no. 1, pp. 17-28, 2003. Doi: 10.1039/b105764m.
[12] S. Y. Toor and E. Croiset, "Reducing sintering temperature while maintaining high conductivity for SOFC electrolyte: Copper as sintering aid for Samarium Doped Ceria," *Ceram. Int.*, vol. 46, no. 1, pp. 1148-1157, 2020. Doi: 10.1016/j.ceramint.2019.09.083.
[13] J. Cheng, C. Tian, and J. Yang, "Effects of Fe_2O_3 addition on the electrical properties of SDC solid electrolyte ceramics," *J. Mater. Sci. Mater. Electron.*, vol. 30, no. 17, pp. 16613-16620, 2019. Doi: 10.1007/s10854-019-02040-2.
[14] A. Arabacı, T. G. Altınçekiç, M. Der, and M. A. F. Öksüzömer, "Preparation and properties of ceramic electrolytes in the Nd and Gd Co-doped ceria systems prepared by polyol method," *J. Alloys Compd.*, vol. 792, pp. 1141-1149, 2019. Doi: 10.1016/j.jallcom.2019.04.098.
[15] S. Soepriyanto. Y. Aristanti, T. Teresia, MA. Sulthon, F. Baqir, W.P. Minwal, and B. Dilasari, "Comparative effect of REO co-dopant (La, Y, Nd) on ionic conductivity of Gd-doped CeO2 solid electrolyte for IT-SOFC," *J. Aust. Ceram. Soc.*, vol. 55, no. 4, pp. 1161-1165, 2019. Doi: 10.1007/s41779-019-00332-8.
[16] A. Arabacı, "Citrate/nitrate combustion synthesis and electrical properties of rare earth co-doped Ce0.8Gd0.2−xNdxO1.90 electrolyte materials," *Mater. Sci. Eng. B Solid-State Mater. Adv. Technol.*, vol. 260, 2020. Doi: 10.1016/j.mseb.2020.114646.
[17] A. Nugroho, S. Soepriyanto, "Karakteristik fisik dan konduktivitas spesifik batas butir dari elektrolit padat gadolinium veria (GC) untuk aplikasi bahan bakar oksida padat temperatur menengah," *Majalah Ilmu dan Teknologi* vol. 35, no 1, 2020. Doi : 10.14203/metalurgi.v35i1.467.
[18] Y. Zheng, M. Zhou, L. Ge, S. Li, H. Chen, and L. Guo, "Effect of Fe_2O_3 on Sm-doped ceria system solid electrolyte for IT-SOFCs," *J. Alloys Compd.*, vol. 509, no. 2, pp. 546-550, 2011. Doi: 10.1016/j.jallcom.2010.09.103.
[19] Z. Wang, Y. Zeng, C. Li, Z. Ye, L. Cao, and Y. Zhang, "Structures and electrical conductivities of Gd3+ and Fe3+ co-doped cerium oxide electrolytes sintered at low temperature for ILT-SOFCs," *Ceram. Int.*, vol. 44, no. 9, pp. 10328-10334, 2018. Doi: 10.1016/j.ceramint.2018.03.041.
[20] N. Priyadharsini, M. Thamilselvan, S. Sangeetha, and S. Vairam, "Effect of neodymium substitution on structural, optical, magnetic and antibacterial activity of zinc selenide nanoparticles," *J. Ovonic Res.*, vol. 12, no. 2, pp. 87-93, 2016.
[21] Limthongkul. P, Jivagonant. P, Loyma. N, Pannaram. N, and Charojrochukul. S, "Effect of Fe addition on densification and conduction property of gadolinia doped ceria," E. C. S. Transactions and T. E. Society, vol. 25, no. 2, pp. 1555-1563, 2009.
[22] A. S. Babu, R. Bauri, and G. S. Reddy, "Processing and conduction behavior of nanocrystalline Gd-doped and rare earth co-doped ceria electrolytes," *Electrochim. Acta*, vol. 209, pp. 541-550, 2016. Doi: 10.1016/j.electacta.2016.05.118.
[23] D. G. Syarif, S. Soepriyanto, Ismunandar, and A. A. Korda, "Effect of LSGM addition on electrical characteristics of 8ysz ceramics for solid electrolyte," *J.*

Aust. Ceram. Soc., vol. 49, no. 2, pp. 52-59, 2013.

[24] S. Dikmen, H. Aslanbay, E. Dikmen, and O. Şahin, "Hydrothermal preparation and electrochemical properties of Gd^{3+} and Bi^{3+}, Sm^{3+}, La^{3+}, and Nd^{3+} codoped ceria-based electrolytes for intermediate temperature-solid oxide fuel cell," *J. Power Sources*, vol. 195, no. 9, pp. 2488-2495, 2010. Doi: 10.1016/j.jpowsour.2009.11.077.

[25] N. Kim, B. Kim, and D. Lee, "Effect of co-dopant addition on properties of gadolinia-doped ceria electrolyte," *Journal of Power Source*s, vol. 90, no. 2, pp. 139-143, 2000. Doi: 10.1016/S0378-7753(00)00389-X.

[26] Q. Dong, Z. H. Du, T. S. Zhang, J. Lu, X. C. Song, and J. Ma, "Sintering and ionic conductivity of 8YSZ and CGO10 electrolytes with small addition of Fe_2O_3: A comparative study," *Int. J. Hydrogen Energy*, vol. 34, no. 19, pp. 7903-7909, 2009. Doi: 10.1016/j.ijhydene.2009.06.042.

[27] Y. Liu, B. Li, X. Wei, and W. Pan, "Citric-nitrate combustion synthesis and electrical conductivity of the Sm3+ and Nd3+ co-doped ceria electrolyte," *J. Am. Ceram. Soc.*, vol. 91, no. 12, pp. 3926-3930, 2008. Doi: 10.1111/j.1551-2916.2008.02748.x.

METALURGI
Majalah Ilmu dan Teknologi
p-ISSN 0126-3188 | e-ISSN 2443-3926
ejurnalmaterialmetalurgi.lipi.go.id

SYNTHESIS AND CHARACTERISTIC OF NANO SILICA FROM GEOTHERMAL SLUDGE: EFFECT OF SURFACTANT

Aufa Rai Adiatama[a], Ratna Frida Susanti[a], Widi Astuti[b], Himawan Tri Bayu Murti Petrus[c], Kevin Cleary Wanta[a,*]

[a]Department of Chemical Engineering, Parahyangan Catholic University
Jl. Ciumbuleuit No. 94, Bandung, Indonesia 40141
[b]Reseach Unit for Mineral Technology, National Research and Innovation Agency
Jl. Ir. Sutami Km. 15 Tanjung Bintang, Indonesia 35361
[c]Department of Chemical Engineering, Universitas Gadjah Mada
Jl. Grafika No. 2 Kampus UGM, Yogyakarta, Indonesia 55281
*E-mail: kcwanta@unpar.ac.id

Received: 29-03-2022, Revised: 08-09-2022, Accepted: 04-10-2022

Abstract

In the synthesis of nanoparticles, the phenomenon of agglomeration is an undesirable condition because the particles formed can be larger. The use of surfactants can prevent the occurrence of this phenomenon. In this study, the use of surfactants was studied in the synthesis of nano silica from geothermal sludge. The method applied in the synthesis of nano silica is the sol-gel method. A 1 M NaOH (sodium hydroxide) solution was used to prepare of the precursor solution, while the SiO_2 gel formation was carried out at a pH of 5 using a 1.5 M HCl (hydrochloric acid) solution. The surfactants used were ABS (alkyl benzene sulfonate), CTAB (cetyltrimethylammonium bromide), SDS (sodium dodecyl sulfate), and PVP (polyvinylpyrrolidone). The surfactant added to the precursor solution was at the CMC (critical micelle concentration), where the CMC value for each surfactant was 0.15; 0.05; 0.50; and 1.00 wt% for ABS, CTAB, SDS, and PVP, respectively. As a comparison, nano silica synthesis was also carried out without adding of surfactants. The experimental results showed that the synthesis of nano silica without surfactant produced a product with a purity of 98.03%. Based on PSA (particle size analyzer) testing, the average particle size was 4.82 μm. Although the purity was already high, the resulting product experiences agglomeration and surfactants were needed to minimize the occurrence of agglomeration in the product. The surfactant that gives the best product quality is PVP, whose average particle size is 66% smaller than the product without surfactant. However, the effect produced with PVP has a low purity, which is 56.67%. This condition occurs because NaCl was trapped in the surfactant template. The presence of this surfactant template causes the washing process more difficult because the templates become an obstacle for water to diffuse into the particles and dissolve the impurities.

Keywords: *Agglomeration, nano silica, geothermal sludge, surfactant*

1. INTRODUCTION

In general, nanoparticles can be defined as particles having sizes in nanometers or more precisely, in the range of 1 and 100 nm [1]-[2]. By having a smaller size, nanoparticles have different characteristics from their bulk particles in several properties, such as the properties of physical (especially particle surface area), chemical, magnetic, electrical, and optical [3]-[6]. One of the nanoparticles that has excellent potential to be utilized is silica-based nanoparticles or usually referred to as nano silica. Nano silica has a large surface area, high stability, good heat and electrical resistance, and is inert [7]. Those properties are the reasons why nano silica is widely applied in various sectors. Utilization of nano silica as the main and/or supporting material is carried out for applications in the sectors of adsorption, catalysts, drug delivery systems, insulators, sensors, polymers, paints, and energy [8]-[12].

Based on several previous studies, the synthesis of nano silica has been widely studied using raw materials or precursor solutions, such

DOI : 10.14203/metalurgi.v37i2.637

Metalurgi is Sinta 2 Journal (https://sinta.ristekbrin.go.id/journals/detail?id=3708) accredited by Ministry of Research & Technology, Republic Indonesia

as TEOS (tetraethyl orthosilicate), rice husks, and silica sand [13]-[15]. Raw materials that can be employed to synthesize nano silica must contain high silica. In addition to the three materials previously mentioned and studied, there is another raw material that has excellent potential to be employed as a source of silica, namely geothermal sludge.

Geothermal sludge is solid waste generated from geothermal power plants. The amount of geothermal sludge produced from one power plant can reach hundreds of thousands of tons per month and this value is classified as very abundant for a waste [16]. If this waste is left alone, it will cause environmental problems. Based on its characteristics, this geothermal sludge contains several mineral elements or compounds that can be utilized. The most prominent mineral in geothermal sludge is silicon dioxide (SiO_2) compounds in amorphous form. The SiO_2 content in this sludge can reach 98% [17]-[19]. These data indicate that this geothermal sludge has enormous potential to be used as raw material for nano silica synthesis. On the other hand, studies on the utilization of this waste as raw material for nano silica have not been studied much and deserve further study because there is still unknown information.

In the synthesis of nano silica, the most widely used method is the sol-gel method. The sol-gel method involves the polymerization of inorganic compounds through chemical reactions in a precursor solution to form oxide compounds. The formation of these oxide compounds includes the stages of hydrolysis (formation of the sol phase-colloid) and changes in shape from the sol phase to the gel phase through the gelation stage [20]-[22]. This method has several advantages, such as producing homogeneous and high purity products, cheap, simple, and easy to operate [22]-[23]. However, the biggest challenge of synthesizing nano silica using the sol-gel method is agglomeration between particles during the gelation stage.

Agglomeration is a phenomenon in which two or more particles bind to each other for an extended period [24]. This phenomenon will cause the particles formed to be larger or the worst conditions; the resulting product is not nanometer in size. Efforts to prevent this phenomenon can be done by adding surfactants to the solution [25]-[28]. Singh, et. al., [29] have conducted studies regarding the use of several surfactants, such as CTAB (cetyltrimethyl-ammonium bromide), TTAB (tetradecyltrimethyl-ammonium bromide), and DTAB (dodecytrimethyl-ammonium bromide), in the synthesis of nano silica. The results of their research proved that the use of CTAB surfactant was able to reduce the nano silica particle size by almost 70%. In addition, another study conducted by Rakhmasari, et. al., [30] also proved that the use of ABS (alkyl benzene sulfonate) surfactant with a certain concentration can reduce the nano silica particle size by about 30% for the treatment without sonication and 47% for the treatment with sonication.

The focus of this work emphasizes the use of surfactants in the nano silica synthesis using geothermal sludge as raw material. It needs to be studied more deeply because there is no detailed and specific information regarding surfactants in the nano silica synthesis from geothermal sludge, especially the effect of the type of surfactant used. This work will study the use of various types of surfactants (cation and anion surfactants). Different types of surfactants will affect the characteristics of the nano silica formed, including particle size and morphology [29], [31]. Therefore, it will also be seen how the characteristics of the formed product where the use of surfactants with the right concentration is expected to give better characteristics to the nano silica product.

2. MATERIALS AND METHODS

2.1 Materials

For this work, geothermal sludge was the main raw material in the synthesis of nano silica. The sludge was derived from PLTP Geo Dipa Dieng, Indonesia. The sludge contained several mineral compounds and the composition of the sludge is shown in Table 1.

Table 1. The composition of geothermal sludge

Element	Composition (wt.%)
SiO_2	96.79
K_2O	0.91
P_2O_5	0.89
Fe_2O_3	0.89
CaO	0.40
Others	0.12

Other main materials employed for this synthesis of nano silica were NaOH (sodium hydroxide) and HCl (hydrochloric acid). In addition, the surfactant types varied for this work were ABS (alkyl benzene sulfonate), CTAB (cetyltrimethyl-ammonium bromide), SDS (sodium dodecyl sulfate), and PVP (polyvinylpyrrolidone). Demineralized water was applied as a solvent for all materials.

2.1 Procedures

In general, this research procedure can be illustrated a workflow as shown in Figure 1. Geothermal sludge was ground with a mortar and pestle to a size of particle less than 74 microns. Then, 20 grams of geothermal sludge were mixed with 800 ml of 1 M NaOH solution. The mixture was stirred using a magnetic stirrer and a hot plate at 90 ^{o}C for 60 minutes isothermally. After the reaction occurred, the mixture was filtered under vacuum conditions to obtain a supernatant containing Na_2SiO_3 (sodium silicate). This supernatant will act as a precursor solution for nano silica synthesis.

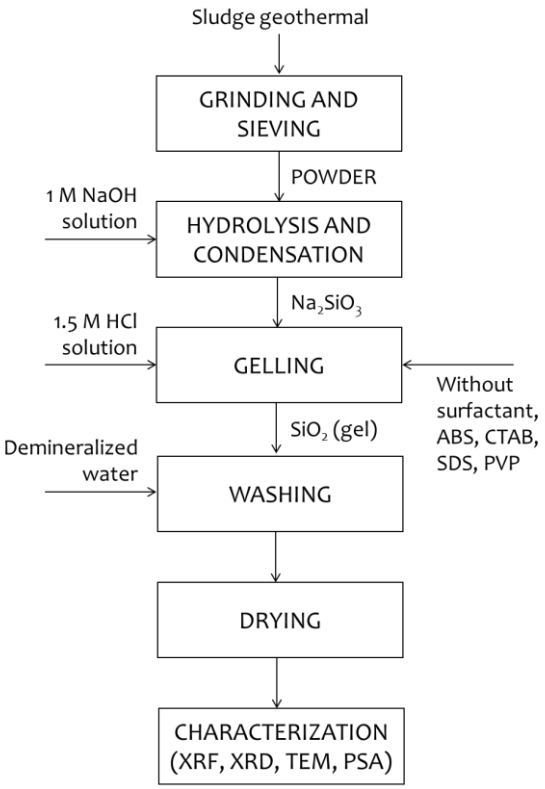

Figure 1. The procedure of this research

A total of 400 mL of the precursor solution was taken and added with surfactant. There were four types of surfactants studied, namely ABS (alkyl benzene sulfonate), CTAB (cetyltrimethyl-ammonium bromide), SDS (sodium dodecyl sulfate), and PVP (polyvinylpyrrolidone). The addition of surfactant was carried out at the CMC (critical micelle concentration). CMC was obtained first by testing the turbidity and surface tension of the precursor solution mixture with surfactants. In this experiment, the surfactant concentration was varied in a particular range according to the character of surfactant. The variation of surfactant concentration is presented in Table 2.

A turbidity meter was used to measure the turbidity level in a mixture of precursor solutions and surfactants. Meanwhile, the Du-Nouy tensiometer was used to measure the surface tension of the mixture. The CMC value was confirmed by making a graph between the surfactant concentration and the values of both physical parameters. Then, the graph was evaluated and compared with the graph of CMC determination, as depicted in Fig. 2.

Table 2. The range of surfactant concentration in the confirmation of CMC

Surfactant	Surfactant (wt.%)
ABS	0 – 2.0
CTAB	0 – 0.5
SDS	0 – 10.0
PVP	0 – 20.0

The precursor solution, added with surfactant in CMC, was stirred with a magnetic stirrer for 60 minutes. The 1.5 M HCl solution was then dripped while stirring until the pH of the solution reached 5 and a SiO_2 solid (gel) was formed. The solution was left for 18 hours so that the aging stage could occur. After the aging stage was complete, the separation process between the solid and liquid was carried out in a vacuum condition.

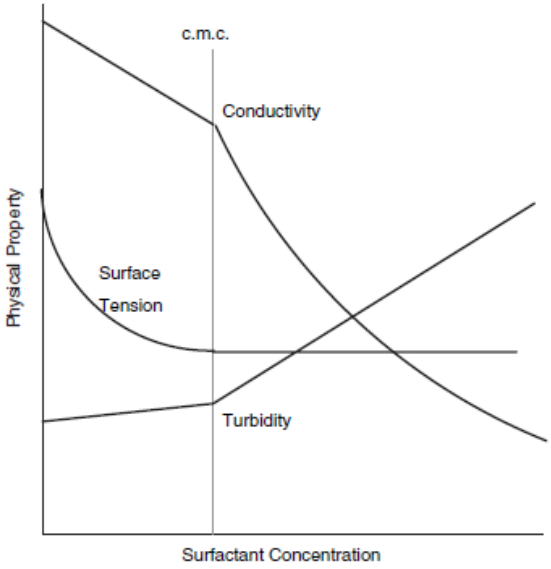

Figure 2. Comparison chart for confirmation of CMC value [32]

The solid formed was washed using 250 mL of demineralized water. The washing process was carried out with a stirring process for 10 minutes in four stages. It carried out in four stages aims to ensure the SiO_2 product has a high purity where the salt impurities (NaCl) dissolve in water. The solid was then dried using a microwave at 700 watts of power for 30 minutes. The final step is that the solids formed are characterized. The characterizations carried out were testing the

product composition using XRF (x-ray fluorescence), the mineral phase of the product using XRD (x-ray diffraction), particle size distribution using PSA (particle size analyzer), and product morphology using a TEM (transmission electron microscope). As a comparison, this study also synthesized nano silica without surfactants. The synthesis steps are the same as previously described.

3. RESULT AND DISCUSSION

3.1 Characterization of Nano silica without Surfactant

Before studying further the effect of surfactants in the synthesis of nano silica from geothermal sludge, the synthesis of nano silica without surfactants needs to be observed first so that it is obtained sharper observations regarding the effect of these parameters. This section shows how the results of nano silica synthesis without the addition of surfactants. The first result observed is the purity of the resulting nano silica product. The results of the analysis can be observed in Table 3.

Table 3. The composition of nano silica without surfactant

Compound	Composition (wt.%)
SiO_2	98.03
P_2O_5	0.97
Fe_2O_3	0.57
CaO	0.31
Others	0.12

Based on the analysis results in Table 3, the purity of the resulting nano silica has increased from the initial raw material. It can be seen that there is an increase of 1.24%, where the product purity is 98.03%. When compared with several other studies [33]-[34], the purity of the product obtained in this study is relatively high.

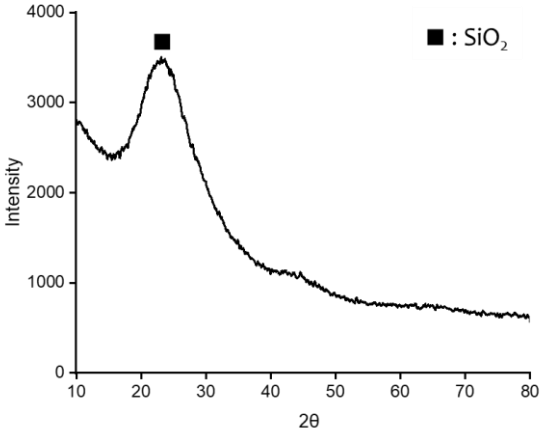

Figure 3. XRD analysis of nano silica products formed without surfactants

To strengthen the results of XRF (x-ray fluorescence) analysis, the mineral phase of the formed nano silica was also analyzed using XRD (x-ray diffraction). The results of the analysis are presented in Fig. 3. Based on Fig. 3, it can be observed that the nano silica product has a peak of about 23.5^o where this peak appears in the range of 16.3-33.8^o. Based on the range of peaks presented in Fig. 3, it also prove that the product formed is an amorphous compound.

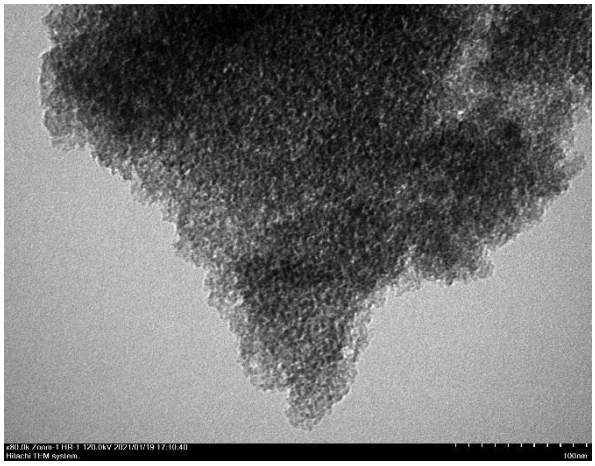

(a)

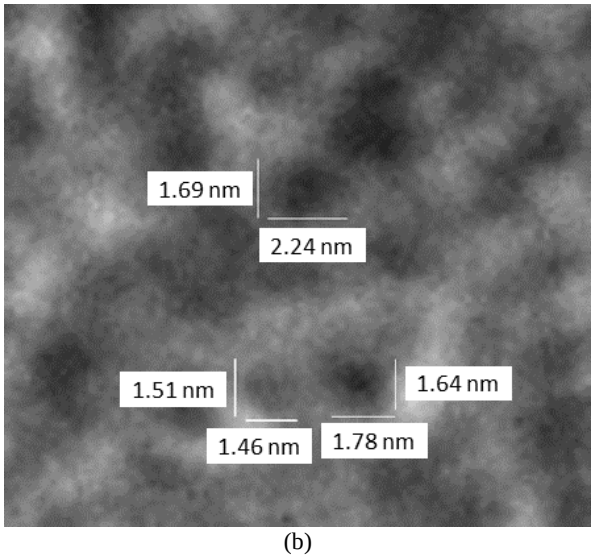

(b)

Figure 4. (a) TEM analysis and (b) size measurement using ImageJ software of nano silica products formed without surfactants

Morphologically, the resulting product was also characterized using TEM (transmission electron microscope) and the characterization results are presented in Fig. 4. Figure 4 indicates that the shape of the resulting nano silica is spherical. Meanwhile, the resulting silica product has a size in nanometers or, more precisely, in the range of 1.46-2.24 nm (see Fig. 4(b)). However, Fig. 4(a) proves that even though the product size is in nanometer units, the nano silica product experiences an enormous agglomeration

phenomenon. In the synthesis of nanoparticles through the sol-gel method, the phenomenon of agglomeration is a common thing to occur. Therefore, this study will be continued to study the use of surfactants as an effort to prevent the agglomeration phenomenon.

3.2 Confirmation of CMC (Critical Micelle Concentration) for Nano silica Synthesis from Sludge Geothermal

In the synthesis of nanoparticles using surfactants, the confirmation of the CMC (critical micelle concentration) is a crucial step. This step has a significant role in forming particles with the size of the nanometer scale because it reduces the possibility of agglomeration. In this study of nano silica synthesis from geothermal sludge, the CMC was confirmed by observing two parameters, namely the surface tension and turbidity in the mixture solution between precursor solution and surfactant. The experimental results for confirming the CMC can be seen in Fig. 5. The graph depicted in Fig. 5 was then compared with Fig. 2 so that CMC could be confirmed. The CMC results of comparing both figures are presented in Table 4.

The synthesis of nano silica without surfactants will make the silica product easier to agglomerate as illustrated in Figure 6a. When the system is in the CMC, the surfactants will aggregate to form micelles. The formation of micelles occurs because the positive groups of surfactants will be adsorbed on the negatively charged nano silica surface to envelop and surround the Na_2SiO_3 solution. It causes SiO_2 (nano silica) formation (gelling stage) to occur in the template or micelles. Under this condition, the possibility of nano silica to agglomerate is low (see Figure 6c).

However, at surfactant concentrations below the CMC, the amount of surfactant present in the solution is not sufficient to protect the entire surface of the surfactant and form micelles. As a result, the formed nano silica still undergoes an agglomeration process between particles (see Fig. 6(b)).

Table 4. The CMC value in the synthesis of nano silica from geothermal sludge

Surfactant	Surfactant Concentration (wt%)
ABS	0.15
CTAB	0.05
SDS	0.50
PVP	1.00

Meanwhile, if the system is above the CMC, the surfactant will form a double layer in which the surfactant previously adsorbed on the silica surface will bind to other surfactants (see Fig. 6(d)).

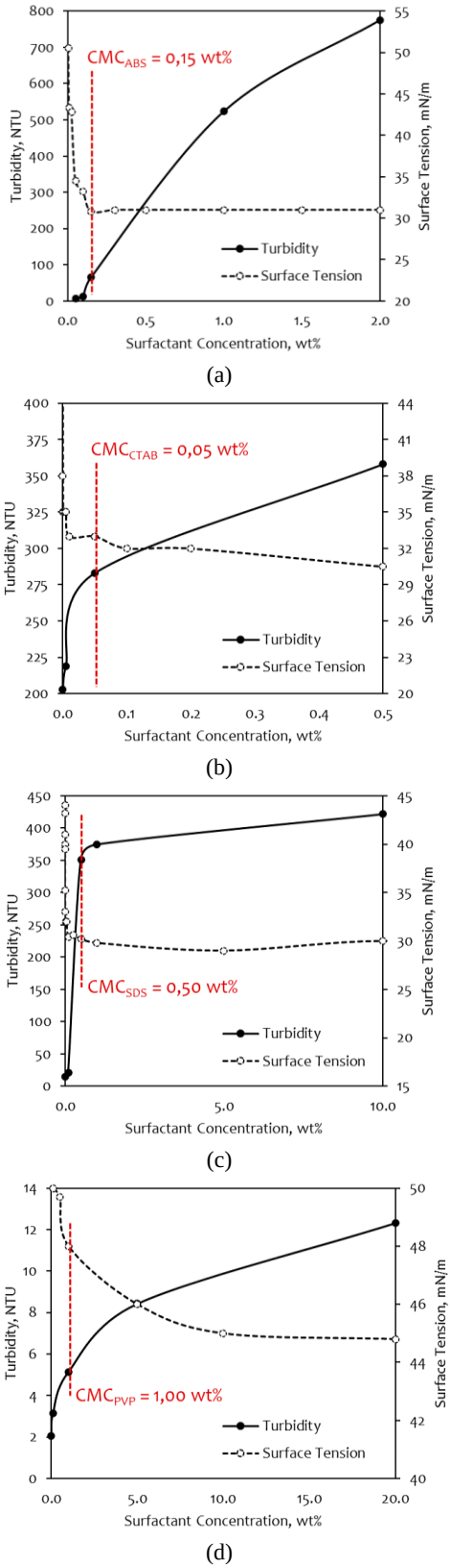

Figure 5. The value of turbidity and surface tension in the solution using surfactant (a) ABS, (b) CTAB, (c) SDS, and (d) PVP

It is due to the excessive amount of surfactant in the solution, which can cause the attractive

force (van der Waals force) between the surfactant and the nano silica surface to be weak so that the surfactant will be released from the nano silica so that the nano silica becomes unprotected and easily agglomerates [35].

Therefore, the surfactant concentration in CMC is the most optimal concentration to protect the nano silica particles from clumping or agglomeration.

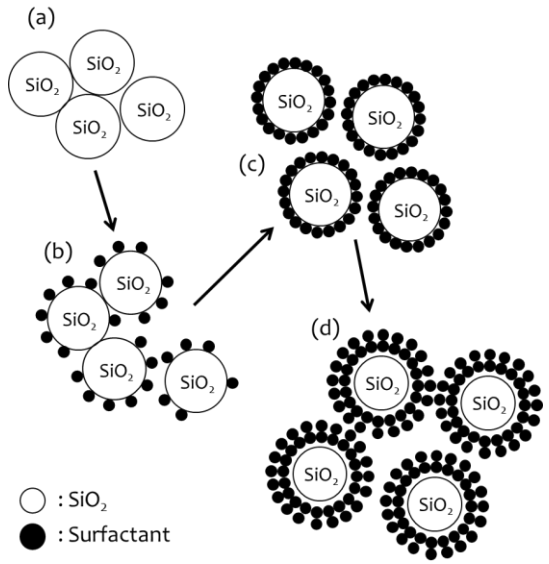

Figure 6. The illustration of the role of surfactants in the synthesis of nano silica (SiO_2)

3.3. Characterization Nano silica with the Addition of Surfactants

This section discusses the effect of using surfactants on the formed nano silica products. The first thing to be discussed is the composition of the nano silica product. The characterization results are presented in Fig. 7. The figure shows a significant decrease in SiO_2 levels in the products synthesized using surfactants. The purity of nano silica with surfactants ranged from 56.77-80.21 wt.%. This reduction in product purity occurs because there is Cl (chloride) based impurities detected in the product. Based on the characterization results, the composition of the Cl impurities ranged from 17.85 to 41.33 wt.%.

The nano silica product with this surfactant was further characterized, especially the compounds contained in this nano silica product. In particular, the determination of the mineral phase is aimed at identifying the impurity compounds in the product. The results of the characterization of this compound are presented in Fig. 8. In general, the formed nano silica products are still dominated by SiO_2 compounds in amorphous form. However, when observed in more detail in Figs. 8(b) to 8€, there are new peaks identified as NaCl (sodium chloride) crystals. It further confirms the test of the composition of the nano silica product in which there is a large amount of chloride-based impurities.

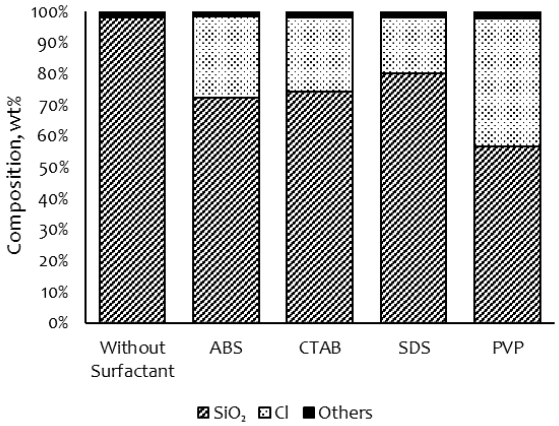

Figure 7. The composition of nano silica formed without and with surfactant

The formation of this NaCl salt is possible during the nano silica synthesis process using the sol-gel method.

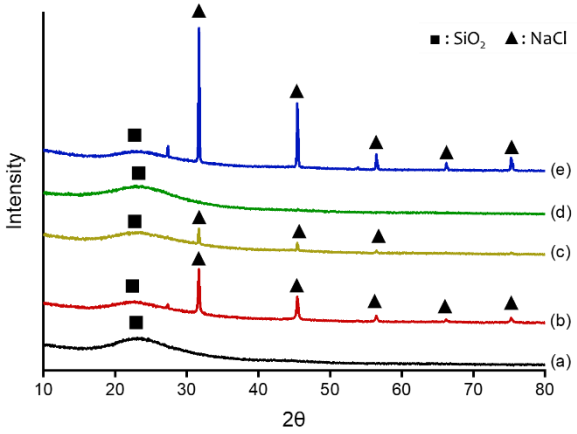

Figure 8. XRD results of nano silica formed (a) without surfactant, with surfactant (b) ABS, (c) CTAB, (d) SDS, and (e) PVP

It can be seen from the following mechanism and chemical reaction equation [22], [36]-[38].

Hydrolysis (basic catalyst)

$OH^- + \equiv Si–OR \rightarrow \equiv Si–OH + OR^-$ (1)

$OR^- + H_2O \rightarrow ROH + OH^-$ (2)

Condensation

$\equiv Si–OH + OH^- \leftrightarrow \equiv Si–O^- + H_2O$ (3)

$\equiv Si–OH + \equiv Si–O–R \rightarrow \equiv Si–O–Si\equiv + ROH$ (4)

$\equiv Si–OH + \equiv Si–O–H \rightarrow \equiv Si–O–Si\equiv + H_2O$ (5)

Gelling

$Na_2SiO_3 + HX \rightarrow SiO_2 + NaX + H_2O$ (6)

Overall reaction (for this study):

$SiO_2 + 2NaOH \rightarrow Na_2SiO_3 + H_2O$ (7)

$Na_2SiO_3 + HCl \rightarrow SiO_2 + NaCl + H_2O$ (8)

In nano silica synthesis, surfactants will form micelles (or can be considered as templates) where the SiO_2 gel (solid) formation process occurs in the template. Therefore, based on equation (2), the formed NaCl is trapped in the template and a saturated condition, NaCl will crystallize into salt and be bound in nano silica products.

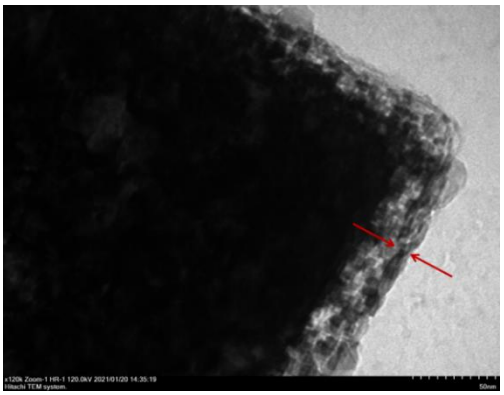

(a)

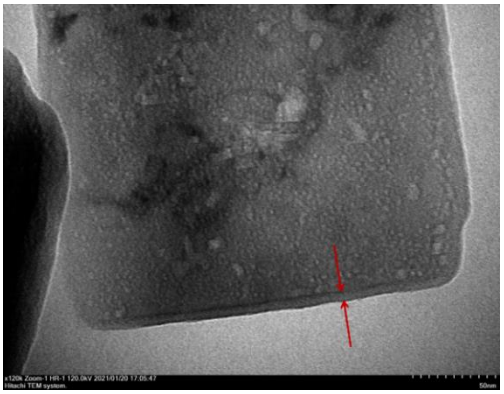

(b)

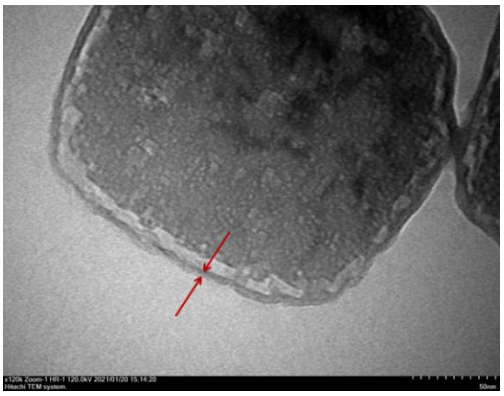

(c)

Figure 9. Surfactant template on nano silica formed with surfactant (a) ABS, (b) CTAB, and (c) SDS

The formation of these salts inevitably occurs in both the nano silica synthesis without and with surfactants. However, when seen in Figs. 7 and 8, the NaCl was not found in the nano silica product without surfactant. It happens because of the washing process that will dissolve the salt completely. The washing process with the same procedure was also carried out on the other four nano silica products (with surfactants). However, this washing process cannot completely dissolve the salt impurities. The salt is still trapped in the solid because there is still a template (miscellaneous) that surrounds the surface of the solid. The presence of this template makes it very difficult for water to diffuse into the solid and dissolve the salt.

The micelle formation of this surfactant causes the outer part of the template to be more hydrophobic due to the influence of the tail portion of the surfactant. It causes water, as a washing medium, to be retained on the outside of the template and form a thin layer [25], [39]. This concept applies to this study because it is supported by the results of characterization using the TEM (transmission electron microscope) instrument to show the morphology of the product and the template that is still left behind. The characterization results are presented in Fig. 9, and the template in question is indicated by arrows.

This study also characterize the size distribution of the formed particles and the results are presented in Fig. 10. Based on that figure, there are two peaks in the product produced using ABS and PVP surfactants (see Figs. 10(b) and 10€) and indicates that there are two different particle size distributions. One of the peaks proves that SiO_2 particles have a particle size (in bulk) in the range of 100-300 nm. When compared with the product without surfactant (see Fig. 10(a)), both surfactants were able to reduce the formation of agglomerates. Based on the tests carried out with PSA, quantitatively, the average diameter of the nano silica product particles changed from 4,822.9 nm (without surfactant) to 1,256.6 nm (for ABS) and 1,625.1 nm (for PVP). This shows that in this study, the use of the two surfactants was able to reduce the particle size between 66.30-73.95%.

Morphologically, the nano silica products synthesized with four types of surfactants were characterized using a TEM instrument. The characterization results are presented in Fig. 11. When compared to the nano silica product without surfactant (Fig. 4), the particle shape of the nano silica with surfactant also resembles a spherical shape. However, if seen in Figs. 11(a) to 11(c) (ABS, CTAB, and SDS surfactants), the interparticles formed are still agglomerated even though each particle is nanometer in size. However, the use of PVP (Fig. 10(d)) showed its success in preventing agglomeration between particles. The size of the nano silica synthesized

with PVP surfactant ranged from 2.01-3.65 nm (measurements were made using ImageJ software). The results obtained in this study are in line with the study conducted by Stanley and Nesaraj [26] where in their study, the use of PVP in the synthesis of nano silica from TEOS resulted in the smallest mean particle diameter compared to CTAB and SDS surfactants.

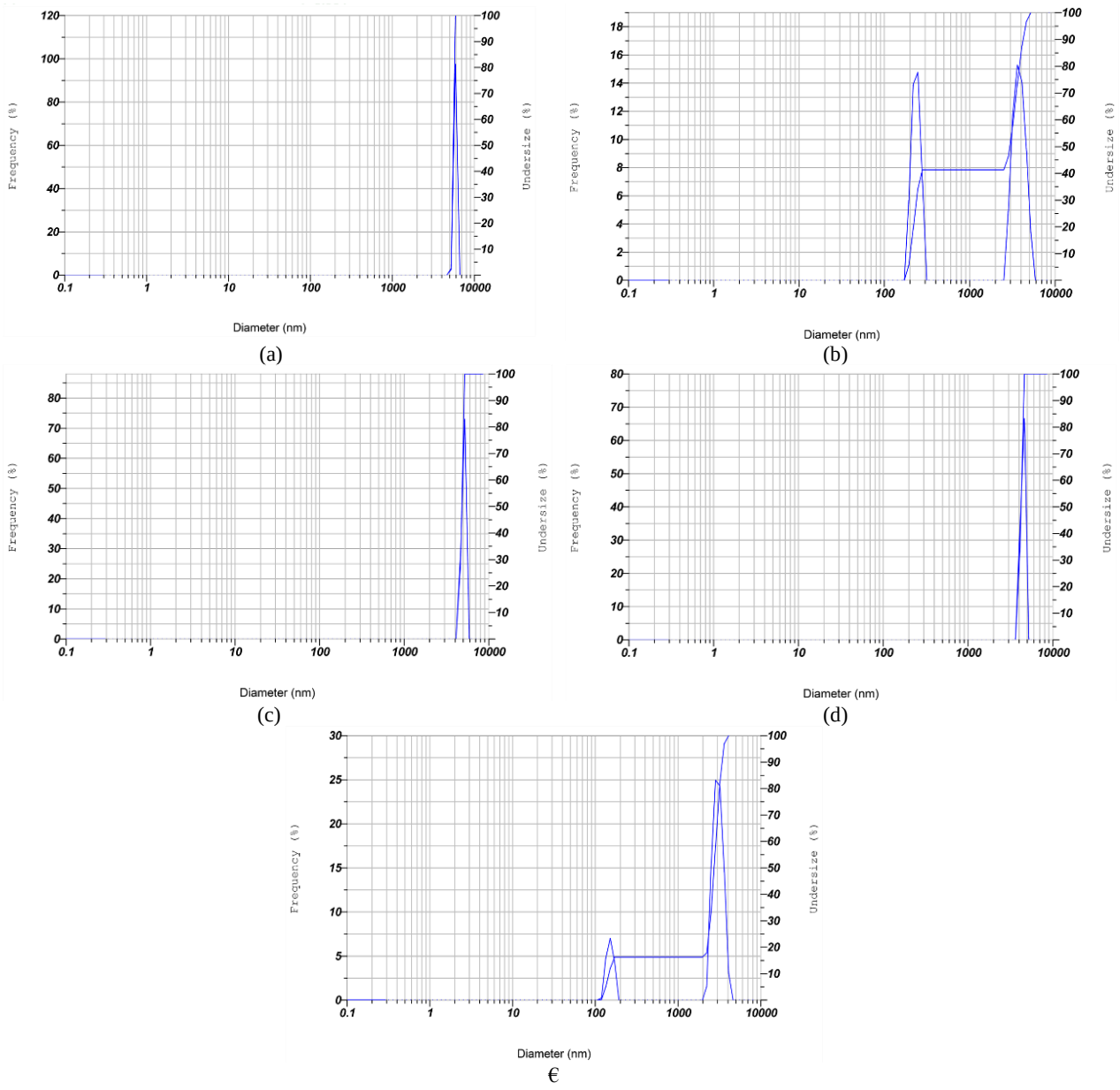

Figure 10. Size distribution of nano silica formed (a) without surfactant, with (b) ABS, (c) CTAB, (d) SDS, and (e) PVP

Based on particle size and degree of agglomeration, nano silica synthesized with PVP surfactant was the best product. However, based on the product composition, nano silica with PVP is the worst product due to salt impurities that cannot be removed entirely due to the presence of the template. It indicates that to get the best results, the template removal from the surfactant must be removed so that the product formed is not only small but also pure. This template can be removed using the calcination method [41].

To prove this point, this study tried to remove this PVP surfactant from the nano silica product through the calcination method. The calcination process was carried out at 400 °C for 3 hours. Then, the nano silica was characterized using the FTIR (fourier transform infrared spectroscopy) instrument to determine whether the surfactant functional groups were missing from the nano silica. The results of the characterization are presented in Fig. 12.

Figure 12 shows that the calcination process can reduce the PVP surfactant present in the nano silica product. It is indicated by a change in the functional groups of PVP surfactants such as CH_2 groups at 2,339.1 and 2,367.4 cm^{-1}; group C=N at 1,667.1 cm^{-1}; NH_2 group at 1,637.3 cm^{-1}; and the $N(CH_3)_2$ group at 517 and 805 cm^{-1}.

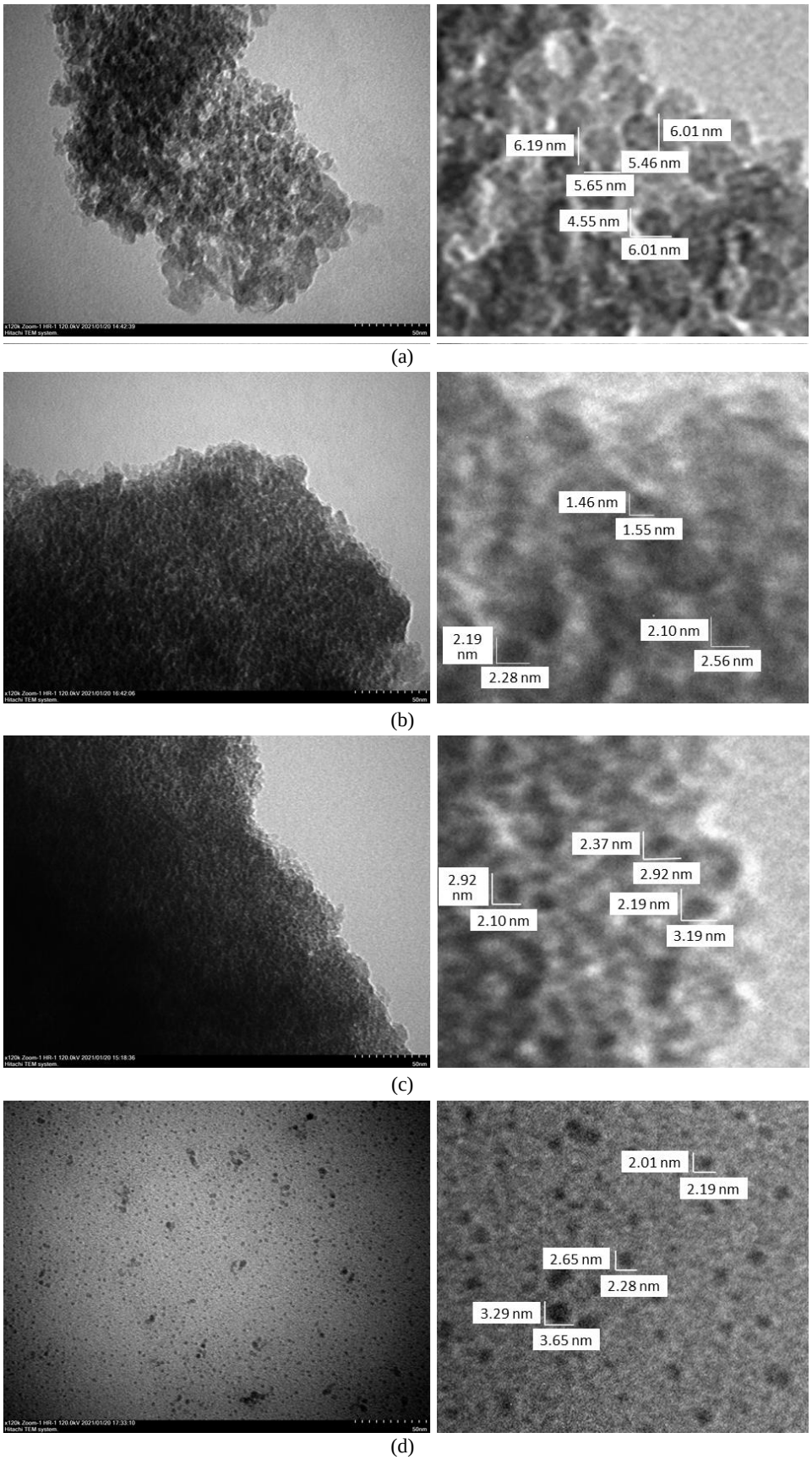

Figure 11. Morphology (left) and the size (right) of nano silica formed with (a) ABS, (b) CTAB, (c) SDS, and (d) PVP

Although in this study, the surfactant had not been completely removed, the results of the calcination process gave a positive pattern.

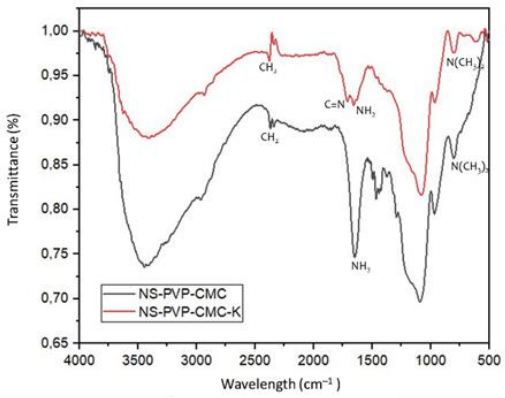

Figure 12. Results of FTIR characterization of PVP nano silica without calcination (black) and with calcination (red)

By changing the operating conditions of the calcination process, this PVP surfactant can be removed entirely.

4. CONCLUSION

This type of surfactant was studied in nano silica synthesis from geothermal sludge. Surfactants can prevent agglomeration between particles when it is used at the right surfactant concentration or usually called CMC (critical micelle concentration). This study showed that the CMC values of each surfactant studied were 0.15, 0.05, 0.50, and 1.00 wt% for ABS, CTAB, SDS, and PVP, respectively. Based on the characterization results of the nano silica composition, the product that gives the purest purity is nano silica without surfactant, where the purity of this product is 98.03%. Surfactants has been shown to reduce the possibility of agglomerated interparticle. A reduction in particle size prove it, and in this study, nano silica produced using PVP surfactant was able to reduce up to 66%. However, the product purity also decreased because the NaCl salt impurities were trapped in the surfactant template and made this salt challenging to remove. The results also showed that the type of surfactant that gave the best quality of nano silica products was PVP. The use of PVP resulted in the least agglomerated product, with particle sizes ranging from 2.01-3.65 nm.

ACKNOWLEDGMENT

The author acknowledges that this study was made possible with the assistance of the Institute for Research and Community Service, Parahyangan Catholic University (LPPM UNPAR), PLTP Dieng, and BRIN's Science Services for Research Laboratory.

REFERENCES

[1] T. Yokoyama, "Basic properties and measuring methods of nanoparticle: Size effect and properties of nanoparticles," in *Nanoparticle Technology Handbook*, 3rd edition, Ed., Elsevier, p.3, 2018. Doi: 10.1016/B978-0-444-64110-6. 00001-9.

[2] M. M. Modena, B. Rühle, T. P. Burg, and S. Wuttke, "Nanoparticle characterization: What to measure?," *Advanced Materials*, vol. 31, no. 32., pp. 1-26, 2019. Doi: 10.1002/adma.201901556.

[3] D. Talapin and E. Shevchenko, "Introduction: Nanoparticle chemistry," *Chemical Reviews*, vol. 116, no. 18. pp. 10343-10345, 2016. Doi: 10.1021/acs. chemrev.6b00566.

[4] G. Guisbiers, S. Mejía-Rosales, and F. L. Deepak, "Nanomaterial Properties: Size and shape dependencies," *Journal of Nanomaterials*, vol. 2012. no. 180976, pp. 1-2, 2012. Doi: 10.1155/2012/180976.

[5] S. Ganguly, K. Halder, N. A. Hoque, S. Das, and S. G. Dastidar, "A Comparative study between electrical properties of bulk and synthesized nano material of zinc sulphide," *American Journal of Research Communication*, vol. 3, no. 3, pp. 1-13, 2015.

[6] A. B. Asha and R. Narain, "Nanomaterials properties," in *Polymer Science and Nanotechnology: Fundamentals and Applications*, R. Narain, Ed., Elsevier, 2020, pp. 343-359. Doi: 10.1016/B978-0-12-816806-6.00015-7.

[7] S. N. A. Jenie, A. Ghaisani, Y. P. Ningrum, A. Kristiani, F. Aulia, and H. T. M. B. Petrus, "Preparation of silica nanoparticles from geothermal sludge via sol-gel method," in *AIP Conference Proceedings*, vol. 2026, no. 020008, pp. 1-5, 2018. Doi: 10.1063/1.5064968.

[8] A. Jyoti, R. K. Singh, N. Kumar, A. K. Aman, and M. Kar, "Synthesis and properties of amorphous nano silica from rice husk and its composites," *Materials Science and Engineering B*, vol. 263, pp. 1-7, 2021. Doi: 10.1016/j.mseb.2020. 114871.

[9] A. Maity and V. Polshettiwar, "Dendritic fibrous nano silica for catalysis, energy harvesting, carbon dioxide mitigation, drug delivery, and sensing," *ChemSusChem*, vol. 10, no. 20, pp. 3866-3913, 2017. Doi: 10.1002/cssc.201701076.

[10] M. Vallet-Regí, M. Colilla, I. Izquierdo-Barba, and M. Manzano, "Mesoporous

DOI : 10.14203/metalurgi.v37i2.637

Metalurgi is Sinta 2 Journal (https://sinta.ristekbrin.go.id/journals/detail?id=3708) accredited by Ministry of Research & Technology, Republic Indonesia

silica nanoparticles for drug delivery: Current insights," *Molecules*, vol. 23, no. 1, pp. 1-19, 2017. Doi: 10.3390/molecules 23010047.

[11] M. Manyangadze, N. M.H. Chikuruwo, T. B. Narsaiah, C. S. Chakra, G. Charis, G. Danha, and T. A. Mamvura, "Adsorption of lead ions from wastewater using nano silica spheres synthesized on calcium carbonate templates," *Heliyon*, vol. 6, no. 11, pp. 1-13, 2020. Doi: 10.1016/j.heliyon. 2020.e05309.

[12] S. D. Bukkitgar, N. P. Shetti, R. M. Kulkarni, and S. Churmure, "Nano-silica modified electrode as a sensor for the determination of mefenamic acid-A voltammetric sensor," in *Materials Today: Proceedings 5*, 2018. pp. 21466 - 21473. Doi: 10.1016/j.matpr.2018.06.556.

[13] A. N. Azzahra, E. S. Yusefin, G. Salima, M. M. W. M. Mudita, N. A. Febriani, and A. B. D. Nandiyanto, "Review: Synthesis of nano silica materials from various sources using various methods keywords," *Journal of Applied Science and Environmental Studies*, vol. 3, no. 4. pp. 254-278, 2020.

[14] P. Singh, S. Srivastava, and S. K. Singh, "Nano silica: Recent progress in synthesis, functionalization, biocompatibility, and biomedical applications," *ACS Biomaterials Science and Engineering*, vol. 5, no. 10, pp. 4882-4898, 2019. Doi: 10.1021/acsbiomaterials.9b00464.

[15] S. M. T. Al-Abboodi, E. J. A. Al-Shaibani, and E. A. Alrubai, "Preparation and characterization of nano silica prepared by different precipitation methods," in *IOP Conference Series: Materials Science and Engineering*, 2020, vol. 978, no. 1. Doi: 10.1088/1757-899X/978/1/012031.

[16] Sulardjaka, M. S. Rahman, and C. Wahyudianto, "Pengaruh waktu dan temperatur sinter terhadap densitas dan porositas komposit aluminium yang diperkuat limbah geothermal." *Rotasi*, vol. 15, no. 4, pp. 28-32, 2013. doi: 10.14710/rotasi.15.4.28-32.

[17] S. Muljani, B. Wahyudi, and K. Sumada, "Potassium silicate foliar fertilizer grade from geothermal sludge and pyrophyllite," in *MATEC Web of Conferences*, 2016, vol. 58, no. 01021. Doi: 10.1051/conf/2016.

[18] H. T. B. M. Petrus, M. Olvianas, M. F. Shafiyurrahman, I G. A. A. N. Pratama, S. N. A. Jenie, W. Astuti, M. I. Nurpratama, J. J. Ekaputri, and F. Anggara, "Circular economy of coal fly ash and silica geothermal for green geopolymer: characteristic and kinetic study," *Gels*, vol. 8, no. 4, pp. 1-14, 2022. Doi: 10.3390/gels8040233.

[19] S. N. A. Jenie, F. S. H. Krismastuti, Y. P. Ningrum, A. Kristiani, M. D. Yuniati, W. Astuti, and H. T. B. M. Petrus, "Geothermal silica-based fluorescent nanoparticles for the visualization of latent fingerprints," *Materials Express*, vol. 10, no. 2, pp. 258-266, 2020. Doi: 10.1166/mex.2020.1551.

[20] G. J. Owens, R. K. Singh, F. Foroutan, M. Alqaysi, C.-M, Han, C., Mahapatra, H.-W. Kim, and J. C. Knowles, "Sol-gel based materials for biomedical applications," *Progress in Materials Science*, vol. 77, pp. 1-79, 2016. Doi: 10.1016/j.pmatsci.2015. 12.001.

[21] A. Feinle, M. S. Elsaesser, and N. Hüsing, "Sol-gel synthesis of monolithic materials with hierarchical porosity," *Chemical Society Reviews*, vol. 45, no. 12. pp. 3377-3399, 2016. Doi: 10.1039/c5cs00710k.

[22] D. Bokov, A. T. Jalil, S. Chupradit, W. Suksatan, M. J. Ansari, I. H. Shewael, G. H. Valiev, and E. Kianfar, "Nanomaterial by sol-gel method: Synthesis and application," *Advances in Materials Science and Engineering*, vol. 2021, pp. 1–21. 2021. Doi: 10.1155/2021/5102014.

[23] A. V. Rane, K. Kanny, V. K. Abitha, and S. Thomas, "Methods for synthesis of nanoparticles and fabrication of nanocomposites," in *Synthesis of Inorganic Nanomaterials*, 1st edition, Ed., Elsevier, pp. 121-139, 2018. Doi: 10.1016/b978-0-08-101975-7.00005-1.

[24] A. Lewis, "Precipitation of heavy metals," in *Sustainable Heavy Metal Remediation, Volume 2: Case Studies*, Ed., Springer International Publishing AG., pp. 101-120, 2017. Doi: 10.1007/978-3-319-58622-9_4.

[25] K. C. Wanta, S. Lim, R. F. Susanti, G. P. Gemilar, W. Astuti, and H. T. B. M. Petrus, "Effect of surfactant type on synthesis and characteristics of nanonickel hydroxide," *Jurnal Rekayasa Proses*, vol. 15, no. 2, p. 217, 2021. Doi: 10.22146/jrekpros.69723.

[26] R. Stanley and A. S. Nesaraj, "Effect of surfactants on the wet chemical synthesis of silica nanoparticles," *International Journal of Applied Science and Engineering*, vol. 12, no. 1, pp. 9-21, 2014.

Doi: 10.6703/IJASE.2014.12(1).9.
[27] R. Songolzadeh and J. Moghadasi, "Stabilizing silica nanoparticles in high saline water by using ionic surfactants for wettability alteration application," *Colloid and Polymer Science*, vol. 295, no. 1, pp. 145-155, 2017. Doi: 10.1007/s00396-016-3987-3.
[28] P. Ding and A. W. Pacek, "De-agglomeration of silica nanoparticles in the presence of surfactants," *Journal of Dispersion Science and Technology*, vol. 29, no. 4, pp. 593-599, 2008. Doi: 10.1080/01932690701729302.
[29] L. P. Singh, S. K. Bhattacharyya, G. Mishra, and S. Ahalawat, "Functional role of cationic surfactant to control the nano size of silica powder," *Applied Nanoscience*, vol. 1, no. 3, pp. 117-122, 2011. Doi: 10.1007/s13204-011-0016-1.
[30] K. D. Rakhmasari, I. Perdana, A. Prasetya, and D. B. Pidhatika, "Nanosilika dari prekursor silika geotermal: Pengaruh konsentrasi surfaktan dan dekomposisi trmal pasca sintesis," in *Prosiding Seminar Nasional Teknik Kimia 'Kejuangan'*, 2019.
[31] T. Song, F. Gao, S. Guo, Y. Zhang, S. Li, H. You, and Y. Du, "A review of the role and mechanism of surfactants in the morphology control of metal nanoparticles," *Nanoscale*, vol. 13, no. 7, pp. 3895-3910, 2021. Doi: 10.1039/ d0nr07339c.
[32] D. Myers, "Surfactant Science and Technology,", 3rd edition, New Jersey, USA: John Wiley & Sons, p. 118, 2006.
[33] S.-J. Kim, S.-G. Seo, and S.-C. Jung, "Preparation of high purity nano silica particles from blast-furnace slag," *Korean Journal of Chemical Engineering*, vol. 27, no. 6, pp. 1901-1905, 2010. Doi: 10.1007/s11814-010-0289-1.
[34] H. El-Didamony, E. El-Fadaly, A.A. Amer, and I. H. Abazeed, "Synthesis and characterization of low cost nano silica from sodium silicate solution and their applications in ceramic engobes," *Boletin de la Sociedad Espanola de Ceramica y Vidrio*, vol. 59, no. 1, pp. 31-43, 2020. Doi: 10.1016/j.bsecv.2019.06.004.
[35] Y. Liu, M. Tourbin, S. Lachaize, and P. Guiraud, "Silica nanoparticles separation from water: Aggregation by cetyltrimethylammonium bromide (CTAB)," *Chemosphere*, vol. 92, no. 6, pp. 681-687, 2013. Doi: 10.1016/j.chemo sphere.2013.03.048.
[36] H. R. Ong, W. M. E. Iskandar, and M. M. R. Khan, "Rice husk nano silica preparation and its potential application as nanofluids," in *Engineered Nanomaterials - Health and Safety*, S. M. Avramescu, Ed., IntechOpen, pp.1-25, 2020. Doi: 10.5772/intechopen.89904.
[37] J. Chruściel and L. Ślusarski, "Synthesis of nano silica by the sol-gel method and its activity toward polymers," *Materials Science*, vol. 21, no. 4, pp. 461-469, 2003.
[38] E. Katoueizadeh, M. Rasouli, and S. M. Zebarjad, "A comprehensive study on the gelation process of silica gels from sodium silicate," *Journal of Materials Research and Technology*, vol. 9, no. 5, pp. 10157-10165, 2020. Doi: 10.1016/j.jmrt. 2020.07.020.
[39] S. C. Ayirala and D. N. Rao, "Multiphase flow and wettability effects of surfactants in porous media," in *Colloids and Surfaces A: Physicochemical and Engineering Aspects*, vol. 241, pp. 313-322, 2004. Doi: 10.1016/j.colsurfa.2004.04.047.
[40] J. Xian, Q. Hua, Z. Jiang, Y. Ma, and W. Huang, "Size-dependent interaction of the poly(N-vinyl-2-pyrrolidone) capping ligand with Pd nanocrystals," *Langmuir*, vol. 28, no. 17, pp. 6736-6741, 2012. Doi: 10.1021/la300786w.
[41] Q. Liang, X. Liu, G. Zeng, Z. Liu, L. Tang, B. Shao, Z. Seng, W. Zhang, Y. Liu, M. Cheng, W. Tang, and S. Gong, "Surfactant-assisted synthesis of photocatalysts: Mechanism, synthesis, recent advances and environmental application," *Chemical Engineering Journal*, vol. 372. pp. 429-451, 2019. Doi: 10.1016/j.cej.2019.04.168.

AUTHOR INDEX

SUBJECT INDEX